RICE UNIVERSITY

Functionalization of Carbon Materials with Metals

by

KOURTNEY DAWN WRIGHT

A THESIS SUBMITTED
IN PARTIAL FULFILLMENT OF THE
REQUIREMENTS FOR THE DEGREE OF
Doctor of Philosophy

APPROVED, THESIS COMMITTEE

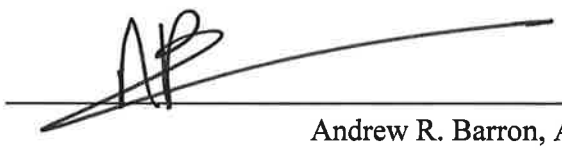

Andrew R. Barron, Advisor
Charles W. Duncan, Jr. – Welch Chair of Chemistry
Professor of Chemistry and Materials Science

Kenton H. Whitmire
Associate Dean for Academic Affairs, Weiss School of Natural Sciences
Professor of Chemistry

Matteo Pasquali
Department Chair of Chemistry
A. J. Hartsook Professor of Chemical and Biomolecular Engineering and Chemistry

Houston, TX

May, 2017

Abstract

Functionalization of Carbon Materials with Metals

by

Kourtney Dawn Wright

The functionalization of carbon nanotubes (CNTs) with metals has been shown to produce materials with interesting and useful properties which are different from the isolated constituents. Although metal atoms and particles have been attached to CNTs in a variety of different ways, there is a need for the development of novel approaches in many cases. In this work, SWNTs and other conjugated carbon materials were deposited with copper and Group 6 metals.

In attempting to functionalize SWNTs with Group 6 metal atoms for electronics applications, we found that the formation of such species is very sensitive to oxidation by adsorbed/bound oxygen and by oxidized residual catalyst material. Annealing and acid treating the SWNTs allowed for the addition of some zero valent metals, while the use of very high purity SWNTs and graphene allowed for the deposition of primarily zero valent Group 6 metals.

As a result of these oxidation issues with SWNTs and because of the limited characterization methods available for SWNTs, we used C_{60} fullerene to study complexes of conjugated carbon systems with copper(I) and chromium(0). Although the synthesis of an η^6-C_{60}-Cr(0) complex was unsuccessful, ^{1}H NMR experiments did suggest the formation of an η^2-C_{60}-Cu(I) complex. These results suggest that similar complexes with SWNTs would also be stable.

This work also describes the uniform deposition of copper(0) seed particles with a narrow size distribution on pyridine functionalized SWNTs, which may be used as precursor for the development of more consistent Cu-CNT composites. The use of pyridine functional groups was found to be crucial in the formation of the desired copper seeds, and bonding between the seeds and the pyridine groups was verified using ^{1}H NMR and UV-visible spectroscopic experiments.

“I am a great believer in luck. The harder I work, the more of it I seem to have.”

– *Coleman Cox*

Acknowledgements

At the beginning of my graduate career, I knew that getting a PhD would be a challenge. But, no one can really prepare you for the pressure and frustration that all graduate students experience. Most of the time, experiments do not work, and it is easy to begin questioning your abilities as a chemist. Of course, not all of the time I spent in graduate school was like this; when experiments were working, I was on top of the world! I was also fortunate enough to visit collaborators at Swansea University in Wales and do two internships at Lockheed Martin during my graduate career, which landed me a job with them. I have also made some of the best friends I've ever had while I was in graduate school. Although I always enjoyed celebrating the good times with friends and family, it was during the tough times that I really appreciated being surrounded by people willing to help. I would like to acknowledge and sincerely thank all of the people who have been so supportive and helpful throughout my graduate career.

First and foremost, I would like to thank my family. Ma and Herm, you are the best parents a girl could ask for. You always said I could be whatever I wanted to be, and, because you meant it, I believed it. You also taught me that success only comes through hard work. Without that, I never would have made it to where I am today. Kels, thank you for being my best friend as well as my sister and for using up all of your vacation days to visit me. Tyler, thanks for being the brother I never had. Patty, thank you for your incredible patience and kindness, for your White Russians, and for your delicious enchiladas. Thank you all for your love and support on this crazy journey.

I also have to thank my friends Britt, Neil, Nadia, Neal, Courtney, J.T., Lauren, Aileen, Richard, John and Amy. I don't know how many times one of you has had to talk

me down from some crisis state! I can say with certainty that I wouldn't have lasted very long without you. Thank you for always being so willing to help me with anything and everything and for being my family away from home. Britt and Nadia, I surely would not have survived my qualifying exam if you two hadn't been there to edit my paper, listen to my talk multiple times and give me plenty of emotional support. Thank you for being amazing friends.

And, of course, there are many people at Rice that I need to recognize. Bo Chen, Emilie Ringe, Wen Guo, Larry Alemany and Sadegh Yazdi taught me nearly everything that I know about the instruments that were crucial to the results that made up this thesis. Thank you for always being willing to take time out of your busy day to help me better understand my data and teach me new things. I also need to thank Jane McNeel, who helped the Barron lab with so much, but was also always available to chat or, sometimes, lend a shoulder to cry on. We miss you, Jane! To my lab mates; Enrico, Yen-Tien, Saunab, Gibran, Britt, Lauren, Pavan and Cathy; thank you for listening to hours of practice talks and for offering your help when I needed it.

I would also like to offer a big thank you to my committee members, Matteo Pasquali and Kenton Whitmire. Not only have they taken time out of their busy schedules to read my thesis and attend my defense, but they have also helped me throughout my graduate career. Dr. Whitmire, thank you for letting me use your IR and for allowing me to barge into your office with random questions. Dr. Pasquali, thank you for all of the things that you do behind the scenes for the Chemistry Department and the graduate students in particular.

Lastly, I need to sincerely thank my advisor, Dr. Barron. I appreciate that you always made time to help me sort through difficult data and discover new ways of approaching problems, despite your incredibly busy schedule. Thank you for teaching me that just because a result isn't the one that I wanted or expected, it is still a result that tells a story nonetheless. I am also forever grateful that you were willing to let me leave for over six months to do two internships with Lockheed Martin. I'm not sure this benefited you much, but it was incredibly useful for me both in terms of my future career and in bettering myself as a scientist. Thank you for everything that you've done for me over the past four years.

Table of Contents

List of Figures

Introduction

Chapter 1

List of Tables

Chapter 1

Chapter 3

Chapter 4

Abbreviations

A	ampere, absorbance
a	lattice parameter
Å	angstrom
ALD	atomic layer deposition
a.u.	arbitrary units
ATR	attenuated total reflectance
b	path length
˚C	degrees Celsius
c	concentration
c	speed of light
cm	centimeter
CNL	Carbon Nanotube Laboratory
^{13}C NMR	carbon nuclear magnetic resonance
CNT	carbon nanotube
c/s	counts per second
CVD	chemical vapor deposition
d	plane spacing
DCC	1,3-dicyclohexylcarbodiimide
˚	degree
DI	deionized
DMAP	4-(dimethylamino)pyridine
DMF	dimethylformamide

dpa	dipyridylamine
DSC	differential scanning calorimetry
e	elementary charge of an electron
ε	extinction coefficient
EDTA	ethylenediamenetetraacetic acid
EDX	energy dispersive X-ray spectroscopy
eV	electron volts
FCC	face-centered cubic
FTIR	Fourier transform infrared spectroscopy
FWHM	full width half maximum
g	gram
GPa	gigapascal
GW	gigawatt
graph	graphene
h	hour
h	Planck's constant, Miller index of the x direction
HPLC	high performance liquid chromatography
^{1}H NMR	proton nuclear magnetic resonance
HiPco	high pressure carbon monoxide
HRM	hot rolling mill
IR	infrared
K	kelvin
k	Miller index of the y direction

kcal	kilocalories
kΩ	kiloohm
kV	kilovolts
L	camera length
l	Miller index of the z direction
M	molar (mol/L)
m	meter
m_0	mass of the electron at rest
mes-dpa	mesitylene-2,2’-dipyridylamine
μm	micrometer
mg	milligram
MHz	megahertz
min	minute
mL	milliliter
mmol	millimole
mol	mole
MPa	megapascal
MW	megawatt, microwave
mSWNT	metallic single wall carbon nanotube
MWNT	multi wall carbon nanotube
NaDDBS	sodium dodecylbenzenesulfonate
η^1	monohapto
η^2	dihapto

η^3	trihapto
η^5	pentahapto
η^6	hexahapto
N/A	not applicable
nm	nanometer
NMR	nuclear magnetic resonance
NP	nanoparticle
ppb	parts per billion
ppm	parts per million
%	percent
% v/v	volume percent
% w/w	weight percent
π	pi
PTFE	polytetrafluoroethylene
PVDF	polyvinylidene fluoride
py-SWNT	pyridine-functionalized ultra-short single wall carbon nanotube
py-US-SWNT	pyridine-functionalized ultra-short single wall carbon nanotube
r	radius
rpm	rotations per minute
S	siemens
s	second
SAED	selected area electron diffraction
sccm	standard cubic centimeter per minute

SEM	scanning electron microscopy
sSWNT	semiconducting single wall carbon nanotube
σ	sigma
SWNT	single-wall carbon nanotube
TEM	transmission electron microscopy
TGA	thermogravimetric analysis
THF	tetrahydrofuran
TPa	terapascal
U	accelerating voltage
UCC	ultraconductive copper
US-SWNT	ultra-short single wall carbon nanotube
UV-Vis	ultraviolet-visible
V	volt
W	watt
λ	wavelength
XPS	X-ray photoelectron spectroscopy
XRD	X-ray diffraction

Introduction

Since their discovery in 1991,[1] single-walled carbon nanotubes (SWNTs) have become a popular research topic as a result of their unique properties. Conceptually, SWNTs can be thought of as ribbons of graphene which are rolled into cylinders and then capped with a segment of a fullerene.[2] Depending on how the graphene segment is folded, three different chiralities of SWNTs exist: armchair, zigzag and chiral.[2] SWNTs with armchair chirality are metallic, whereas SWNTs with chiral or zigzag chiralities may be semiconducting or metallic depending on their diameter.[2] Metallic SWNTs (mSWNTs) have been shown to have a resistivity of 4 kΩ/μm and a mean-free path of 1.6 μm.[3] Semiconducting SWNTs (sSWNTs) have a resistivity of 20 kΩ/μm and a mean-free path length of 300 nm.[4] At lengths shorter than the mean-free path, SWNTs are ballistic conductors.[5] Thus, electrons do not lose momentum as they travel through the SWNT, and the contacts are the only source of resistance in the system.[5] According to theory, ballistic conductivity may be possible at 10 μm or more if the SWNTs are of very high quality with few defects.[5] In comparison, the mean-free path of copper, one of the most prevalent conductors used today, is a short 40 nm.[5] Additionally, carbon nanotubes (CNTs, implying an unknown mixture of SWNTs and multi walled carbon nanotubes, MWNTs) have very high current carrying capability with a theoretical limit of 10^9 A/cm^2.[6] This is much higher than Cu, which has an ampacity of 10^6 A/cm^2.[6] SWNTs also have remarkable mechanical properties with theoretical and experimental Young's moduli of 1.5 TPa[7] and 1.002 TPa,[8] respectively, and an experimental tensile strength of 30 GPa.[8] For comparison, steel has a Young's modulus of 200 GPa[9] and a tensile strength 0.8 GPa.[10] Further, SWNTs show thermal conductivities as high as 6,600 W/(m K),[11]

whereas diamond, previously the best thermal conductor known, shows 2,200 W/(m K).[12] These and other useful properties are the reason SWNTs have been studied for a number of applications ranging from field effect transistors[13] to tissue engineering.[14]

Perhaps the largest area of SWNT research is dedicated to SWNT functionalization, with the majority of these reports being focused on adding organic functional groups.[15] On the other hand, there are relatively few reports on the functionalization of SWNTs with metals. Although organic functionalization has been very useful for dispersing SWNTs in different mediums[16–18] and for SWNT purification,[18,19] functionalization of SWNTs (as well as MWNTs) with metals has shown promise towards many interesting applications including catalysis, energy storage, sensing and others.[15] Here, we review some of the methods that have been used to functionalize CNTs with metals. These have been organized according to the flow chart shown in Figure 0.1.

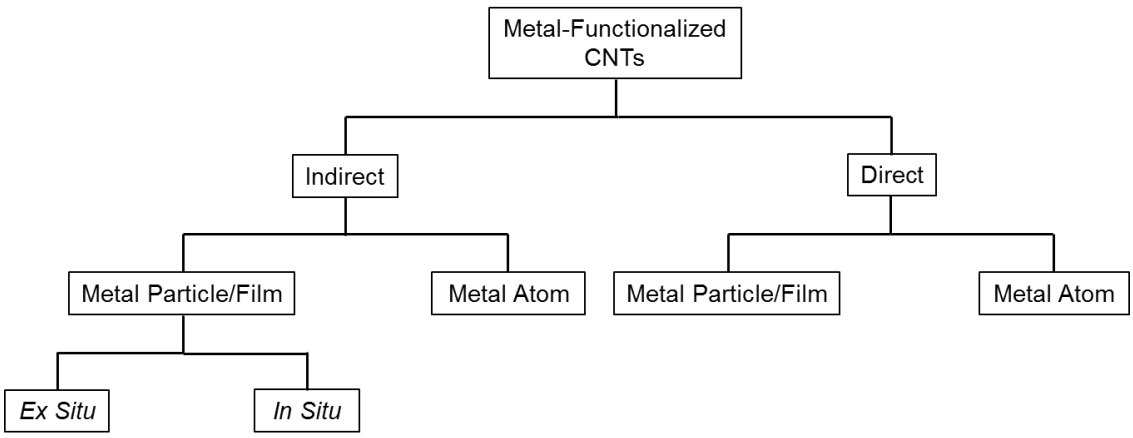

Figure 0.1. Discussion of metal functionalized CNTs is organized according to this chart.

Indirect metal particle and film functionalized CNTs. Of the methods that have been reported for functionalizing CNTs with metals, some of the most common methods involve attaching *ex situ*-synthesized metal particles to CNTs by way of an organic functional group. The main advantage of synthesizing particles before incorporating them onto CNTs is the improved control over the size and shape of the particles than would be had if they were synthesized directly on CNTs.[15] Typically, CNTs are treated with an oxidizing acid, such as nitric or sulfuric acid, to add carboxylic acid, ketone and alcohol groups to the SWNT ends and sidewalls.[20–22] These CNTs can then be used as is or can be functionalized further with other groups to accommodate metal binding. Multiple groups have reported the attachment of pre-synthesized metal oxide nanoparticles such as TiO_2,[23] MnO_2[24] and MgO[25] directly to acid-treated CNTs using solution-based methods. In the case of TiO_2, this method produced well dispersed particles,[23] which have been shown to interact strongly with the CNTs as a result of esterification between carboxylic acids on the CNTs and alcohols on the metal oxide particles.[26] Although the authors of the MnO_2[24,27] and MgO[25] papers did not comment on the adhesion of their particles, it is likely that other metal oxides form ester linkages to CNTs as well.

For binding unoxidized and oxidized metal particles, others have used the CNT carboxylic acid groups as a basis for the synthesis of thiols, phosphonic acids and other functional groups. For instance, Banerjee used ethylenediamine to functionalize acid-treated CNTs with amine groups, which were then reacted with acid terminated, mercaptobenzoic acid-capped CdSe quantum dots.[16] Azamian reacted acid-treated CNTs with 2-aminoethanethiol to produce thiol-terminated CNTs, which have a very strong

interaction with gold nanoparticles.[28] Sainsbury used 2-aminoethylphosporic acid to add phosphoric acid-terminated groups to the CNTs, allowing them to bind to TiO_2 particles.[29] Acid-treated CNTs have also been functionalized with charged polymers, thereby forming a charged coating which is dense and well dispersed on the tube's surface. These functionalized CNTs support a layer of charged metal particles interacting through strong ionic bonds. An example of this method can be found in a report by Jiang in which acid-treated CNTs were functionalized with poly(diallyldimethylammonium) chloride, PDDA.[30] The positively charged tubes were then decorated with negatively charged gold nanoparticles.[30]

For applications that would suffer from incomplete conjugation of the CNTs, other methods that do not modify the structure of the tubes have been developed. The first of these methods involves wrapping pristine CNTs with charged surfactants, which then form ionic bonds with charged metal nanoparticles. For example, Hrapovic dispersed pristine CNTs in Nafion, a negatively charged perfluorosulfonated polymer, which then allowed for the attachment of platinum nanoparticles.[31] Another method of this type utilizes π-π interactions between the CNTs and an aromatic linker to functionalize the tubes with metal particles. For instance, CNTs have been coated with carboxylic acid-modified pyrene molecules, which then serve as an anchor (through the carboxylic acid group) for oleic acid-capped Co, Co/Pt and iron oxide nanoparticles (Figure 0.2).[32] This method generated stable solutions of metal-functionalized CNTs in toluene and chloroform for 3 weeks.[32] This acts as testament to the stability of these modified CNTs, since neither the CNTs alone nor the pyrene-modified CNTs were soluble.[32] A similar method used triphenylphosphine to link Pt particles to CNTs.[33]

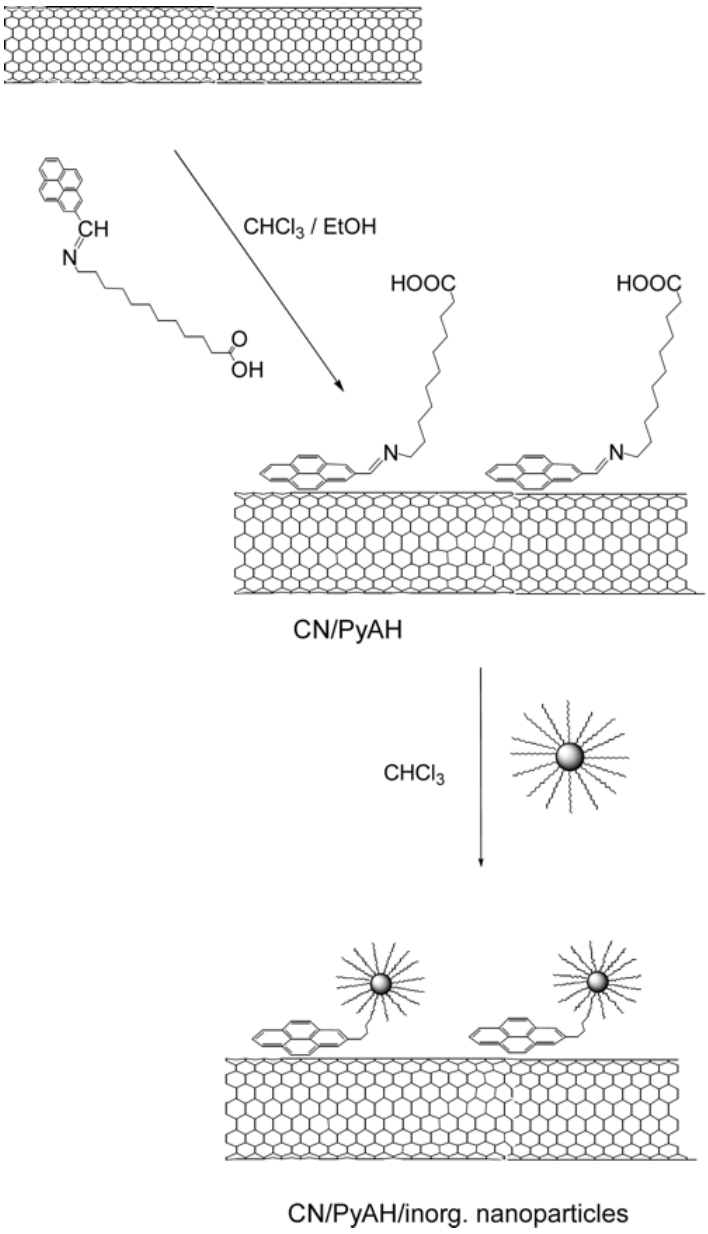

Figure 0.2. The functionalization of CNTs with oleic acid-capped nanoparticles through carboxylic acid-modified pyrene molecules. Reprinted with permission from V. Georgakilas, V. Tzitzios, D. Gournis and D. Petridis, *Chem. Mater.*, 2005, **17**, 1613–1617. Copyright 2005 American Chemical Society.

Although the *ex situ* synthesis of metal nanoparticles allows for better control of particle sizes and shapes, it also limits the type of composites that can be made. For

instance, obtaining a complete, uniform film of metal on the CNT surface using an ex situ method is impossible. Thus, for some applications, it is necessary to attach the metal using *in situ* synthesis methods. Although synthesizing metals particles directly on CNTs does not allow as much control over particle morphology, it does allow for the formation of more diverse metal structures using a broader range of methods. For instance, all of the methods discussed up to this point have been solution-based methods. Such methods are useful for adding particles to all of the reactive CNT surfaces, but, in most cases, they are not ideal for adding particles to aligned CNT films. In these circumstances, gas phase deposition is optimal, since it does not disturb the position of the CNTs. Further, these methods allow for the controlled addition of metal layers to obtain the desired thickness.[15] This is especially true for atomic layer deposition (ALD), which, as the name suggests, allows for the addition of individual atomic layers.[15] Although very slow, this method works well for the addition of uniform and pinhole-free films.[15] As an example, acid-treated CNTs were subjected to $TiCl_4$ gas to form a monolayer of $–OTiCl_3$ groups.[34] These were then hydrolyzed to generate $–OTi(OH)_3$ groups.[34] This process was repeated until an 8-10 nm layer of titanium hydroxide was formed.[34] These were then heated to 700 ˚C to generate a uniform TiO_2 layer on the CNTs.[34] Another common gas deposition method is chemical vapor deposition (CVD), which is commonly used in the semiconductor industry because of its scalability and the high purity of resulting films or particles.[15] These films/particles are easily produced by introducing a reactive metallic gas into the CVD chamber and then decomposing or reacting the gas on the sample surface to produce a solid.[15] For instance, a uniform distribution of 3-15 nm SnO_2 particles have been deposited by decomposing SnH_4 at 550 ˚C on acid-treated CNTs.[35]

The authors found that the size of the nanoparticles could be increased by increasing the deposition time (Figure 0.3) or precursor flow rate (Figure 0.4).[35]

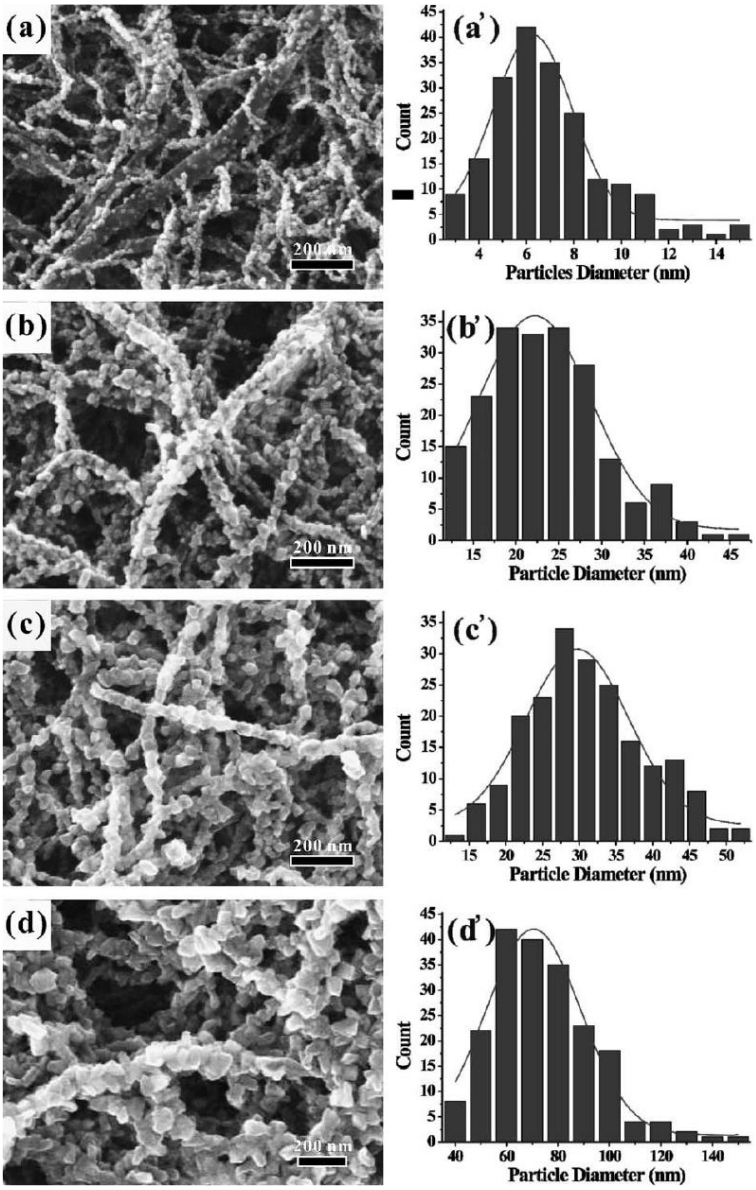

Figure 0.3. SEM images and cooresponding histograms of particle size distrubutions of SnO_2 particles deposited on acid-treated CNTs by CVD after (a, a') 0.5 min, (b, b') 1 min, (c, c') 2 min and (d, d') 3 min of deposition time. Reprinted with permission from Q. Kuang, S.-F. Li, Z.-X. Xie, S.-C. Lin, X.-H. Zhang, S.-Y. Xie, R.-B. Huang and L.-S. Zheng, *Carbon*, 2006, **44**, 1166–1172.

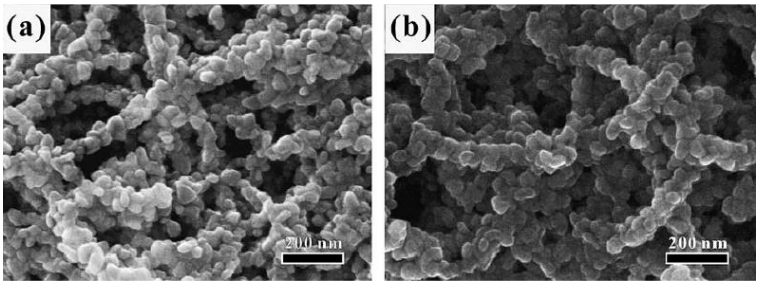

Figure 0.4. SEM of acid-treated CNTs coated with SnO_2 particles by CVD after 0.5 min of deposition time with (a) 20 sccm and (b) 30 sccm SnH_4/N_2 flow rates. Reprinted with permission from Q. Kuang, S.-F. Li, Z.-X. Xie, S.-C. Lin, X.-H. Zhang, S.-Y. Xie, R.-B. Huang and L.-S. Zheng, *Carbon*, 2006, **44**, 1166–1172.

For applications where the orientation of the CNTs does not matter, solution-based methods may be used to deposit metal particles on the tubes. One of the most commonly used solution-based methods is electroplating, which involves the deposition of metals on the CNT surface using an applied voltage.[15] This method is advantageous, because the number of particles and particle sizes can be tuned by adjusting the applied potential, deposition time and the metal salt concentration.[36,37] For example, this method has been used to deposit Pt from a K_2PtCl_4 solution onto CNTs which underwent electrochemical activation in Na_2SO_4 to add oxygen functional groups to the tubes defect sites and ends.[38] The authors report that the resulting Pt particles preferentially grow on carboxylic acid functional groups to form strong composites which survive sonication.[38] A similar method was used to deposit Pt/Ru particles from a H_2PtCl_6 and $RuCl_3$ solution.[39] However, as a result of decreasing current through the length of a CNT film, the density of metal nanoparticles formed on the tubes tends to decrease moving away from the contact, see Figure 0.5.[37] Thus, electroplating is not ideal for generating uniform densities of particles across large films of overlapping CNTs.

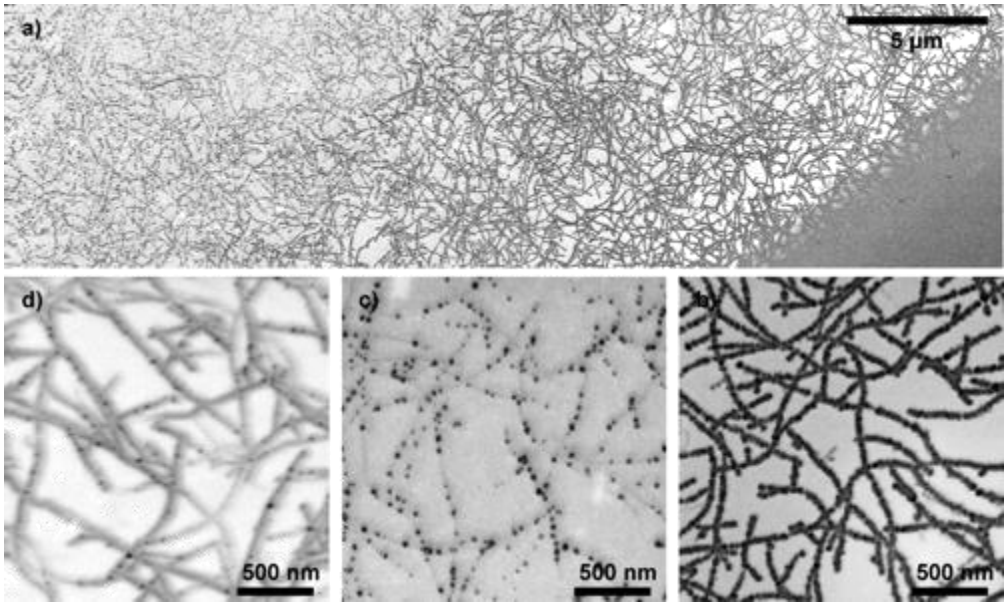

Figure 0.5. SEM images of a CNT film that was functionalized with Pt particles using electrodeposition at a potential of -0.4 V for 30 s, showing a deacrease in particle density as the distance from the electrode increases (a). Particles are densly packed (b), become differentiable (c) and eventually become very disperse (c) moving away from the electrode. Reprinted with permission from T. M. Day, P. R. Unwin, N. R. Wilson and J. V. Macpherson, *J. Am. Chem. Soc.*, 2005, **127**, 10639–10647. Copywrite 2005 American Chemical Society.

A solution-based method that is similar to electroplating uses chemical reduction rather than an applied voltage to deposit metals on CNTs. An advantage to using chemical reduction over electroplating is the elimination of the particle density gradient seen in Figure 0.5. Thus, particles deposited by chemical reduction tend to be more evenly dispersed on the CNTs. However, this method does not work well for pre-aligned CNT films because the deposition solution must be stirred in order to maintain a homogenous solution. This process has been used to deposit gold nanoparticles on thiol-functionalized CNTs by reducing $HAuCl_4$ with citric acid.[40] The gold particles were well

dispersed on the CNTs and had an average size of 1.7 nm with a narrow size distribution.[40] A similar experiment conducted with pristine CNTs resulted in the formation of few gold particles on the tubes with sizes between 10 and 100 nm.[40] Thus, the thiol functional groups act as seed locations for particle growth and adhesion. Copper nanoparticles have also been deposited on acid-treated CNTs from $CuSO_4 \cdot 5H_2O$ using formaldehyde as the reducing agent in basic solution.[41] The authors also reported that deposition on pristine CNTs resulted in growth of few particles with large sizes,[41] confirming the importance of functional groups for particle size and distribution control. Further, particle size and distribution could be controlled by changing the concentration of the reducing agent or copper precursor.[41] However, if the reaction proceeded too fast (by using high concentrations), large particles formed sporadically on the tubes.[41] Another group reported the formation of CNT/CdS core-shell nanowires by reducing sulfur with KBH_4 and reacting the resulting S^{2-} with Cd^{2+} in the presence of oxidized CNTs.[42] This method has also been used to indirectly functionalize CNTs with metal particles using non-covalent methods. Li accomplished this by functionalizing CNTs with 1-aminopyrene through π-π interactions, which then acted as a seeding location for the formation of Pt and CdS particles by chemical reduction.[43] Similar methods were used by Wu to deposit Cu particles on CNTs functionalized with polyethylenimine or poly(sodium 4-styrenesulfonate).[44]

Still, another common method for functionalizing CNTs is by the sol-gel process, which is commonly used to form ceramics and glasses.[15,45] In this process, a colloidal suspension of solid particles in a liquid, called a sol, undergoes condensation or hydrolysis to form polymeric units, which further react to generate a continuous solid

network surrounded by a liquid phase that together make up the gel.[45] The gel is then dried under various conditions to make the desired porous or dense ceramic.[45] For example, Eder used the sol-gel method to coat CNTs with TiO_2.[46] Specifically, pristine CNTs were dispersed in solution with benzyl alcohol, which acted as a surfactant.[46] Then, tetrabutyl-orthotitanate (TBOT) was added dropwise to the solution and hydrolyzed to form a TiO_2 layer indirectly attached to the CNTs via the benzyl alcohol surfactant.[46] After drying at 80 ˚C, the CNTs were completely coated with a smooth TiO_2 layer with few particles (Figure 0.6b).[46] However, quickly drying the composites in this way resulted in stress cracking of the coating (Figure 0.6c).[46] On the contrary, slowly drying the composites in air prevented cracking, but also resulted in the formation of a thicker TiO_2 coating (Figure 0.6e).[46] When this method was attempted without the surfactant, the resulting TiO_2 layer was not uniform and formed aggregated particles (Figure 0.6a).[46] This illustrates the importance of the surfactant-sol interaction in making uniform layers on the CNTs. However, the downside to using sol-gel methods is their inability to generate crystalline materials.[15,46] This is evident by the electron diffraction pattern shown in Figure 0.6d, which only shows a pattern for the CNTs.[46] Further, it has been shown that this method works best *in-situ*; when the sol was synthesized prior to addition of the CNTs in the previously mentioned example, the nanotubes were inefficiently covered with TiO_2 (Figure 0.6f).[46] The sol-gel process has also been used to add metal particles (RuO_2, for example)[47] to oxidized SWNTs. However, due to the uncertainty of location and degree of oxygen functionality on acid-treated CNTs, it has been reported that use of these in the sol-gel process sometimes result in non-uniform coatings.[15]

Indirect metal atom functionalized CNTs. Although there are fewer examples of indirect complexation of metal atoms to CNTs compared to metal particles, the complexes that have been formed are generally more novel. For example, Banerjee has functionalized oxidized CNTs with Vaska's compound (*trans*-$IrCl(CO)(PPh_3)_2$)[48] as well as with Wilkinson's catalyst ($RhCl(PPh_3)_3$),[49] both of which coordinate with the oxygen functional groups on the CNTs.[16] Utilizing π-π interactions, Bassiouk and Rahman functionalized pristine CNTs with Ni, Co, Fe[50] and Zn[51] porphyrins (Figure 0.7).

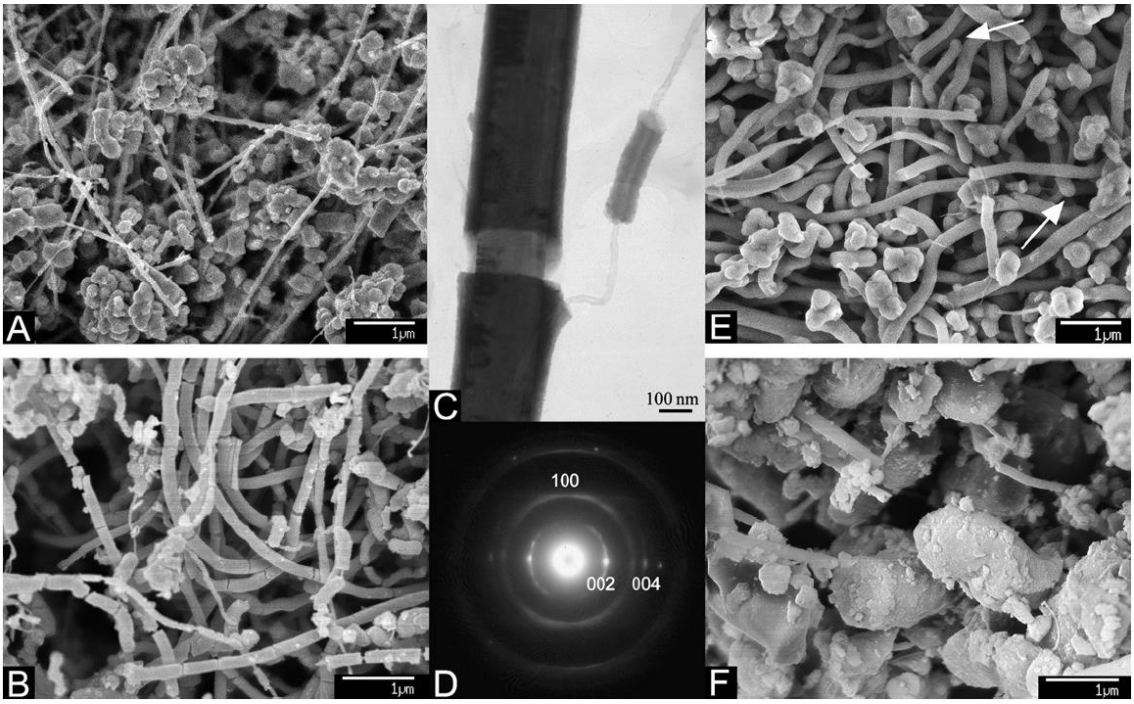

Figure 0.6. SEM images of TiO_2 grown on CNTs using a sol-gel process (a) without benzyl alcohol, (b) with benzyl alcohol and heated drying, (e) with benzyl alcohol and air drying and (f) using an *ex-situ* sol-gel process. A TEM image of the benzyl alcohol and heat dried sample is shown in (c), along with the electron diffraction pattern from that image showing a typical pattern from CNTs (d). Reprinted with permission from D. Eder and A. H. Windle, *J. Mater. Chem.*, 2008, **18**, 2036–2043.

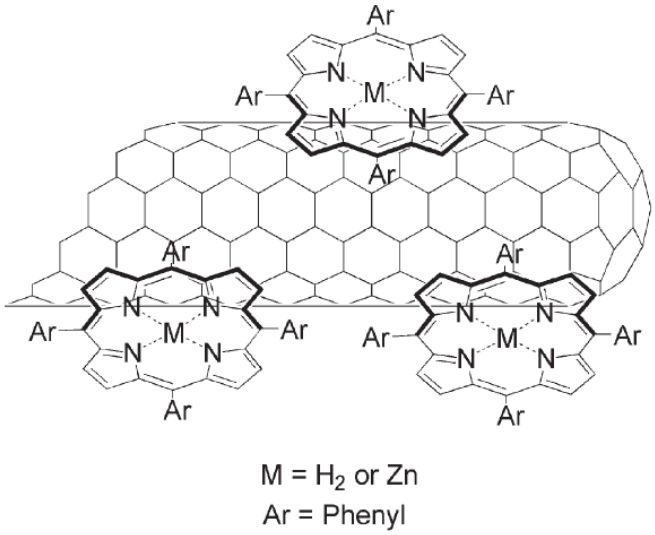

Figure 0.7. Functionalization of CNTs with porphyrin molecules through π-π interactions. Reprinted with permission from G. M. A. Rahman, D. M. Guldi, S. Campidelli and M. Prato, *J. Mater. Chem.*, 2006, **16**, 62–65.

Although the authors did not give an explanation for this behavior, it is interesting to note that the Co porphyrin was found to have the strongest interaction with the CNTs, forming helical structures of molecules around individual tubes.[50] The Ni and Fe porphyrins, however, were unable to debundle the CNTs and only interacted with the surface of CNT ropes.[50] In another example, CNTs were functionalized with a zinc phthalocyanine derivative by way of a pyrene linker ("ZnPc-py" in Figure 0.8).[52] Pyrene was specifically chosen because of its strong π-π interaction with CNTs (mentioned in the previous section).[32,52]

Direct metal particle and film functionalized CNTs. Due to the relative ease of generating metal particles directly on CNTs, there are many examples of this type of method. Probably the simplest examples are the deposition of metal particles from the gas

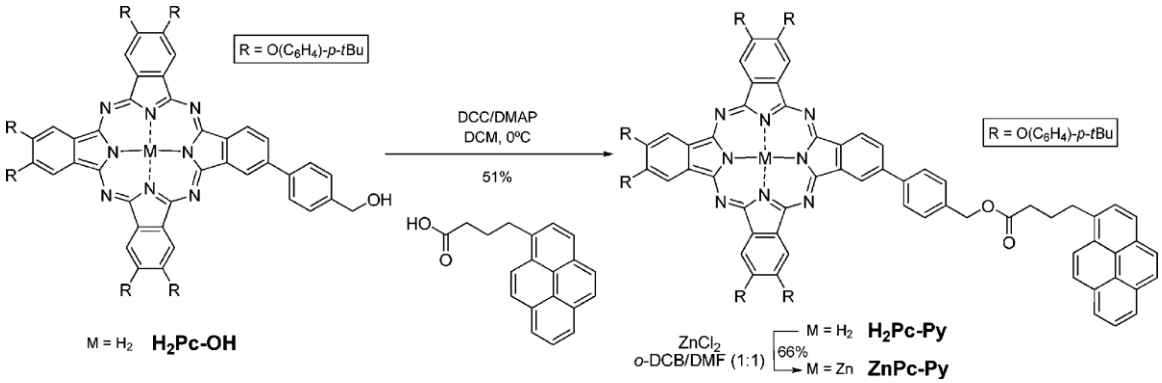

Figure 0.8. The synthesis of a pyrene derivative of zinc phthalocyanine. Reprinted with permission from J. Bartelmess, B. Ballesteros, G. de la Torre, D. Kiessling, S. Campidelli, M. Prato, T. Torres and D. M. Guldi, *J. Am. Chem. Soc.*, 2010, **132**, 16202–16211. Copyright 2010 American Chemical Society.

phase by evaporation, sputtering, CVD and ALD. As was previously mentioned, these methods are very useful for generating uniform films or particles on CNTs without disrupting structure of films or vertically aligned tubes.[15] In one particularly interesting report, the authors grew CNTs directly on transmission electron microscopy (TEM) grids and then deposited Ti, Ni, Pd, Au, Al and Fe on the CNTs using electron-beam deposition (Figure 0.9).[53] They found that Ti formed a continuous film on the CNTs, while Pd and Ni formed very small, well-dispersed particles.[53] But, Au, Al and Fe formed large islands of metal particles on the CNTs, which the authors reported were larger than the thickness of metal deposited.[53] These results give some information about the interactions of different metals with CNTs. Au, Al and Fe have a weak interaction, especially in the case of gold, as evidenced by their aggregation on the CNT surface.[53] Ni, Pd and Ti show strong interactions with CNTs, made obvious by their dispersion on the tubes.[53] In general, the interaction of the metal with CNTs is stronger with fewer

filled d orbitals, with the exception of Fe.[53] We speculate that empty d orbitals allow the metal to interact with the filled π orbitals of the CNTs.

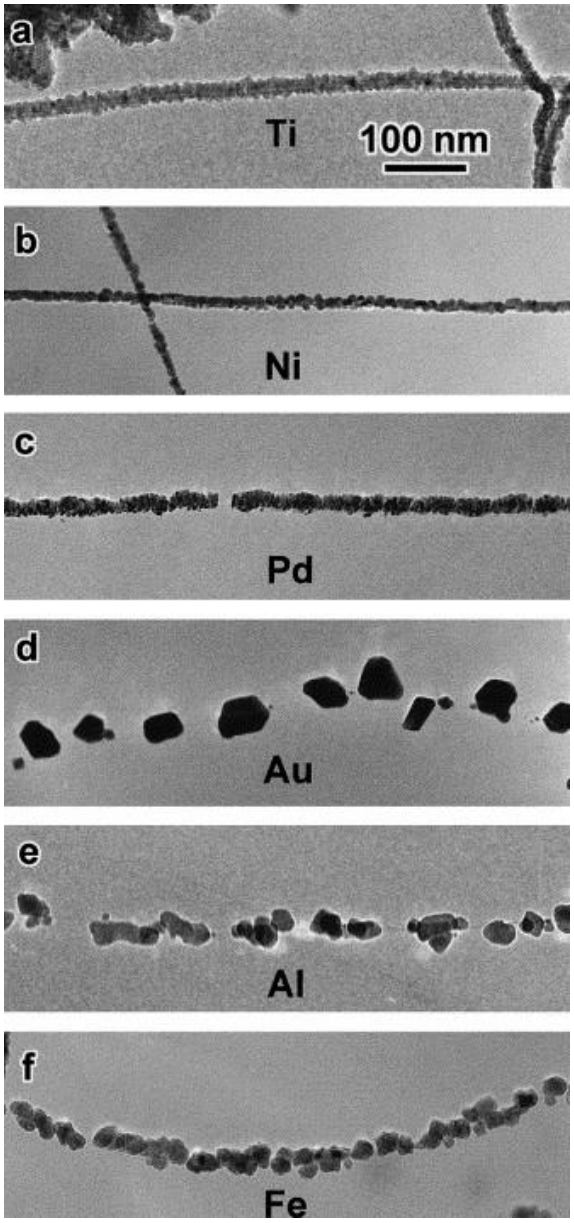

Figure 0.9. The deposition of different metals onto CNTs using an electron beam. Reprinted with permission from Y. Zhang, N. W. Franklin, R. J. Chen and H. Dai, *Chem. Phys. Lett.*, 2000, **331**, 35–41.

Another useful method for depositing metals on CNTs from the gas phase is by CVD. For example, a TiC layer was produced on CNTs by flowing acetylene gas over Ti-coated CNTs heated to 700 ˚C.[54] By using this method, the authors were able to make a high aspect ratio TiC structure (for field emission), which would be very challenging using other methods.[54] However, the authors also found that some CNTs were incompletely covered depending on their location in the film.[54]

Other groups have used sputtering to deposit metal particles on CNTs. This method is especially useful for the deposition of high melting temperature materials such as metal oxides. For example, Ru was sputtered in an O_2/Ar atmosphere to deposit RuO_2 on vertically aligned CNTs.[55] But, as this report exemplified, the disadvantage to using sputtering is the "shadowing" effect; the CNT tips were covered with 50 nm of RuO_2, which gradually decreased in thickness to expose bare nanotubes at the base of the sample.[55] Similar structures were reported when ZnO was sputtered on vertically aligned CNTs.[56] For films of CNTs, however, sputtering results in uniform deposition. For instance, individual CNTs were coated with a uniform film of ZrO_x, HfO_x, AlO_x, and ZnO_x by sputtering high purity metal pellets with a Nd:YAG (yttrium aluminum garnet) laser (in the presence of oxygen for the oxide materials).[57] Using the same method for the deposition of Au resulted in the formation of crystalline gold nanoparticles as a result of Au's mobility on the CNT surface.[57] On the contrary, the metal oxides were primarily amorphous due to their lack of mobility on CNTs.[57]

There are also many reports of metal particle deposition on CNTs using solution-based synthesis. A common method is electrodeposition, which has been used to deposit a variety of metals including Pt from H_2PtCl_6 or K_2PtCl_4,[36,37,58] Au from $HAuCl_4$,[36] Ag

from $AgNO_3$,[37] Pd from $(NH_4)_2PdCl_4$,[36] TiO_2 from $TiCl_3$,[59] and NiO_2/CoO_x from $Ni(NO_3)_2$ and $Co(NO_3)_2$.[60] Despite the fact that Pt, Au and Pd only adhere to the CNTs via van der Waals interactions, when deposited by electrodeposition, these metals remain adhered to the CNTs even after rinsing with water and blowing dry with nitrogen.[36] This method allows for control of particle size and distribution by adjusting the applied potential, deposition time and the metal salt concentration.[36,37] It also works well for selective metal deposition on CNT films that are on a non-conductive substrate.[37]

Chemical reduction has also been used to deposit metal nanoparticles directly on CNTs. As an example, CNTs have been functionalized with Pt nanoparticles by suspending them and a Pt precursor in supercritical CO_2, then reducing the precursor with H_2.[61] The resulting particles were reported to be between 5 and 10 nm and were dispersed fairly uniformly on the CNTs (Figure 0.10).[61] Additionally, this synthesis has the benefit of being very fast; the authors report a 15 minute reduction time.[61] Using a similar reduction with H_2, Takashi deposited Pt nanorods (with some rods being longer than 1 μm) inside CNTs by reducing a Pt precursor in CNTs grown in an aluminum oxide template with 30 nm channels (Figure 0.11).[62] And, using the same template, the authors were also able to completely fill the CNTs with Pt by reducing the Pt precursor with $NaBH_4$ (Figure 0.12).[62] Although the rods did not completely fill the CNTs, they were found to be highly crystalline, while the completely filled CNTs contained small Pt crystallites with various orientations.[62]

A particularly interesting solution-based method is hydrothermal deposition. Known for making very large single crystals of quartz, this method uses high pressures and temperatures to solubilize precursors in solution so that they may be recrystallized in

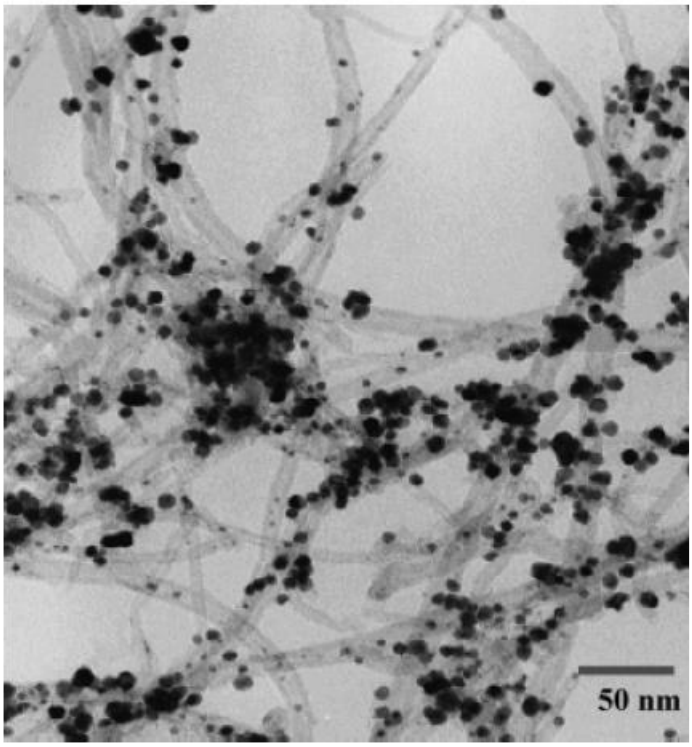

Figure 0.10. TEM image of Pt nanoparticles deposited on CNTs using H_2 reduction of a precursor in supercritical CO_2. Reprinted with permission from Y. Lin, X. Cui, C. Yen and C. M. Wai, *J. Phys. Chem. B*, 2005, **109**, 14410–14415. Copyright 2005 American Chemical Society.

a variety of different ways (interested readers see reference 63).[63] This method has been used to deposit crystalline ZnO nanowires on vertically aligned CNTs (with a thin ZnO seeding layer grown using sputtering techniques) in an autoclave at 100 ˚C.[56] Use of this method allowed for the preparation of unique brush-like composites with uniform ZnO nanowires along the length of the CNTs.[56]

Using a unique solution-based strategy, Sun was able to add ZnO nanoparticles to bare CNTs.[64] To accomplish this, the CNTs were dispersed using sodium dodecylbenzenesulfonate (NaDDBS) in an aqueous solution.[64] The CNT solution was

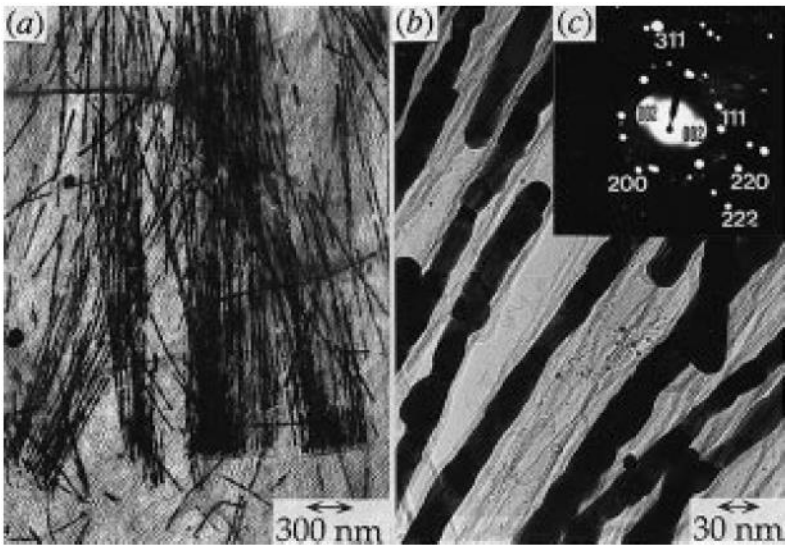

Figure 0.11. TEM images of (a) Pt nanorods deposited inside CNTs using an H_2 reduction method and (c) the electron diffraction pattern aquired from (b) the TEM image. Reprinted with permission from T. Kyotani, L. Tsai and A. Tomita, *Chem. Commun.*, 1997, 701–702.

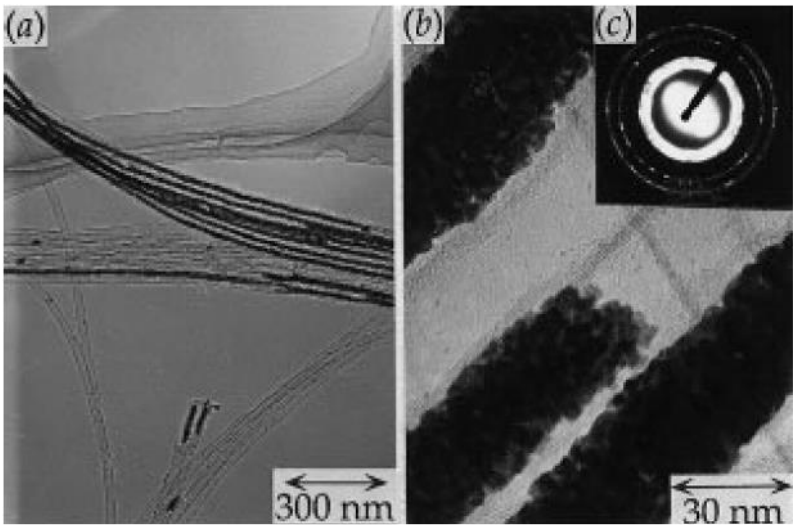

Figure 0.12. TEM images of (a) Pt particles deposited inside CNTs using an $NaBH_4$ reduction method and (c) the electron diffraction pattern aquired from (b) the TEM image. Reprinted with permission from T. Kyotani, L. Tsai and A. Tomita, *Chem. Commun.*, 1997, 701–702.

then added dropwise to a cyclohexane solution containing Triton X-114, generating small water droplets surrounded by Triton X and NaDDBS on the CNTs.[64] $Zn(O_2CMe)_2$ was then added to the solution.[64] Upon addition of a base, the Zn ions within the water droplets formed hollow $Zn(OH)_2$ particles (Figure 0.13).[64] These underwent calcination to form 5 nm solid ZnO particles on bare CNTs.[64] The authors reported similar results using $Mg(O_2CMe)_2$.[64]

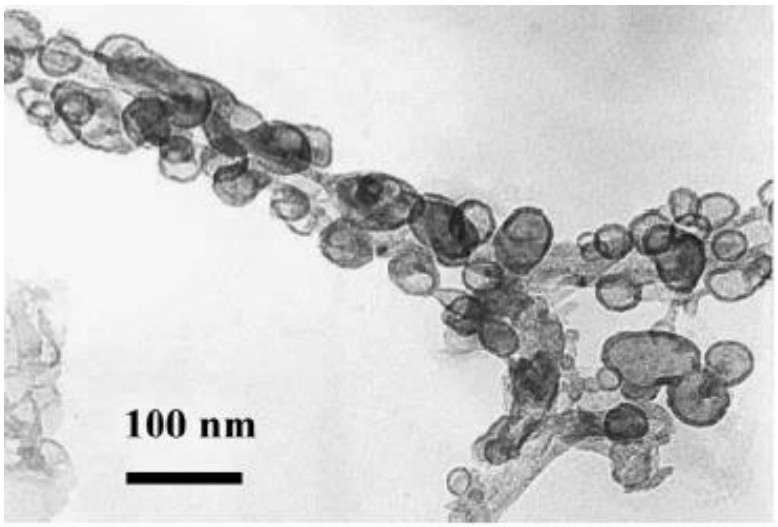

Figure 0.13. TEM image of hollow $Zn(OH)_2$ particles on CNTs. Reprinted with permission from J. Sun, L. Gao and M. Iwasa, *Chem. Commun.*, 2004, 832–833.

Direct metal atom functionalized CNTs. Comparing methods for functionalizing CNTs with metals, it is clear that direct functionalization of CNTs with metal atoms is the least common. To our knowledge, only two groups have reported such methods in the literature. The first report, published by Banerjee in 2002, directly functionalized CNTs with Vaska's complex (*trans*-$IrCl(CO)(PPh_3)_2$) by simply refluxing it with the raw CNTs in dimethylformamide (DMF).[48] They report that the Ir metal center

forms a dihapto (η^2) complex with the CNT without losing any preexisting ligands (Figure 0.14).[48] The second set of complexes found in the literature are hexahapto (η^6) metal complexes of CNTs reported by the Haddon group starting in 2011. By refluxing $(C_6H_6)Cr(CO)_3$ and $Cr(CO)_6$ with CNTs in tetrahydrofuran (THF), they reported the synthesis of $(C_6H_6)Cr(CNT)$ and $(CNT)Cr(CO)_3$, respectively.[65,66] They also reported formation of (CNT)Cr(CNT), (CNT)Mo(CNT) and (CNT)W(CNT) complexes by evaporating the respective metals on CNT films or by decomposing $(C_6H_6)Cr(CO)_3$ and $Cr(CO)_6$ under ultraviolet (UV) light in the presence of CNTs.[66,67] Because the Group 6 metals are mobile on the CNT surface, the authors reported that the metals migrate across the tubes until they come to a CNT-CNT junction, where they form two sets of hexahapto bonds between the tubes (Figure 0.15).[66] They also used this method to make similar *bis*-hexahapto lanthanum, neodymium, samarium, europium and gadolinium complexes of CNTs, which are stable under high vacuum up to 400 K.[68]

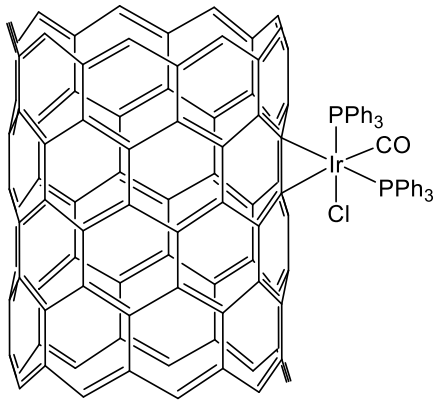

Figure 0.14. Functionalization of CNTs with Vaska's complex via a dihapto bond.

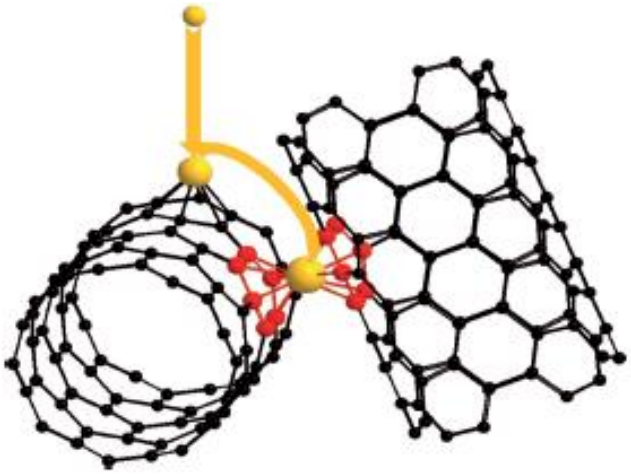

Figure 0.15. Upon evaporation of Group 6 metals on CNTs, the metals migrate to a CNT-CNT junction to form a (CNT)M(CNT) complex (M = Cr, Mo or W). Reprinted with permission from I. Kalinina, E. Bekyarova, S. Sarkar, F. Wang, M. E. Itkis, X. Tian, S. Niyogi, N. Jha and R. C. Haddon, *Macromol. Chem. Phys.*, 2012, **213**, 1001–1019.

Conclusions

The functionalization of CNTs with metals has been investigated using a wide range of methods, the most common of which is the deposition of metal particles and films both directly and indirectly on the CNTs. On the contrary, there are far fewer reports on the functionalization of CNTs with individual atoms. We speculate that the reasoning for this lies in the relative ease of depositing metal particles and films by sputtering, evaporation, chemical reduction, etc. where the CNTs are essentially treated as a surface to be coated. The addition of metal atoms is more challenging because the CNTs must be treated as molecules. Because the chemistry of CNTs is still not fully understood, adding metal atoms in a predictable manner is difficult. This is made even harder by the fact that CNTs are insoluble in most solvents, are difficult to purify, and are

not easily characterized by conventional methods used for organometallics. Thus, further investigation into the organometallic chemistry of CNTs is called for.

Because the entire field of direct metal atom functionalization of CNTs is dominated by the work of one research group, we became interested in expanding it. But, after finding inconsistencies in the Haddon Group's work, we primarily focused our efforts on further investigating the functionalization of pristine SWNTs with Group 6 metals. This work is discussed in Chapter 1. Besides these efforts, we were also interested in directly functionalizing pristine SWNTs with Cu(I), since it is known to complex to a variety of olefins.[69] But, after experiencing oxidation issues in our Group 6 metal endeavor as a result of residual catalyst materials and adsorbed oxygen, we decided to use C_{60} fullerene as a rough model for CNTs. Not only would this theoretically simplify the synthesis, but it would also simplify the characterization; C_{60} is easily characterized by nuclear magnetic resonance spectroscopy (NMR). In the case of Group 6 metal functionalization, we were unable to form hexahapto chromium complexes with C_{60}. Based on previous work, we concluded that this was a result of C_{60}'s high degree of curvature.[70,71] However, in the case of copper functionalization, our results did suggest the complexation of C_{60} to Cu(I), which also suggests Cu(I)'s ability to complex to very pure CNTs. A full discussion of the C_{60} work can be found in Chapter 2.

Lastly, we were also interested in functionalizing CNTs with zero-valent copper particles because of the recent success these composites have shown in improving CNT conductivity and ampacity.[6] To accomplish this, we chose to use chemical reduction to deposit copper particles on pyridine functionalized CNTs because of this methods tunability and capacity to generate well-dispersed particles. To our knowledge, pyridine

has not been used to anchor copper particles to CNTs before. We found that the Cu(II) precursor is absorbed by pyridine functionalized CNTs, suggesting that these groups act as seeding locations for the growth of the observed copper particles, and that these particles coordinate to the pyridine groups. This work is discussed in detail in Chapter 3.

References

1. S. Iijima, *Nature*, 1991, **354**, 56–58.
2. R. Sairo, G. Dresselhaus and M. S. Dresselhaus, *Physical Properties of Carbon Nanotubes*, Imperial College Press, London, 1998.
3. J. Park, S. Rosenblatt, Y. Yaish, V. Sazonova, H. Ustunel, S. Braig, T. A. Arias, P. W. Brouwer and P. L. McEuen, *Nano Lett.*, 2004, **4**, 517–520.
4. Y. Yaish, J. Park, S. Rosenblatt, V. Sazonova, M. Brink and P. L. McEuen, *Phys. Rev. Lett.*, 2004, **92**, 046401.
5. O. Hjortstam, P. Isberg, S. Soderholm and H. Dai, *Appl. Phys. A*, 2004, **78**, 1175–1179.
6. C. Subramaniam, T. Yamada, K. Kobashi, A. Sekiguchi, D. N. Futaba, M. Yumura and K. Hata, *Nat. Commun.*, 2013, **4**, 2202.
7. R. Saito, G. Dresselhaus and M. S. Dresselhaus, *Physical properties of carbon nanotubes*, Imperial College Press, London, Reprinted., 1999.
8. M.-F. Yu, B. S. Files, S. Arepalli and R. S. Ruoff, *Phys. Rev. Lett.*, 2000, **84**, 5552–5555.
9. H. M. Ledbetter, *J. Appl. Phys.*, 1981, **52**, 1587–1589.
10. A. A. Almusallam, *Construction and Building Materials*, 2001, **15**, 361–368.
11. S. Berber, Y.-K. Kwon and D. Tománek, *Phys. Rev. Lett.*, 2000, **84**, 4613–4616.

12. J. E. Graebner, S. Jin, G. W. Kammlott, J. A. Herb and C. F. Gardinier, *Appl. Phys. Lett.*, 1992, **60**, 1576–1578.

13. R. H. Baughman, A. A. Zakhidov and W. A. de Heer, *Science*, 2002, **297**, 787.

14. B. S. Harrison and A. Atala, *Biomaterials*, 2007, **28**, 344–353.

15. D. Eder, *Chem. Rev.*, 2010, **110**, 1348–1385.

16. S. Banerjee, M. G. C. Kahn and S. S. Wong, *Chem. Eur. J.*, 2003, **9**, 1898–1908.

17. Y.-P. Sun, K. Fu, Y. Lin and W. Huang, *Acc. Chem. Res.*, 2002, **35**, 1096–1104.

18. D. Tasis, N. Tagmatarchis, V. Georgakilas and M. Prato, *Chem. Eur. J.*, 2003, **9**, 4000–4008.

19. V. Georgakilas, D. Voulgaris, E. Vázquez, M. Prato, D. M. Guldi, A. Kukovecz and H. Kuzmany, *J. Am. Chem. Soc.*, 2002, **124**, 14318–14319.

20. K. L. Klein, A. V. Melechko, T. E. McKnight, S. T. Retterer, P. D. Rack, J. D. Fowlkes, D. C. Joy and M. L. Simpson, *J. Appl. Phys.*, 2008, **103**, 061301.

21. J. Liu, A. G. Rinzler, H. Dai, J. H. Hafner, R. K. Bradley, P. J. Boul, A. Lu, T. Iverson, K. Shelimov, C. B. Huffman, F. Rodriguez-Macias, Y.-S. Shon, T. R. Lee, D. T. Colbert and R. E. Smalley, *Science*, 1998, **280**, 1253–1256.

22. J. Zhang, H. Zou, Q. Qing, Y. Yang, Q. Li, Z. Liu, X. Guo and Z. Du, *J. Phys. Chem. B*, 2003, **107**, 3712–3718.

23. A. Kongkanand, R. Martínez Domínguez and P. V. Kamat, *Nano Lett.*, 2007, **7**, 676–680.

24. G.-X. Wang, B.-L. Zhang, Z.-L. Yu and M.-Z. Qu, *Solid State Ionics*, 2005, **176**, 1169–1174.

25. B. Liu, J. H. Chen, C. H. Xiao, K. Z. Cui, L. Yang, H. L. Pang and Y. F. Kuang, *Energy Fuels*, 2007, **21**, 1365–1369.

26. X. Li, J. Niu, J. Zhang, H. Li and Z. Liu, *J. Phys. Chem. B*, 2003, **107**, 2453–2458.

27. X. Xie and L. Gao, *Carbon*, 2007, **45**, 2365–2373.

28. B. R. Azamian, K. S. Coleman, J. J. Davis, N. Hanson and M. L. H. Green, *Chem. Commun.*, 2002, 366–367.

29. T. Sainsbury and D. Fitzmaurice, *Chem. Mater.*, 2004, **16**, 3780–3790.

30. K. Jiang, A. Eitan, L. S. Schadler, P. M. Ajayan, R. W. Siegel, N. Grobert, M. Mayne, M. Reyes-Reyes, H. Terrones and M. Terrones, *Nano Lett.*, 2003, **3**, 275–277.

31. S. Hrapovic, Y. Liu, K. B. Male and J. H. T. Luong, *Anal. Chem.*, 2004, **76**, 1083–1088.

32. V. Georgakilas, V. Tzitzios, D. Gournis and D. Petridis, *Chem. Mater.*, 2005, **17**, 1613–1617.

33. Y. Mu, H. Liang, J. Hu, L. Jiang and L. Wan, *J. Phys. Chem. B*, 2005, **109**, 22212–22216.

34. A. Gomathi, S. R. C. Vivekchand, A. Govindaraj and C. N. R. Rao, *Adv. Mater.*, 2005, **17**, 2757–2761.

35. Q. Kuang, S.-F. Li, Z.-X. Xie, S.-C. Lin, X.-H. Zhang, S.-Y. Xie, R.-B. Huang and L.-S. Zheng, *Carbon*, 2006, **44**, 1166–1172.

36. B. M. Quinn, C. Dekker and S. G. Lemay, *J. Am. Chem. Soc.*, 2005, **127**, 6146–6147.

37. T. M. Day, P. R. Unwin, N. R. Wilson and J. V. Macpherson, *J. Am. Chem. Soc.*, 2005, **127**, 10639–10647.

38. D.-J. Guo and H.-L. Li, *J. Electroanal. Chem.*, 2004, **573**, 197–202.

39. Z. He, J. Chen, D. Liu, H. Zhou and Y. Kuang, *Diamond Relat. Mater.*, 2004, **13**, 1764–1770.

40. R. Zanella, E. V. Basiuk, P. Santiago, V. A. Basiuk, E. Mireles, I. Puente-Lee and J. M. Saniger, *J. Phys. Chem. B*, 2005, **109**, 16290–16295.

41. C. Xu, G. Wu, Z. Liu, D. Wu, T. T. Meek and Q. Han, *Mater. Res. Bull.*, 2004, **39**, 1499–1505.

42. J. Cao, J. -Z. Sun, J. Hong, H. -Y. Li, H. -Z. Chen and M. Wang, *Adv. Mater.*, 2004, **16**, 84–87.

43. X. L. Li, Y. Q. Liu, L. Fu, L. C. Cao, D. C. Wei and Y. Wang, *Adv. Funct. Mater.*, 2006, **16**, 2431–2437.

44. H.-X. Wu, W.-M. Cao, Y. Li, G. Liu, Y. Wen, H.-F. Yang and S.-P. Yang, *Electrochim. Acta*, 2010, **55**, 3734–3740.

45. C. J. Brinker and G. W. Scherer, *Sol-gel science: the physics and chemistry of sol-gel processing*, Academic Press, Boston, 1990.

46. D. Eder and A. H. Windle, *J. Mater. Chem.*, 2008, **18**, 2036–2043.

47. J. H. Park, J. M. Ko and O. Ok Park, *J. Electrochem. Soc.*, 2003, **150**, A864.

48. S. Banerjee and S. S. Wong, *Nano Lett.*, 2002, **2**, 49–53.

49. S. Banerjee and S. S. Wong, *J. Am. Chem. Soc.*, 2002, **124**, 8940–8948.

50. M. Bassiouk, V. A. Basiuk, E. V. Basiuk, E. Álvarez-Zauco, M. Martínez-Herrera, A. Rojas-Aguilar and I. Puente-Lee, *Appl. Surf. Sci.*, 2013, **275**, 168–177.

51. G. M. A. Rahman, D. M. Guldi, S. Campidelli and M. Prato, *J. Mater. Chem.*, 2006, **16**, 62–65.

52. J. Bartelmess, B. Ballesteros, G. de la Torre, D. Kiessling, S. Campidelli, M. Prato, T. Torres and D. M. Guldi, *J. Am. Chem. Soc.*, 2010, **132**, 16202–16211.

53. Y. Zhang, N. W. Franklin, R. J. Chen and H. Dai, *Chem. Phys. Lett.*, 2000, **331**, 35–41.

54. L. Pan, T. Shoji, A. Nagataki and Y. Nakayama, *Adv. Eng. Mater.*, 2007, **9**, 584–587.

55. J.-S. Ye, H. Cui, X. Liu, T. Lim, W.-D. Zhang and F.-S. Sheu, *Small*, 2005, **1**, 560–565.

56. Wei-De Zhang, *Nanotechnol.*, 2006, **17**, 1036.

57. T. Ikuno, T. Yasuda, S. Honda, K. Oura, M. Katayama, Jung-Goo Lee and H. Mori, *J. Appl. Phys.*, 2005, **98**, 114305.

58. C. Wang, M. Waje, X. Wang, J. M. Tang, R. C. Haddon and Yan, *Nano Lett.*, 2004, **4**, 345–348.

59. O. Frank, M. Kalbac, L. Kavan, M. Zukalova, J. Prochazka, M. Klementova and L. Dunsch, *Phys. Status Solidi B*, 2007, **244**, 4040–4045.

60. H. Kuan-Xin, W. Quan-Fu, Z. Xiao-gang and W. Xin-Lei, *J. Electrochem. Soc.*, 2006, **153**, A1568.

61. Y. Lin, X. Cui, C. Yen and C. M. Wai, *J. Phys. Chem. B*, 2005, **109**, 14410–14415.

62. T. Kyotani, L. Tsai and A. Tomita, *Chem. Commun.*, 1997, 701–702.

63. A. Rabenau, *Angew. Chem. Int. Ed. Engl.*, 1985, **24**, 1026–1040.

64. J. Sun, L. Gao and M. Iwasa, *Chem. Commun.*, 2004, 832–833.

65. S. Sarkar, S. Niyogi, E. Bekyarova and R. C. Haddon, *Chem. Sci.*, 2011, **2**, 1326–1333.

66. I. Kalinina, E. Bekyarova, S. Sarkar, F. Wang, M. E. Itkis, X. Tian, S. Niyogi, N. Jha and R. C. Haddon, *Macromol. Chem. Phys.*, 2012, **213**, 1001–1019.

67. A. Pekker, M. Chen, E. Bekyarova and R. C. Haddon, *Mater. Horiz.*, 2015, **2**, 81–85.

68. M. L. Moser, X. Tian, A. Pekker, S. Sarkar, E. Bekyarova, M. E. Itkis and R. C. Haddon, *Dalton T.*, 2014, **43**, 7379–7382.

69. J. J. Allen and A. R. Barron, *Dalton T.*, 2009, 878–890.

70. R. C. Haddon, *Science*, 1993, **261**, 1545–1550.

71. R. C. Haddon, *J. Comput. Chem.*, 1998, **19**, 139–143.

Chapter 1

Are Hexahapto-Metal Complexes of Group 6 Metals Formed on Single-Walled Carbon Nanotubes?

Introduction

The *bis*-hexahapto sandwich complex, *bis*(benzene)chromium, is a well-studied molecule in the literature. It has been shown through density functional theory that *bis*(benzene)chromium has a dissociation energy 30 times higher than (benzene)chromium.[1] This stability can be attributed to the fact that each benzene ring contributes 6 π electrons to the d^5s^1 metal, making a very stable 18 electron system.[1] Similarly, the benzenoid rings in a SWNT should also contribute 6 electrons to chromium or any of the other Group 6 metals (molybdenum and tungsten) to make a stable complex. Hexahapto functionalization of SWNTs is desirable, because it does not break the sp^2 hybridization of the tubes or significantly alter the electronic structure. This is imperative for the use of SWNTs in electronics applications, since it has been shown that a decrease in the delocalization through the formation of sp^3 hybridized carbons results in higher resistance.[2] Further, theoretical calculations have shown that there is no potential barrier between a semiconducting SWNT and a molybdenum contact, indicating that electrons flow freely between the two.[3] Thus, the formation of Group 6 metal-SWNT sandwich complexes may allow for the formation of interesting composites without disrupting the tubes inherent conductivity. Additionally, these sandwich complexes have the potential to act as an electronic bridge between the resistive metallic SWNT and semiconducting SWNT (mSWNT-sSWNT) junctions present in bundles of tubes.[4,5]

The Haddon group at University of California, Riverside has published multiple papers on this subject. In 2011, they reported the synthesis of $(C_6H_6)Cr(SWNT)$ by reacting electric arc SWNTs with $(C_6H_6)Cr(CO)_3$.[6] In 2012, they reported the formation of $(SWNT)Cr(CO)_3$ and $Cr(SWNT)_2$ by reacting SWNTs with $Cr(CO)_6$ and by evaporating chromium on SWNTs, respectively.[5] For films of their $Cr(SWNT)_2$ sandwich complex, they reported an increase in conductivity of over 100%, supporting the hypotheses made in the previous paragraph.[4] They also reported conductivity increases for tungsten and molybdenum sandwich complexes synthesized by the same method.[5]

We were very interest in this work, and sought to expand it by determining how the Group 6 metal concentration on the SWNTs affects their conductivity. However, we found that we could not synthesize the reported complexes using the Haddon Group's solution-based reactions; all of our SWNTs were functionalized with chromium oxides. Upon further investigation into the Haddon Group's work, we found several gaps in their characterization that justified a study of the system. For instance, they used X-ray photoelectron spectroscopy (XPS) to determine the oxidation state of their chromium-functionalized SWNTs, stating that the binding energy of the Cr $2p_{3/2}$ and $2p_{1/2}$ signals were 576.9 eV and 586.5 eV, respectively (Figure 1.1).[5] This corresponds to a spin-orbit splitting of 9.7 eV.[5] They also reported a full width half max (FWHM) of 2.3-2.7 eV for these signals.[5] The literature reports that the Cr $2p_{3/2}$ peak of $(C_6H_6)Cr(CO)_3$ occurs at 576.1 eV and the corresponding peak for $(C_6H_6)Cr(C_6H_6)$ occurs at 575.2 eV.[7] Thus, the reported value of 576.9 eV is too high for a $(SWNT)Cr(CO)_3$ or $(SWNT)Cr(C_6H_6)$ complex, which the authors reported at the same binding energy. But, this alone is not enough to argue that their assignment is incorrect. To this end, the literature also reports a

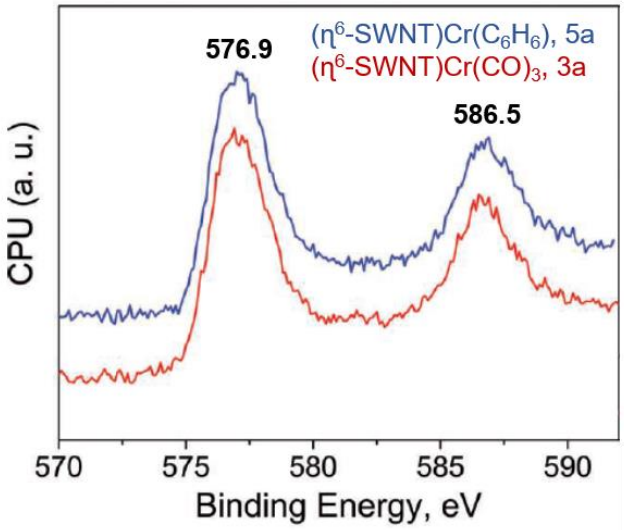

Figure 1.1. The Cr 2p XPS of (SWNT)Cr(C_6H_6) (blue) and (SWNT)Cr($CO)_3$ (red). Reprinted with permission from I. Kalinina, E. Bekyarova, S. Sarkar, F. Wang, M. E. Itkis, X. Tian, S. Niyogi, N. Jha and R. C. Haddon, *Macromol. Chem. Phys.*, 2012, **213**, 1001–1019.

multi-peak structure for the Cr 2p spectra of $Cr(CO)_6$ and (C_6H_6)Cr($CO)_3$ from shake-up-shake-off processes, which are indicated by arrows in Figure 1.2a and b, respectively.[7] The Haddon Group's Cr 2p spectra of the product they reported as (SWNT)Cr($CO)_3$ does not have these shake up peaks despite having the same local structure as (C_6H_6)Cr($CO)_3$. Further, another report indicated that the FWHM of the $2p_{3/2}$ peak for zero-valent chromium is between 1.8 and 2.3 eV and the distance between the $2p_{3/2}$ and the $2p_{1/2}$ peaks is between 8.7 and 9.2 eV.[8] For Cr_2O_3, these values are 3.0 eV and 9.7 eV, respectively.[8] Looking again at the values Haddon reports (2.3-2.7 eV and 9.7 eV, respectively), it is arguable that these peaks are indicative of Cr_2O_3, especially given its Cr $2p_{3/2}$ binding energy of 576.8 eV at the most intense point of the signal.[8] Finally, the infrared (IR) spectroscopy of the species assigned (SWNT)Cr($CO)_3$ is reported to show a

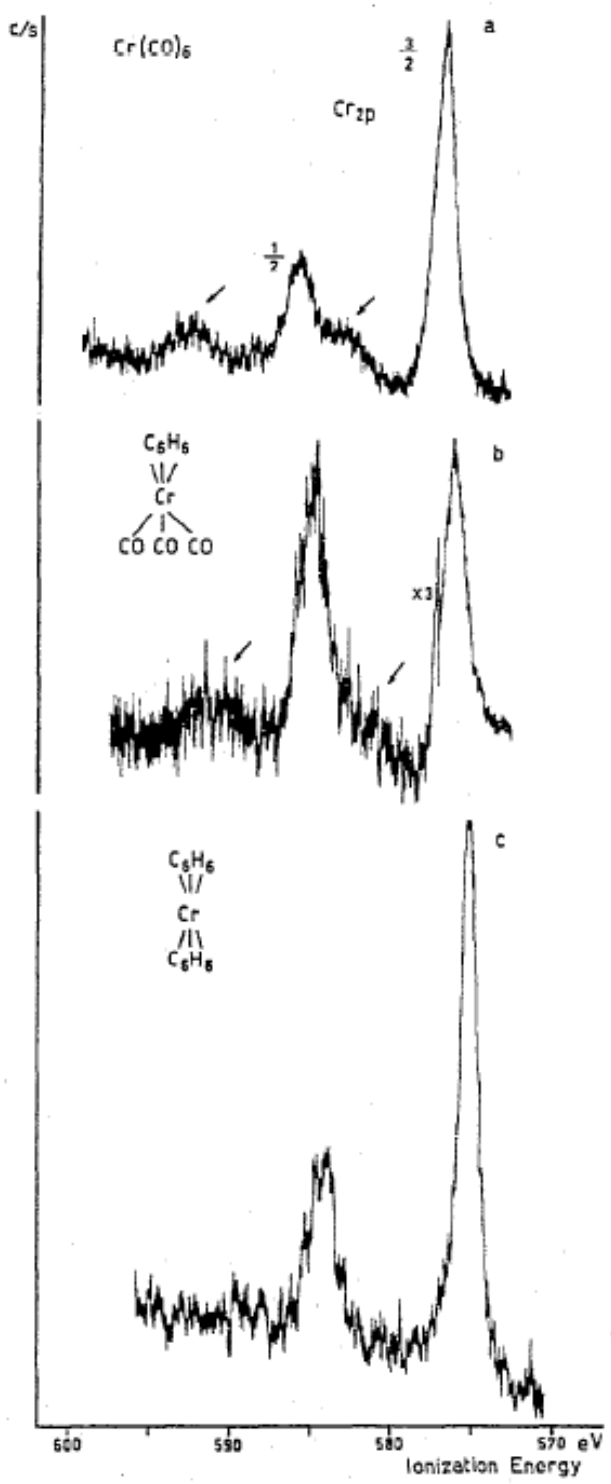

Figure 1.2. The Cr 2p XPS spectra of (a) $Cr(CO)_6$, (b) $(C_6H_6)Cr(CO)_3$, and (c) $(C_6H_6)Cr(C_6H_6)$. Reprinted with permission from S. Pignataro, A. Foffani and G. Distefano, *Chem. Phys. Lett.*, 1973, **20**, 350–355.

single signal for the carbonyls at 1971 cm^{-1}.[5] The local environment of (SWNT)$Cr(CO)_3$ corresponds to a $(C_6H_6)Cr(CO)_3$ structure, which has a C_{3v} symmetry.[9] With this symmetry, the A_1 and E vibration modes are IR-active; therefore, two bands are seen in the $(C_6H_6)Cr(CO)_3$ spectra.[9] Because Haddon's IR only shows a single band in the carbonyl region, the assignment of (SWNT)$Cr(CO)_3$ is not supported. Indeed, the observation of a single peak is more in line with the presence of unreacted $Cr(CO)_6$ starting material, which shows a single signal at 2000 cm^{-1}.[5] Although the Haddon Group's signal is shifted to lower wavenumbers, the literature shows that physisorption of this molecule can lead to shifts in its vibrational frequency.[10,11] However, we do acknowledge that these spectra were obtained using an attenuated total reflectance (ATR) setup, and that the resulting decrease in resolution may make the observation of two peaks more difficult.

In trying to repeat the Haddon Group's work, we found that the reported Group 6 metal-SWNT complexes are very sensitive to oxidation during synthesis. Even after using freshly distilled solvents and inert atmosphere techniques, our efforts resulted in metal oxides. After further investigation, we found that acid-treating and annealing the SWNTs reduced the amount of Group 6 metal oxides formed and allowed for the synthesis of zero-valent metals. Because annealing and treating with acid have been shown to reduce oxygen functional groups and residual growth catalyst on SWNTs,[12–14] we conclude that the removal of any reactive oxygen is necessary for the success of this reaction.

Although the elimination of reactive oxygen functional groups from the SWNTs is fairly obvious, the removal of residual growth catalyst is not. However, a literature

search revealed that other research has been complicated by the residual catalyst material as well. In trying to determine their toxicity in the body, multiple groups have found that exposure to SWNTs results in oxidative stress, indicated by the formation of free radicals and buildup of peroxidative products.[15,16] Eventually, the antioxidants that normally keep these reactive oxygen species in check become depleted, and the cell dies.[15,16] In these studies, however, the CNT preparation contained a large concentration of iron and nickel growth catalysts.[15,16] It was found that these catalyst materials are key players in causing the oxidative stress in biological systems as a result of their ability to redox-cycle.[15,16] Although the study of nanotubes in biological systems is very different from the comparatively simple system under investigation here, this example illustrates the significance of the residual catalyst materials and exemplifies the need for further investigation into their effects on chemical systems. Indeed, the only examples we found regarding unexpected outcomes as a result of residual catalyst materials were in toxicity reports.

Results and Discussion

Synthesis of Group 6 metal complexes. In an effort to maximize the metal concentrations on the SWNTs, $(MeCN)_3M(CO)_3$ and $(C_7H_8)M(CO)_3$ (M = Cr, W) were synthesized. This is due to the more labile nature of the ligands as compared to CO in $M(CO)_6$. The syntheses were carried out by a modification of the literature procedures.[17]

The acetonitrile complexes are made by refluxing the appropriate *hexa*-carbonyl complex, $M(CO)_6$, in acetonitrile for multiple days, producing a mixture of very air-sensitive, yellow products (Figure 1.3). The IR spectra of the crude products are in agreement with the literature and are shown in Figure 1.4 and Figure 1.5.[18] In the case of

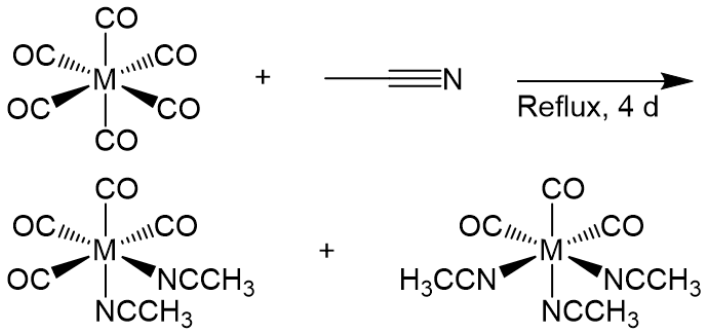

Figure 1.3. The reaction scheme for the synthesis of $(CH_3CN)_2M(CO)_4$ and $(CH_3CN)_3M(CO)_3$ (M = Cr or W).

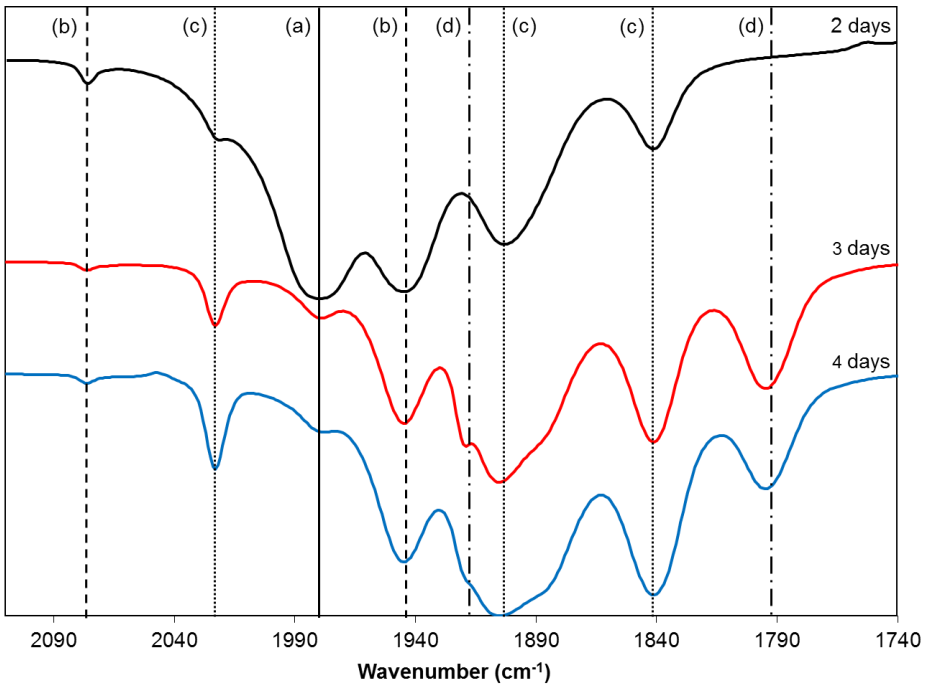

Figure 1.4. The solution IR spectrum in the carbonyl region of the crude product of the reaction between $Cr(CO)_6$ and acetonitrile analyzed after 2, 3 and 4 days of reaction. Peaks are assigned as (a) $Cr(CO)_6$, (b) $(MeCN)Cr(CO)_5$, (c) $(MeCN)_2Cr(CO)_4$, and (d) $(MeCN)_3Cr(CO)_3$.

the Cr derivative, it was found that longer reaction times result in a notable reduction of the mono-substituted product, as well as the starting material, based on the decreasing intensities of their peaks relative to other species, see Figure 1.4. However, it was also found that longer reaction times do not substantially reduce the di-substituted product, $(CH_3CN)_2Cr(CO)_4$. The residual mono-substituted product is easily separated from the mixture by extraction with hexane. The di- and tri-substituted products, on the other hand, are very difficult to separate, especially in the case of W; the tri-substituted product decomposes readily despite being kept under an inert atmosphere, making crystallization a challenge.[19] Because of this and the fact that using the di- and tri-substituted mixture did not appear to negatively affect later syntheses, the product mixture was used as is immediately after it was produced.

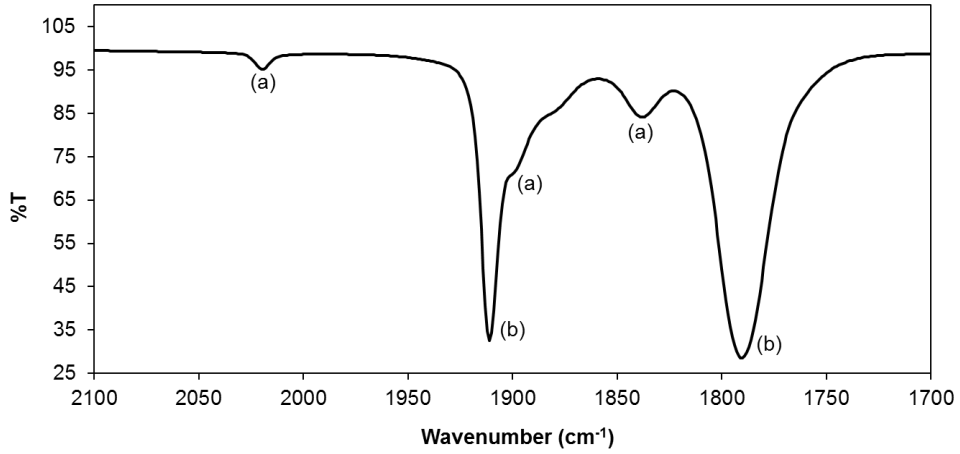

Figure 1.5. The solution IR spectrum in the carbonyl region of the crude product of the reaction of $W(CO)_6$ with acetonitrile after 4 days of reflux. Peaks are assigned as (a) $(MeCN)_2W(CO)_4$ and (b) $(MeCN)_3W(CO)_3$.

The cycloheptatriene derivatives $(C_7H_8)M(CO)_3$ (M = Cr, W) are easily synthesized by adding cycloheptatriene to the as prepared MeCN product and refluxing in

hexane to produce a dark red solution (Figure 1.6). The air stable $(C_7H_8)M(CO)_3$ product can then be easily purified by sublimation. These products were characterized by IR spectroscopy, showing three C=O stretches in agreement with the literature (Figure 1.7).[20,21]

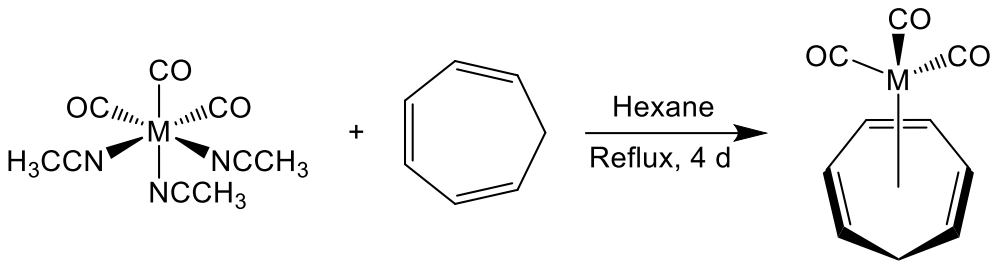

Figure 1.6. The reaction scheme for the synthesis of $(C_7H_8)M(CO)_3$.

Reaction of Group 6 complexes with raw SWNTs. Functionalization of SWNTs using various Cr and W complexes was attempted, but proved to be very challenging. Part of the challenge lies in the difficulty of characterizing the SWNT products. Unfortunately, the features in IR spectra suffer from low intensities as a result of the SWNTs dynamic dipole moment.[22] This issue is exacerbated by the similar refractive indexes of SWNTs and the ATR diamond window that was available. X-ray photoelectron spectroscopy (XPS), a technique commonly used to characterize metal species (and in particular changes in oxidation state), is challenging in and of itself due to the variety of ways that signals can be interpreted using curve fitting. XPS is especially challenging in this case, because many chromium and tungsten species have complex satellite peaks that are difficult to fit. Additionally, the identity and concentration of the oxygen species present on the SWNT walls vary widely. Therefore, characterization using the oxygen signals gives inconsistent results that are difficult to interpret.

Furthermore, the HiPco SWNTs used in this study contain residual catalyst present as iron oxides, which have overlapping oxygen signals with the Group 6 metal oxides that may form during functionalization. Despite these issues, XPS is still the best method in this case, and it was used cautiously to characterizing Group 6 metal-functionalized SWNTs.

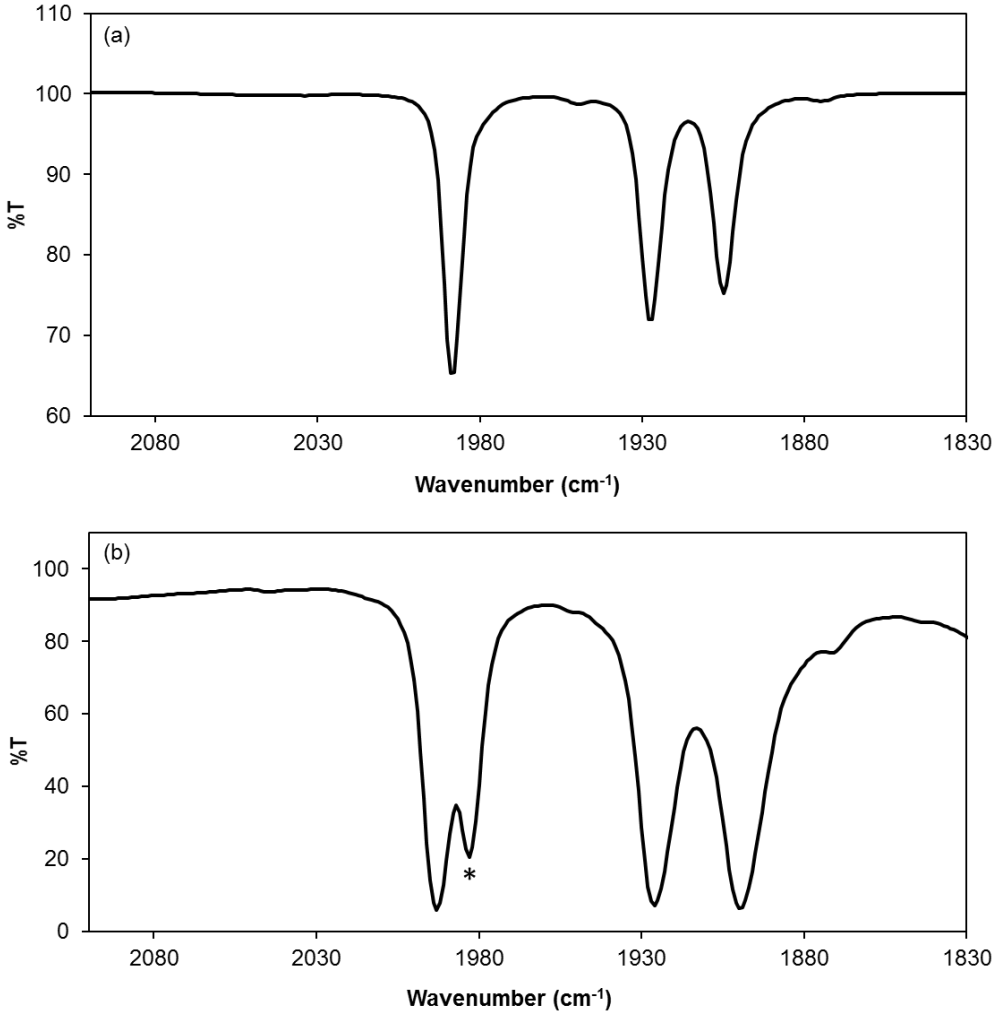

Figure 1.7. The IR spectra of the carbonyl region for (a) $(C_7H_8)Cr(CO)_3$ and (b) $(C_7H_8)W(CO)_3$. The peak indicated by * is due to unreacted $W(CO)_6$.

SWNTs were reacted with $Cr(CO)_6$, $W(CO)_6$, $(C_7H_8)Cr(CO)_3$, $(C_7H_8)W(CO)_3$, and $(C_6H_6)Cr(CO)_3$ (Figure 1.8) with the goal being to maximizing the amount of zero-valent Group 6 metals deposited on the SWNTs. However, all of the reactions resulted in the formation of Group 6 metal oxides, as indicated by the binding energies of the XPS signals shown in Table 1.1. A comparison of these values for the chromium reactions to those found in the literature for various chromium species in Table 1.2 shows that the binding energies of the obtained chromium products are too high to be zero-valent complexes and fall in the range of Cr_2O_3. These results suggest that the reaction of any of the Cr carbonyls with the HiPco SWNTs results in a Cr(III) species. However, the XPS analysis also shows a curve around 576.1 eV for all three Cr products, which may be indicative of the formation of $(SWNT)Cr(CO)_3$. The FWHM of all three of these peaks is 1.45 eV, which is nearly within the range reported for zero-valent chromium (1.8 to 2.3 eV).[8] But, as this example illustrates, benzenoid chromium tricarbonyl species overlap

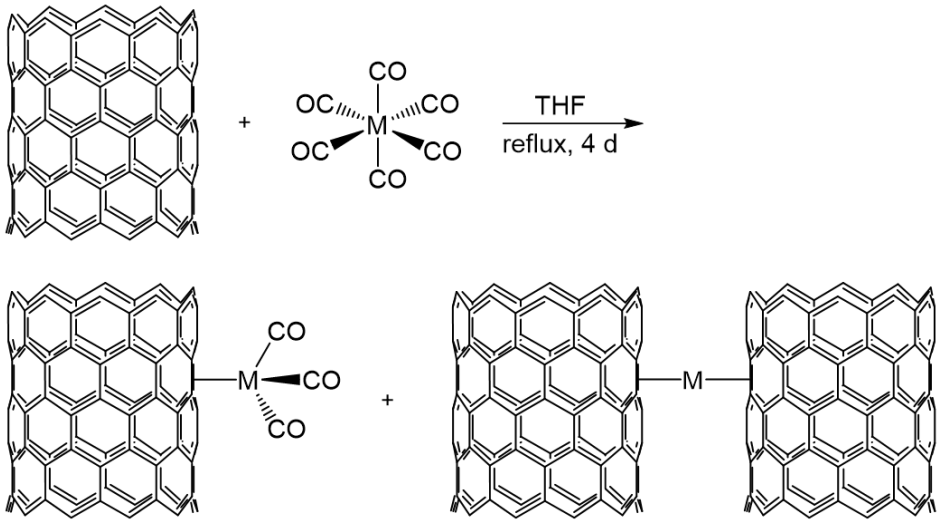

Figure 1.8. The reaction scheme for the functionalization of SWNTs with Group 6 metals (M = Cr or W).

Table 1.1. Observed XPS Cr $2p_{3/2}$ and W $4d_{5/2}$ binding energies and atomic percentages for reactions of SWNTs with various reagents.

Reagent	Cr $2p_{3/2}$ (eV)	W $4d_{5/2}$ (eV)	M%
$(C_6H_6)Cr(CO)_3$	576.2, 577.4, 578.9		1.70
$Cr(CO)_6$	576.0, 577.3, 578.9		3.5
$(C_7H_8)Cr(CO)_3$	576.1, 577.3, 578.9		5.01
$W(CO)_6$[a]		247.8	1.01
$W(CO)_6$[b]		247.5	2.51
$(C_7H_8)W(CO)_3$		247.7	4.54

[a]Large scale reaction. [b]Small scale reaction.

Table 1.2. The literature values of the XPS Cr $2p_{3/2}$ and W $4d_{5/2}$ binding energies for various chromium and tungsten species of interest.

Cr Complex	Cr $2p_{3/2}$ (eV)	W Complex	W $4d_{5/2}$ (eV)
Cr^0 (metal)	574.2[23]	W^0 (metal)	244.2[24]
$(C_6H_6)Cr(C_6H_6)$	575.2[7]	$W(CO)_6$	247.8[25]
$(C_6H_6)Cr(CO)_3$	576.1[7]	WO_3	248[26]
$Cr(CO)_6$	576.8[7]		
Cr_2O_3[a]	575.7-578.9[8]		
CrO_3	579.6[8]		

[a]The binding energy of the most intense portion of the peak without curve fitting is 576.8.[8]

with chromium(III) oxide (Table 1.2), making XPS identification especially difficult. This is further complicated by the fact that chromium(III) species have multiplet splitting in XPS, which makes curve fitting to determine oxidation states very challenging.[23] In a similar manner, the W $4d_{5/2}$ binding energies from all analogous reactions (Table 1.1) appear to be more similar to that of WO_3 rather than W^0 or $(SWNT)W(CO)_3$ (Table 1.2),

assuming that the binding energy of benzenoid tungsten tricarbonyls would decrease from the $W(CO)_6$ binding energy similarly to the chromium analogues.[24,26] This is consistent with complete oxidation of any adsorbed W containing species. Despite the oxidation of the products, it is interesting to note that the metal concentration on the SWNTs is the highest for the reactions with $(C_7H_8)M(CO)_3$ (M = Cr, W), rather than the reactions with $M(CO)_6$ or $(C_6H_6)Cr(CO)_3$. This suggests that the cycloheptatriene derivatives are indeed more reactive than the other starting materials,[27,28] making them the best choice for maximizing SWNT functionalization.

As was previously discussed, the Haddon Group reported a Cr $2p_{3/2}$ binding energy for $(SWNT)Cr(CO)_3$ to be 576.9 eV as being consistent with Cr(0) η^6-complexes;[5] however, the accepted value for $(C_6H_6)Cr(CO)_3$ is 576.1 eV.[7] We note that they also reported the binding energy for Cr_2O_3 to be 575.5 eV, which does not fall within the accepted literature values of 575.7-578.9 eV.[23] In the prior work[5], SEM images were used to suggest the formation of increased bundle size as an indicator of interconnects, while TEM images showed surface particles of ca. 1 nm despite the chromium atom having a diameter closer to 0.424 nm.[29] TEM of our samples show similar particulates (Figure 1.9), but these are difficult to differentiate from the residual catalyst materials on raw HiPco SWNTs (Figure 1.10). Given these discrepancies and those discussed in the introduction to this chapter, we are interested in determining if $Cr(\eta^6\text{-SWNT})_2$ or $(\eta^6\text{-SWNT})Cr(CO)_3$ are actually formed under these conditions.

The presence of oxidized products could be put down to the reaction with adventitious oxygen; however, since careful air-free techniques (including the use of degassed THF distilled over sodium/benzophenone) were used in the reactions, it was

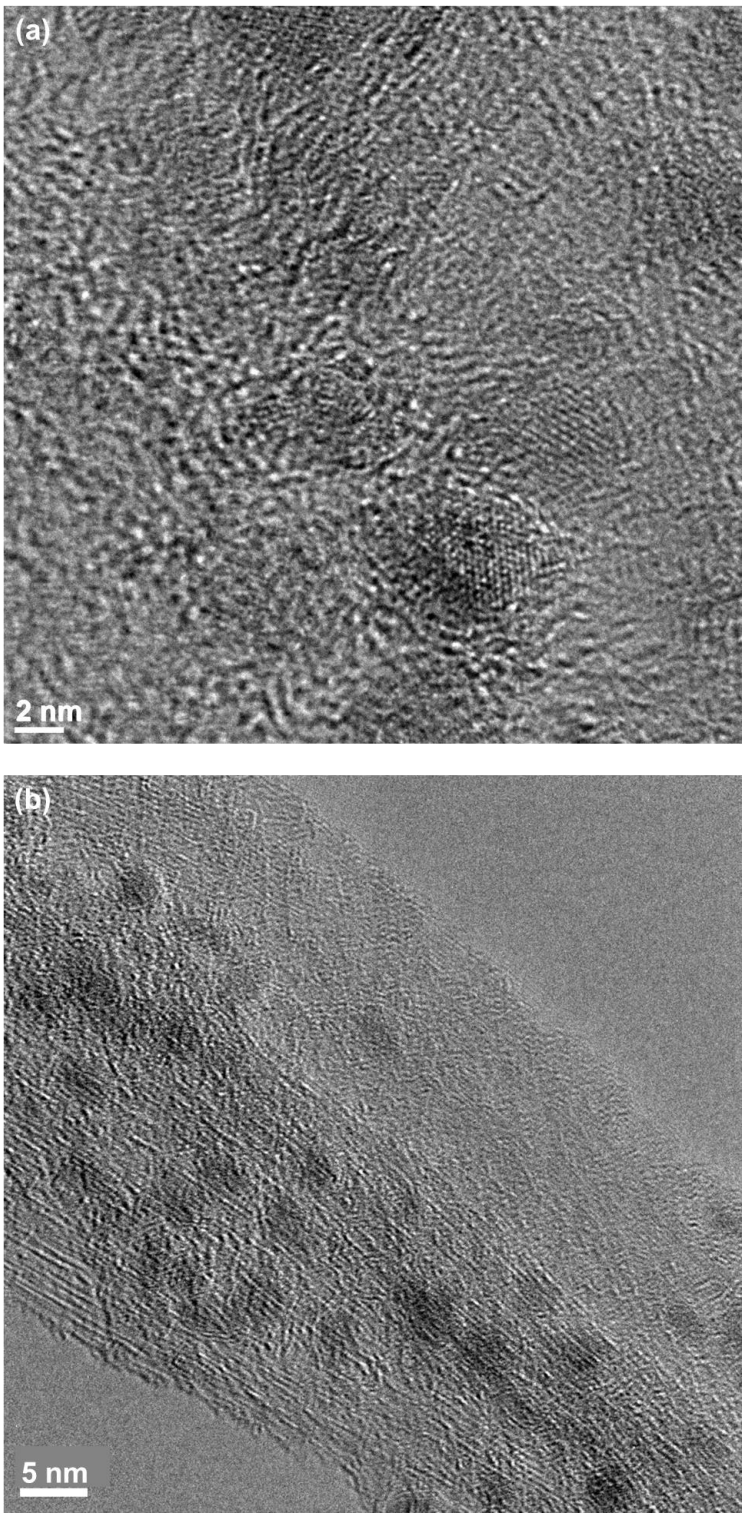

Figure 1.9. TEM image of the product from the reaction of (a) $W(CO)_6$ and (b) $(C_6H_6)Cr(CO)_3$ with raw HiPco SWNTs.

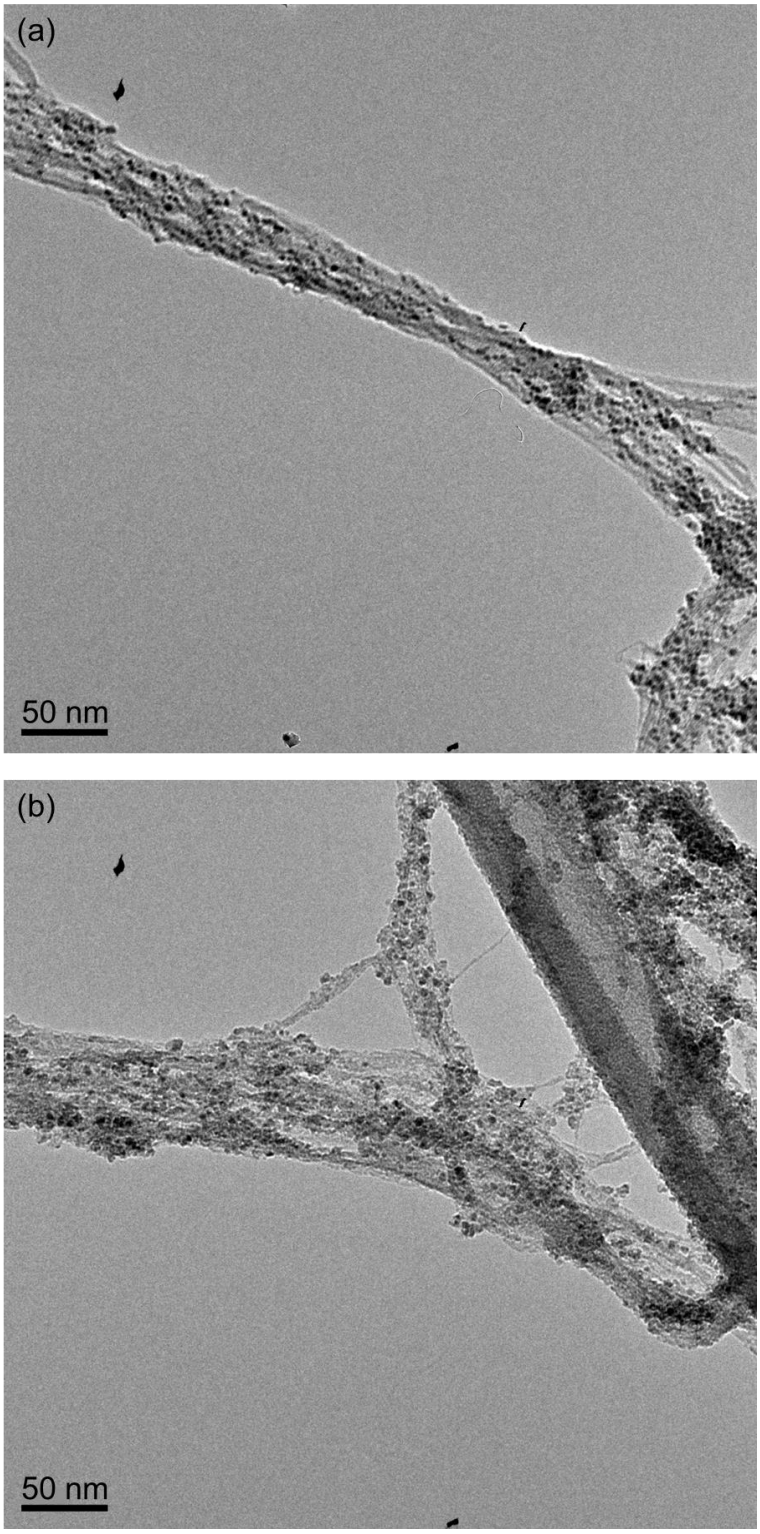

Figure 1.10. TEM image of (a) raw HiPco SWNTs and (b) the product from the reaction of $(C_6H_6)Cr(CO)_3$ with raw HiPco SWNTs.

hypothesized that the Group 6 metal oxidation was occurring with the oxygen impurities that are present on the outside of the SWNTs.[30] To prevent this, the oxygen was removed from the SWNTs by annealing them at 550 °C in an inert atmosphere.[13,14] This did not solve the oxidation problem. As noted in the introduction, we have been concerned with issues associated with the presence of residual catalyst particles in SWNTs with regard to any meaningful investigation of their reactivity. Based upon prior work, we suggested that the presence of oxidized Cr and W species is due to reaction with the iron oxide catalyst residue that is commonly present.[15,16] Consideration of the standard reduction potentials (Table 1.3) show that iron is larger than chromium, indicating that iron oxides could be causing the oxidation of zero valent chromium.[31,32] Prediction of the redox chemistry between iron and tungsten based on the standard reduction potentials (Table 1.3) is not possible. The potentials for elemental tungsten cannot be obtained

Table 1.3. Selected standard reduction potentials.

Reaction	E^0 (V)
$Fe^{3+} + e^- \rightarrow Fe^{2+}$	+0.77[31]
$Fe^{3+} + 3e^- \rightarrow Fe$	-0.04[31]
$Fe^{2+} + 2e^- \rightarrow Fe$	-0.44[31]
$Cr^{3+} + e^- \rightarrow Cr^{2+}$	-0.42[31]
$Cr^{3+} + 3e^- \rightarrow Cr$	-0.74[31]
$Cr^{2+} + 2e^- \rightarrow Cr$	-0.90[31]
$WO_4^{2-} + 4H_2O + 6e^- \rightarrow W(s) + 8OH^-$*	-1.074[33]
$WO_3(s) + 6H^+ + 6e^- \rightarrow W(s) + 3H_2O(l)$‡	-0.090[33]

* Reduction performed in alkali solution, ‡ reduction performed in acidic solution.

experimentally due to the formation of a conductive tungsten intermediate on the cathode, which is difficult to fully reduce and also acts as a catalyst for hydrogen evolution.[33]

To test this theory, $Cr(CO)_6$ was heated in freshly distilled THF in the presence of mixed iron oxide powder. After filtration of the soluble $Cr(CO)_6$, the resulting red powder was analyzed by XPS. The high resolution Fe $2p_{3/2}$ signals in Figure 1.11 show the presence of Fe(III) and Fe(II) in both the starting material and the product; however, there is a distinct shift in the relative speciation. Analyzing the peak areas shows an increase in Fe(II) from 58% to 63% after heating with $Cr(CO)_6$. Additionally, the XPS Cr $2p_{3/2}$ signal (Figure 1.12) shows that no zero-valent chromium is in the sample. Assuming that no $Cr(CO)_6$ survived washing and being placed under vacuum, the peak is consistent with a mixture of Cr_2O_3 and CrO_3.[23] The lack of zero-valent chromium, coupled with the observed increase in Fe(II), shows that iron oxides do oxidize $Cr(CO)_6$. This observed oxidation is not attributed to accidental contamination with air or water because of the increase in Fe(II) content. The fact that the Fe(II) increase is small is expected, because most of the $Cr(CO)_6$ was recovered after the reaction. These results are significant, because TGA indicates that raw HiPco SWNTs contain 20-40 w/w% oxidized iron catalyst after combustion of the SWNTs in air (Figure 1.13).

XPS analysis of SWNT purification. The realization that the reaction of the residual catalyst appears to be masking any potential reactions with Cr and W carbonyl species led to an investigation into SWNT purification, beginning with an analysis of how well annealing removes bound and absorbed oxygen as well as how it effects the presence and oxidation state of the iron catalyst residue.

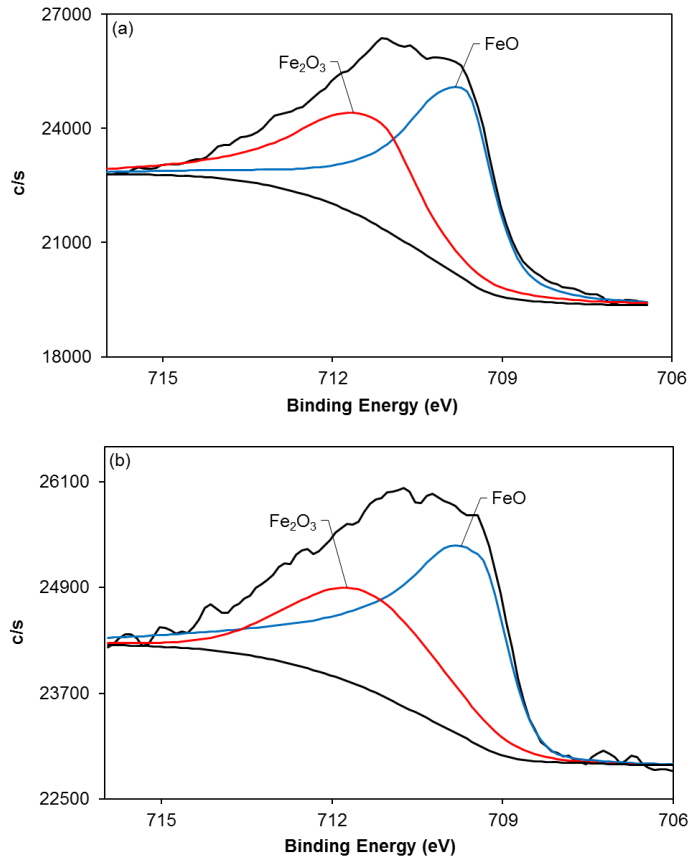

Figure 1.11. The Fe $2p_{3/2}$ XPS signals for (a) mixed iron oxide powder and (b) the product of the reaction between iron oxide powder and $Cr(CO)_6$.

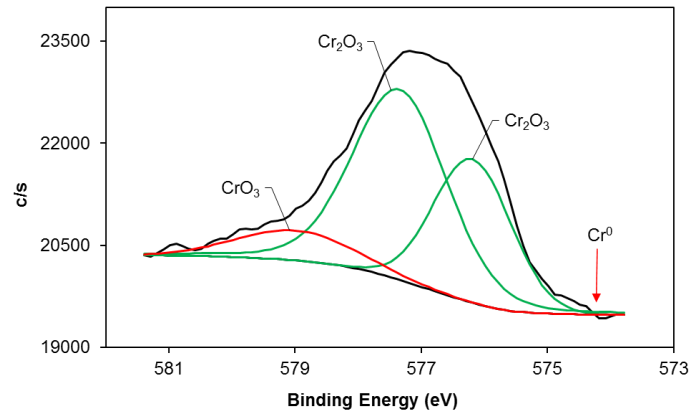

Figure 1.12. The Cr $2p_{3/2}$ XPS signal for the product of the reaction between Fe_2O_3 and $Cr(CO)_6$. Cr_2O_3 is fit with two curves to account for its complex multiplet splitting.[23]

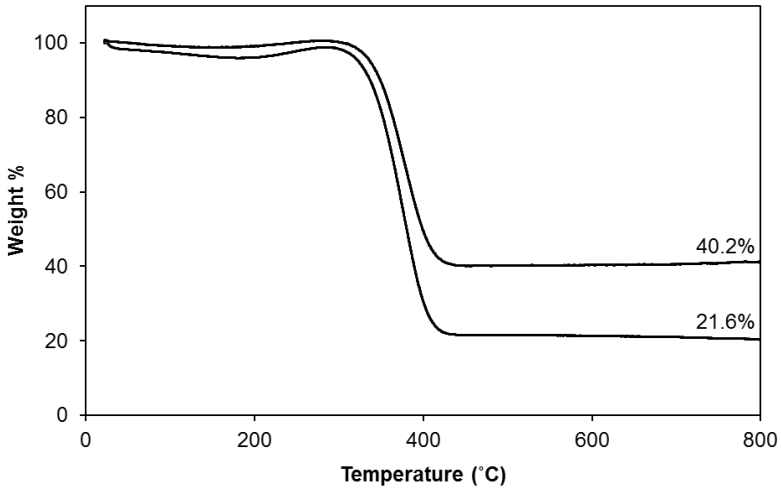

Figure 1.13. TGA of two samples from the same batch of raw HiPco SWNTs.

Analysis of the high resolution O 1s XPS peak of the as received tubes (Figure 1.14) shows the presence of iron oxides as indicated by the peak at 530.3 eV in addition to a range of oxygen moieties associated with the side wall of the SWNTs. Prior studies suggest these are due to the single and double bonds oxygen makes to carbon in carboxylic acid, ketone and alcohol groups.[34] Annealing the tubes in Ar or under vacuum reduces the oxygen on the SWNTs relative to the Fe oxide peak (Table 1.4). However, it is not clear whether or not the iron oxide peak is reducing simultaneously.

To determine this, the Fe $2p_{3/2}$ signals can be analyzed (Figure 1.15 and Table 1.4). It can be seen that the majority (ca. 65%) of the Fe present in the raw SWNT sample is due to zero-valent Fe, indicated by the peak at 706.6 eV (Figure 1.15a).[23,35] The remainder is a mixture of Fe(II) and Fe(III).[23,35] Annealing at 550 °C under Ar atmosphere has no obvious effect on the relative iron oxide concentration (Figure 1.15b and Table 1.4). By contrast, annealing under vacuum greatly increased the iron oxides, leaving only 9% zero-valent iron (Figure 1.15c and Table 1.4). Because the system was

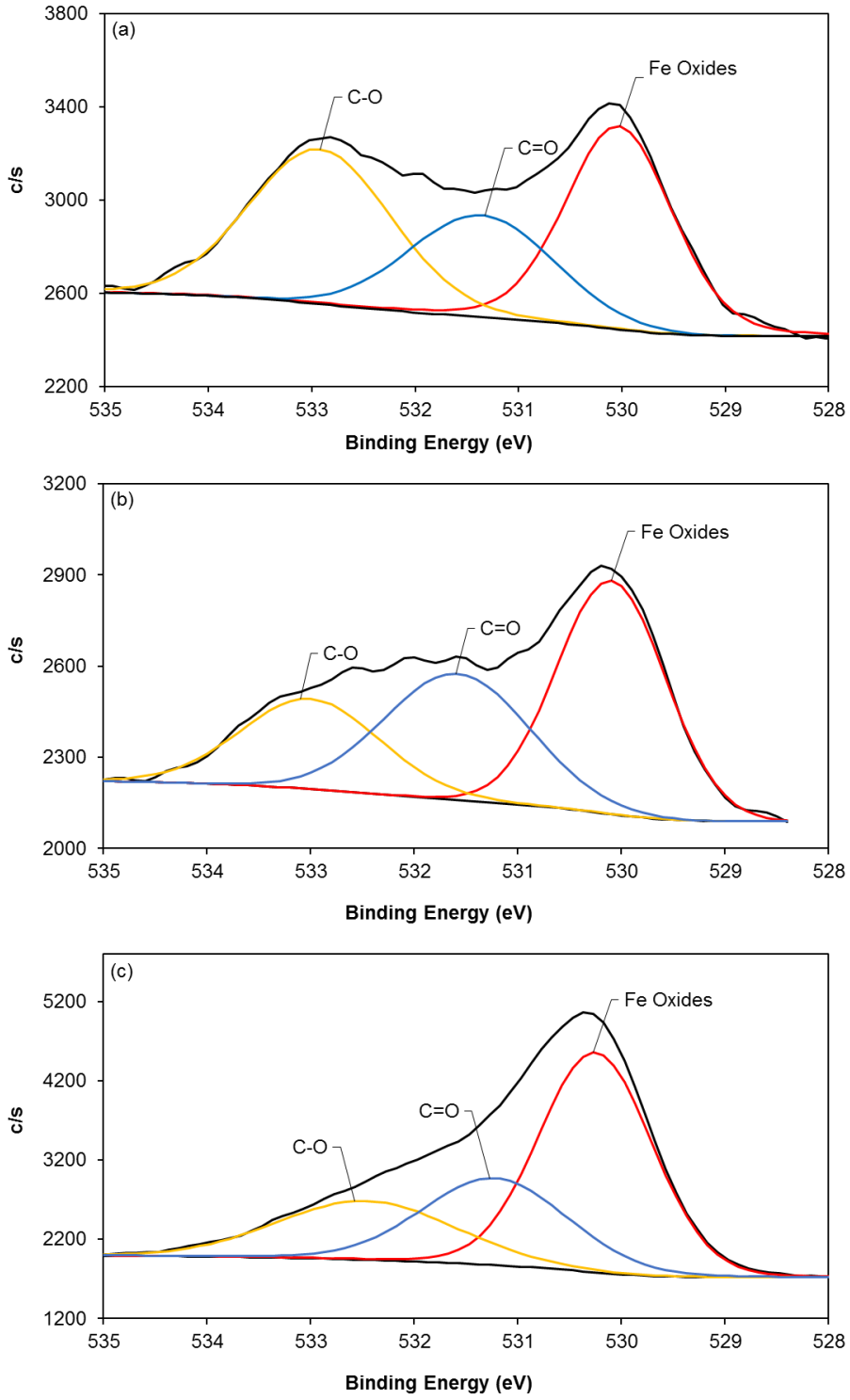

Figure 1.14. The XPS O 1s signals for (a) as received raw HiPco SWNTs and after annealing at 550 °C under (b) Ar atmosphere and (c) vacuum.

under vacuum, the oxidation of iron is assumed to be a result of the oxygen bound and absorbed on the tubes.

Table 1.4. O 1s and Fe 2p assignment and composition for raw SWNTs and after thermal annealing at 550 °C in Ar or vacuum.

Peak (eV)	Assignment	Raw-HiPco (%)	Ar annealed (%)	Vacuum annealed (%)	Microwave/HCl/vacuum annealed (%)
533.3[34]	C-O	37.47	22.68	21.74	45.40
531.5[34]	C=O	24.16	32.42	26.64	8.42
530.0	Fe oxides	38.37	44.90	51.62	46.18
706.6[23,35]	Fe(0)	64.86	64.08	9.17	51.59
709.5[35]	Fe(II)	11.76	13.63	43.11	28.92
711.0[35]	Fe(III)	23.38	22.29	47.73	19.49

Based upon the forgoing, annealing under vacuum is the most effective way to remove oxygen from the SWNTs. Although, it does not remove all of the oxygen, and it also increases the amount of iron oxides. Annealing under argon does not change the concentration of iron oxides, but it is not as effective at removing oxygen from the SWNTs. Both are problematic for Group 6 metal functionalization. Ineffective removal of oxygen from the SWNT surface along with the presence of iron oxides can result in oxidation of the Group 6 metals, especially given the low metal concentration being added. Thus, it is imperative that the iron catalyst be removed from the SWNTs prior to reaction with $Cr(CO)_6$, etc.

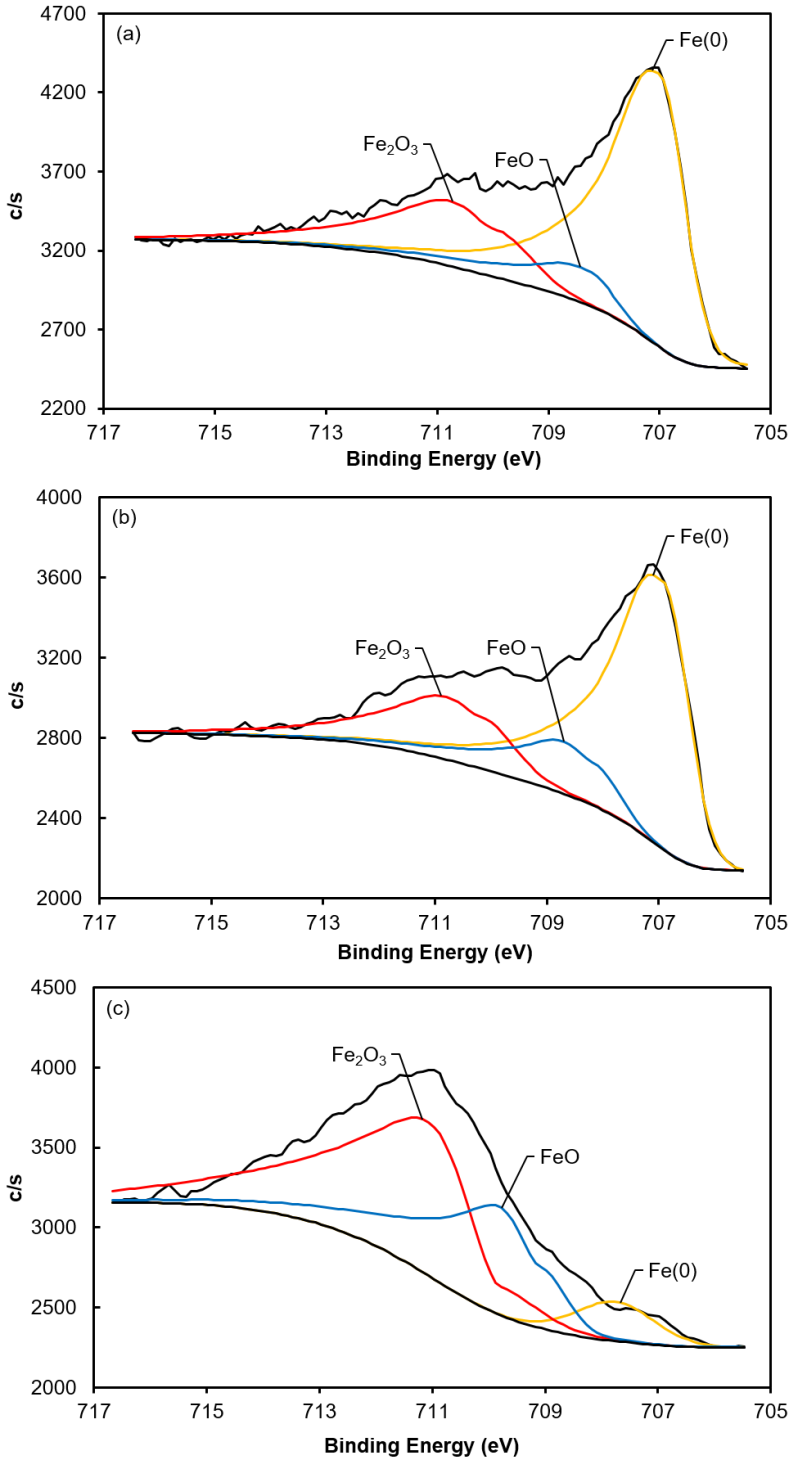

Figure 1.15. The Fe 2p XPS signals (a) as received HiPco SWNTs and after annealing at 550 °C under (b) Ar atmosphere and (b) vacuum. For simplicity the Fe(III) signal and its complex satellites are fit with a single peak.

In many instances, oxidative treatment of CNTs with HNO_3, piranha, H_2SO_4, and others have been shown to remove a substantial amount of the residual catalyst materials.[36] However, these treatments add oxygen functional groups[34], which are possibly detrimental to the chemistry of interest. Gomez, et al., have found that microwaving SWNTs in air causes carbon-encapsulated iron to break out of its carbon shell and be oxidized, facilitating its chemical removal with acid or chlorine.[37] This destruction of the encapsulation is critical for SWNT purification in general since the encapsulated catalyst residue is not removed by non-oxidative purification processes that don't also functionalize SWNT ends and sidewalls.[37]

In an attempt to remove the residual iron catalyst without altering the SWNTs, the tubes were microwaved using the procedure defined by Gomez, et al., then refluxed in concentrated hydrochloric acid to dissolve away the iron oxides. Finally, the SWNTs were annealed to remove oxygen functional groups, adsorbed oxygen, amorphous carbon, and any remaining hydrochloric acid. The XPS analysis of the resulting "cleaned" SWNTs shows a decrease in the amount of C=O groups on the SWNTs (Figure 1.16), as well as an overall decrease in oxygen species as indicated by the lower signal intensity. In addition, a decrease in zero-valent iron is observed (Figure 1.17 and Table 1.4) relative to untreated SWNTs (Table 1.4). But, because iron and iron oxides were not eliminated from the sample, it is suggestive that some of the residual catalyst remains encased in carbon. The TGA analysis of the sample (Figure 1.18) shows a residue of 21.8% (15.2% w/w Fe).

Reaction of $Cr(CO)_6$ with purified SWNTs. Despite the incomplete removal of catalyst materials from the cleaned SWNTs, the microwave/HCl/annealed SWNTs were

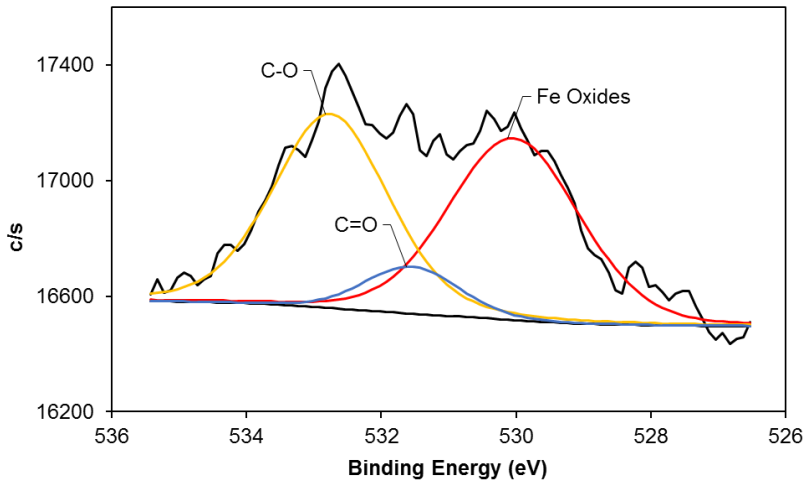

Figure 1.16. The XPS O 1s signal for microwaved, acid-treated and Ar annealed SWNTs.

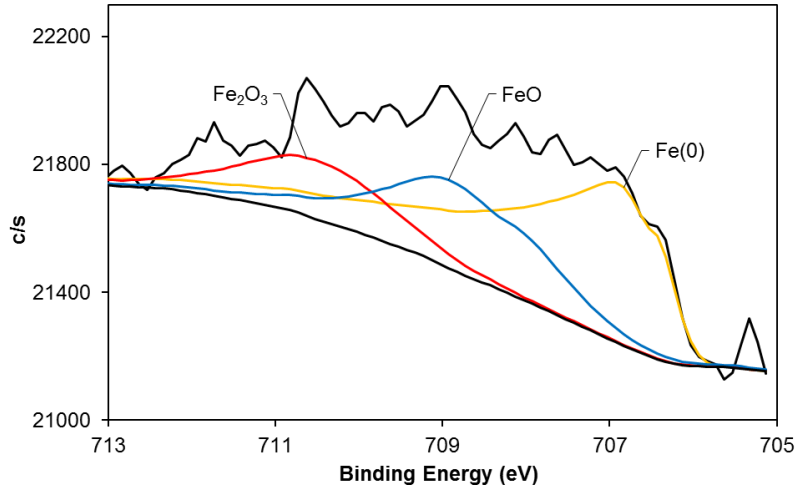

Figure 1.17. The XPS Fe $2p_{3/2}$ signal for microwaved, acid-treated and Ar annealed SWNTs.

reacted with $Cr(CO)_6$ and the products characterized using XPS. Figure 1.19 shows the Cr $2p_{3/2}$ peak, which indicates the presence of chromium oxides as a result of the curves high binding energies. Considering the incomplete removal of the iron catalyst from the SWNTs and the redox chemistry between iron oxides and zero-valent chromium shown

in the previous experiment, this is expected; however, what is important is that the chromium signal also has an 18.5% contribution from a zero-valent chromium peak at 574.0 eV. It is also important to note that this peak is in line with that expected for Cr metal.[23] However, as was previously discussed, the binding energy of (SWNT)$Cr(CO)_3$ overlaps with that of chromium(III) oxide. Thus, there is a possibility that (SWNT)$Cr(CO)_3$ is also present in this sample, but it is very difficult to confirm. Additionally, the iron signal in Figure 1.20 shows a shift in intensity toward lower binding energies compared to the iron signal for the cleaned SWNTs (Figure 1.17), indicating that the iron is being reduced (as a consequence of the oxidation of the Cr).

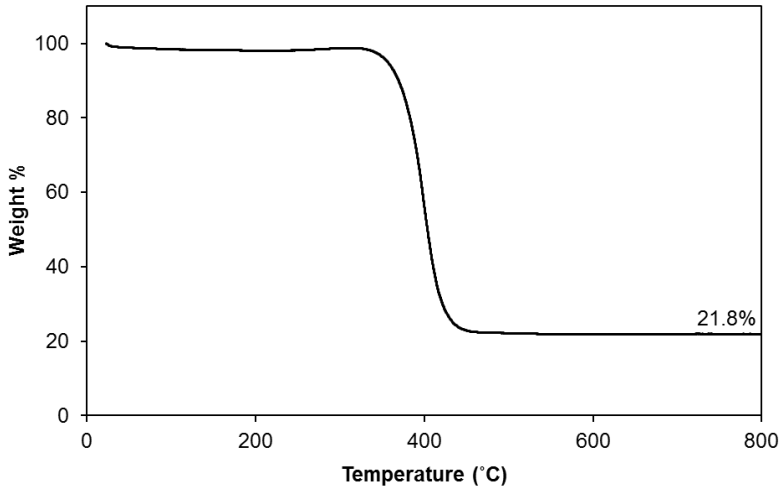

Figure 1.18. TGA of microwaved, acid-treated and Ar annealed SWNTs.

The presence of Cr(0) is confirmed in the current study after the removal of some of the iron catalyst, and the prior report[5] appears to be more consistent with the oxidation of the Cr by the catalyst residue (4.2 wt%) or from oxygen functional groups (since there is no mention of annealing). Although this study did not confirm "$Cr(CO)_n$" complexes of SWNTs, it does suggest that such complexes may indeed be prepared on SWNTs;

however, only upon removal of sufficient catalyst residue and oxygen bound to the SWNTs. This illustrates the importance of catalyst removal during SWNT purification.

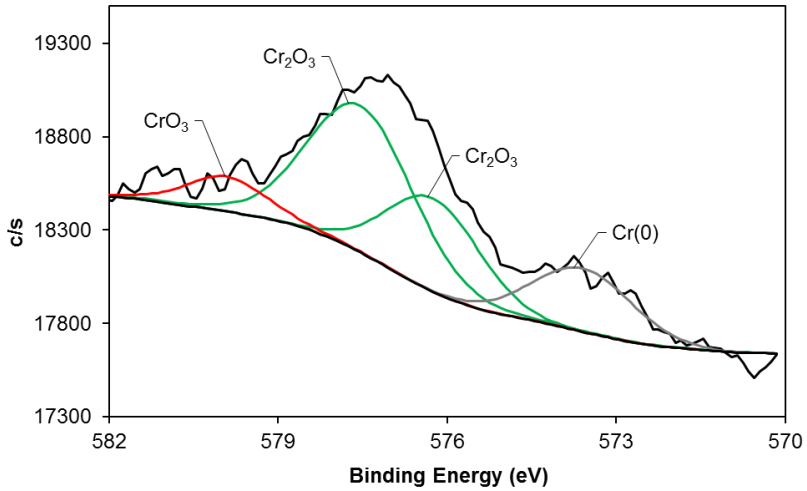

Figure 1.19. The XPS Cr $2p_{3/2}$ signal for chromium-functionalized cleaned SWNTs. Cr_2O_3 is fit with two curves to account for its complex multiplet splitting.[23]

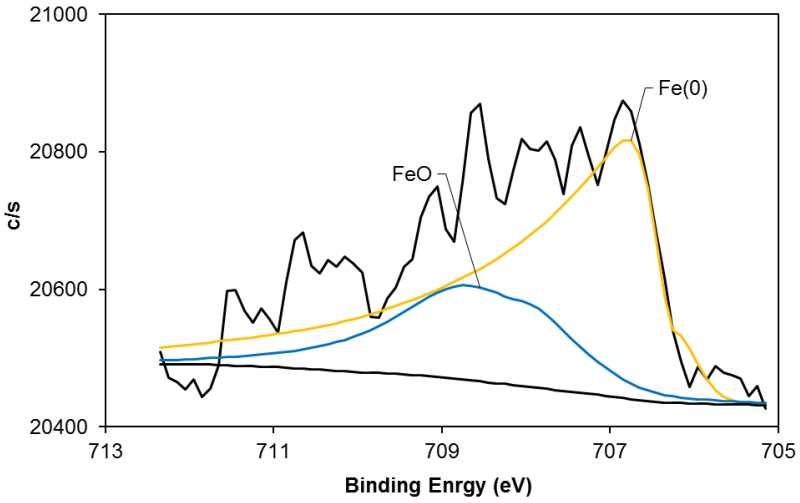

Figure 1.20. The XPS Fe $2p_{3/2}$ signal for the product from the reaction of $Cr(CO)_6$ with purified SWNTs.

Reaction of $W(CO)_6$ with highly purified SWNTs. To eliminate Group 6 metal oxidation from residual catalyst materials, SWNTs with ppb catalyst content (Lockheed Martin) were reacted with $W(CO)_6$. The choice of W as opposed to Cr was due to the lower propensity for oxidation of W(0) versus Cr(0). The purified SWNTs are spin-coated from aqueous solution onto silicon wafers, allowing for a suitable surface for reaction (Figure 1.21).

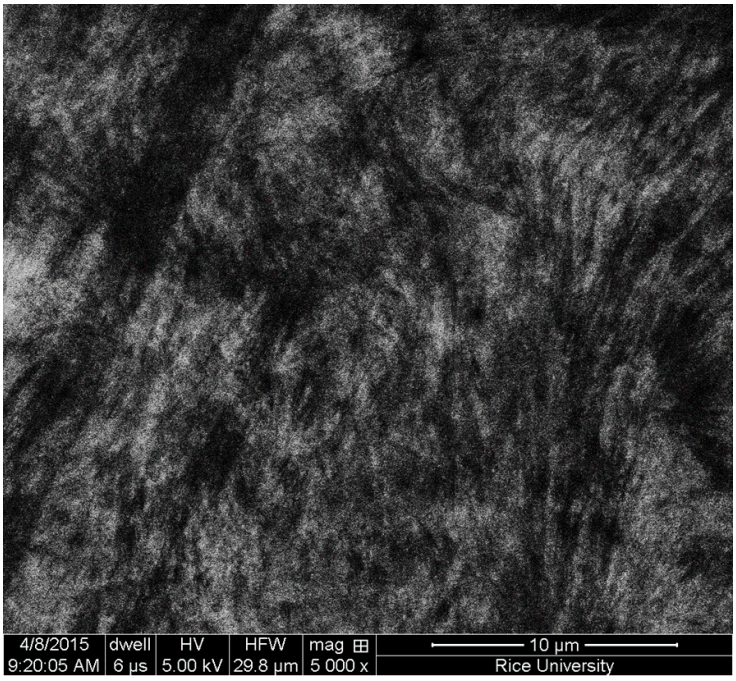

Figure 1.21. SEM of purified SWNTs spincoated on a silicon wafer.

After annealing the SWNT-coated wafers to remove oxygen functional groups, a concentrated $W(CO)_6$ solution was drop-coated on the wafer and allowed to dry. This was then loaded into a 600 ˚C argon-purged tube furnace to decompose the $W(CO)_6$ to W(0).[38] Upon removal from the furnace, the SWNT-coated wafer had a gray film covering most of its surface and a small, seemingly uncovered region at the edge. This

sample was analyzed with XPS depth profiling and with scanning electron microscopy (SEM) in both regions of the sample. The SEM image of the gray region of the sample in Figure 1.22a shows a densely-packed layer of W particles of around 330 nm in diameter. The SEM of the purple region of the sample shows a sparse layer of W particles of similar diameter, shown in Figure 1.22b. The goal of this experiment was to bridge the SWNT-SWNT junctions with Group 6 metals, not to put particles on the SWNT surface; however, the appearance of the latter was a consequence of the large excess of $W(CO)_6$ deposited on the wafers. Thus, it is the region without particles that is of interest since this contains a network of SWNTs which have been exposed to $W(CO)_6$.

Figure 1.23 shows the XPS depth profile for the purple region. This indicates an almost constant W intensity with depth, while C shows a small decrease as the nanotube layer is eroded down to the wafer. The observed decrease in C and the lack of change in the W intensity with depth indicates a higher concentration of W relative to C with depth. This increase in concentration with depth suggests that W preferentially infiltrates the SWNT layers, which may be evidence that W bridges the SWNT-SWNT junctions, since these junctions are not present at the surface of the sample.

The analysis of the high resolution W 4f XPS signals show the presence of 50% zero-valent tungsten at the surface of the sample, with the remaining tungsten being oxidized in the form of WO_3 (Figure 1.24a).[26] This is expected since these samples were exposed to the air. Once the samples are sputtered, the W(0) signals increase to 81% throughout the sample for up to 1 min of sputter time (Figure 1.24b). This is a major improvement over the analogous functionalization of HiPco SWNTs, emphasizing that

the presence of iron oxides and oxygen species on the tubes have a significant effect on the oxidation of Group 6 metals.

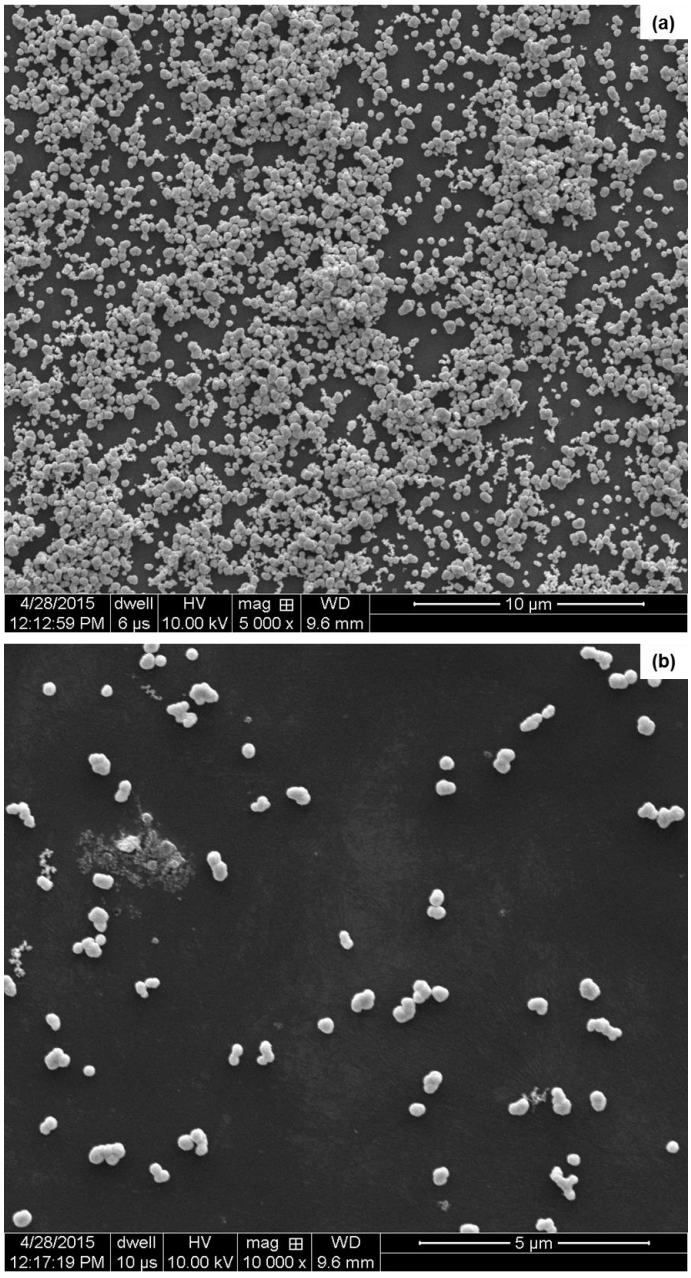

Figure 1.22. SEM images of the W-functionalized SWNT-coated wafer shows (a) a region that is densely packed with 330 nm W particles, which appears grey to the naked eye and (b) a more sparsely covered region with clear visibility of the SWNTs, which appear purple to the naked eye.

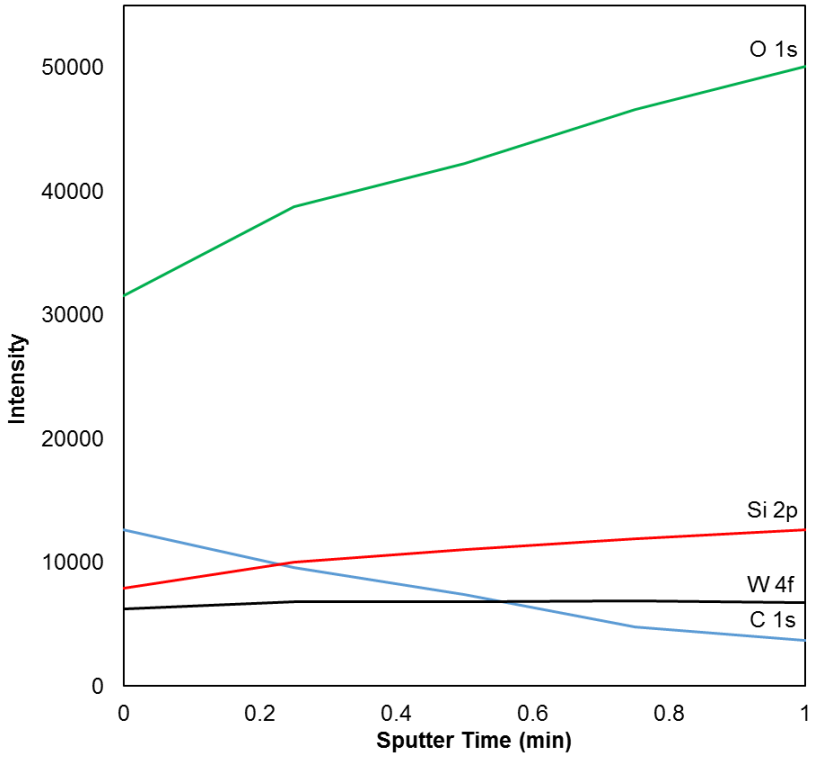

Figure 1.23. The XPS depth profile of a W-functionalized SWNT-coated wafer on the purple region of the sample. The sample was sputtered for 15 s between data collections.

Reaction of $Cr(CO)_6$ with graphene. Graphene was also functionalized with Cr as a crude model for SWNT behavior with Group 6 metals due to its relative ease of manipulation and high purity (99.9999%). By eliminating the residual catalyst from the reaction, the expectation was that fewer Group 6 metal oxides would be present in the graphene product relative to the SWNT products. A reaction between graphene and $Cr(CO)_6$ was conducted in THF using a similar procedure to the one outlined by the Haddon group and was characterized by XPS.[6] Because of the oxidation problems seen for functionalization reactions of SWNTs, the graphene was annealed under argon before use.

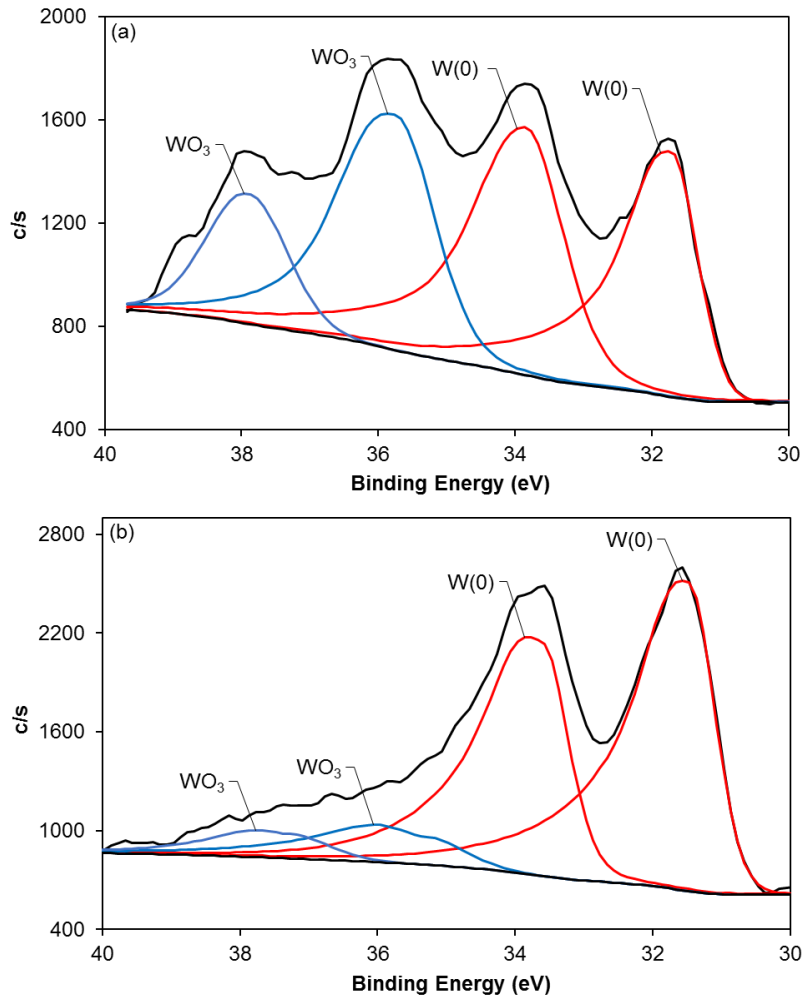

Figure 1.24. The high resolution XPS W 4f signals for the purple region of the W-functionalized SWNT-coated silica wafer. The sample was analyzed (a) before sputtering and (b) after 15 seconds of sputtering. Further sputtering and analysis resulted in similar tungsten signals for up to 1 min total sputter time.

The XPS chromium signals of the chromium-functionalized graphene (Figure 1.25) show the presence of zero-valent chromium before (a) and after sputtering (b). The concentration of zero-valent chromium decreases from 22.04% to 16.88% after sputtering the sample for one minute with a 3 kV, 2 by 2 mm argon ion beam. But, the overall concentration of chromium (relative to the carbon signal) increases from 4.2% before

sputtering to 9.2% after sputtering. Although XPS is not quantitative without a standard, this general increase suggests that chromium prefers to be sandwiched between the graphene sheets, in agreement with the depth profile of tungsten-functionalized SWNTs in Figure 1.23. And, indeed, the XPS also shows the presence of a new curve at 575.2 eV that is consistent with the formation of (graph)Cr(graph) (where graph = graphene), assuming this species has a similar chemical shift to $(C_6H_6)Cr(C_6H_6)$.[7] Comparing the curves before and after sputtering, an increase from 17.44% to 22.30% (graph)Cr(graph) is observed. This supports the claim that the concentration of Group 6 metals increases with depth as a result of (graph)Cr(graph) interconnects. Comparing the combined percentages of zero-valent chromium for functionalized graphene and functionalized SWNTs (Figure 1.19), a definite increase is seen for graphene- 39.5% of the chromium is unoxidized on graphene, whereas 18.5% is unoxidized on the cleaned SWNTs. Because the graphene starting material contains a parts per million (ppm) concentration of metal catalyst, an insignificant amount of the chromium is oxidized by residual catalyst. Even so, there is still a significant percentage of chromium(III) oxide on graphene (60.5%). As with the SWNT complexes, there is a possibility that a curve for (graph)$Cr(CO)_3$ is overlapping with the Cr_2O_3 signal, but determining what that concentration might be is difficult with the available characterization. Given the presence of Cr_2O_3, it is clear that adsorbed oxygen plays an important role in Group 6 metal oxidation on SWNTs and graphene. As was demonstrated by the study in the previous section, complete removal of oxygen from the surface of SWNTs is not accomplished by annealing (Figure 1.14). It seems likely that the same is true for graphene, especially considering the fact that

graphene and CNTs have been used for gas sensing and adsorption due in part to their extremely high surface areas.[30,39,40]

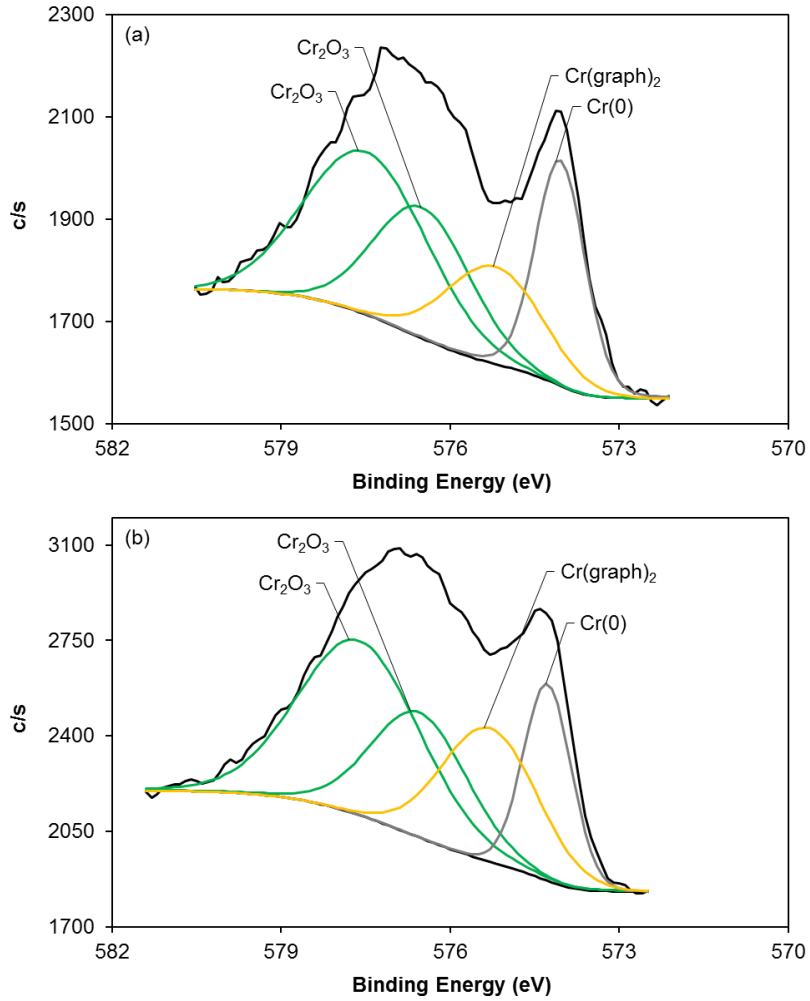

Figure 1.25. The XPS chromium $2p_{3/2}$ signals for chromium-functionalized annealed graphene (a) before sputtering and (b) after sputtering.

Conclusions

We have shown that the hexahapto functionalization of carbon materials with Group 6 metals is very challenging and not as straightforward as previously reported. The primarily product is the formation of Group 6 metal oxides as a consequence of the

residual SWNT growth catalyst and oxygen functional groups. Cleaning the SWNTs using a microwave and HCl treatment helped to decrease the residual iron catalyst, but, again, it did not eliminate it. However, it enabled the first observation of a Cr(0) species on a SWNT, albeit contaminated with oxide. Reactions with ultrapure SWNTs (ppb Fe) and graphene do facilitate the formation of M(0) species intercalated into the SWNTs. And, in the case of graphene, we were able to directly observed the formation of (graph)Cr(graph) in XPS. However, we were unable to observe any $–Cr(CO)_3$ complexes as a result of their overlapping binding energies with chromium(III) oxides. We can conclude that in order to make the functionalization of carbon materials with Group 6 metals successful, it is imperative that the carbon materials be extremely pure and free of both catalyst and absorbed oxygen.

Experimental

All reagents were used as received unless otherwise noted. All solvents were distilled (unless they were obtained from the solvent purification system) and degassed with bubbling argon. Glassware was placed in a base bath before use, then washed with soap and water and dried in an oven overnight. XPS was measured on a PHI Quantera XPS Scanning Microprobe using Al Kα X-rays. The spectra were shifted using a carbon standard of 284.5 eV. Solution IR spectra were obtained on a PerkinElmer Spectrum Two FT-IR. SEM images were acquired on an FEI Quanta 400 ESEM FEG.

$(CH_3CN)_3M(CO)_3$. The synthesis of $(CH_3CN)_3M(CO)_3$ was adapted from the literature.[17] $M(CO)_3$ (1 equivalent, where M is Cr or W) was added to a Schlenk flask in the glove box. Acetonitrile (100 equivalents) was transferred by cannula to the reaction vessel directly from the distillation apparatus. The $M(CO)_3$ solution was refluxed and the

reaction progress was monitored by solution-phase IR spectroscopy. After 4 days, the IR showed primarily $(CH_3CN)_3M(CO)_3$ with some $(CH_3CN)_2M(CO)_4$ according to peak assignments found in the literature.[18] The solution was allowed to cool to room temperature, and the solvent was pumped off to leave a yellow solid. Hexane was added to the solids by cannula. The mixture was agitated, and then filtered using inert atmosphere techniques to produce yellow solids on the filter and a yellow solution. The solution was discarded and the solids were collected for further use.

$(C_7H_8)M(CO)_3$. The synthesis of $(C_7H_8)M(CO)_3$ was adapted from the literature.[17] Cycloheptatriene (4.3 mL, 12.6 equivalents) and hexane obtained from a solvent purification system (50 mL) were added via syringe to a mixture of $(CH_3CN)_3M(CO)_3$ and $(CH_3CN)_2M(CO)_4$ (M = Cr or W, exact composition unknown, about 1 equivalent) in a Schlenk flask. The solution was heated and allowed to reflux for 4 days. The solution was allowed to cool. The mixture was filtered using inert atmosphere techniques to produce a red solution and yellow solids on the filter. A solution IR was run on the crude product, indicating that the desired product had been synthesized according to literature peak assignments.[20,21] The product was dried under vacuum, leaving behind a red crystals in the reaction vessel and yellow solids in the solvent trap.

Reaction of SWNTs with $M(CO)_6$, $(C_7H_8)M(CO)_3$, or $(C_6H_6)Cr(CO)_3$. This synthesis was adapted from the literature.[6] SWNTs (0.04 g, 5 equivalents of carbon atoms) were placed in a Schlenk flask equipped with a stir bar and were heated at 100 ˚C under vacuum overnight. $M(CO)_6$, $(C_7H_8)M(CO)_3$, or $(C_6H_6)Cr(CO)_3$ (1 equivalent, M = W or Cr) and 20 mL THF were added to the cooled flask in a glove box. The mixture was

kept under argon and sonicated in a bath sonicator to disperse the SWNTs. The vessel was then put under an argon flow and refluxed for 4 days. The product was allowed to cool and was then centrifuged at 4,400 rpm for 30 minutes. The supernatant was decanted off, leaving a black solid. THF was added and the vial was sonicated in a bath sonicator to redisperse the product. The dispersion was centrifuged again. This process was repeated 3 times. The black solid was then dried and stored under vacuum. The product was characterized by XPS and TEM.

Microwave and HCl acid-treatment of SWNTs. 0.2 g of dry HiPco SWNTs were placed in an 860 watt domestic microwave oven with an open 500 mL beaker filled with water (for dissipating some of the heat). The SWNTs were heated for 1 min and then allowed to cool. This process was repeated until the SWNTs had been heated for a total of 10 min. They were then placed in 150 mL of concentrated HCl, stirred and refluxed overnight. The black mixture was allowed to cool to room temperature and then diluted to about 300 mL with water. The SWNTs were removed by filtering the mixture through a 0.22 μm PVDF filter paper. They were rinsed with DI water until the pH of the rinse was no longer acidic, and then placed under vacuum to dry overnight. Once dry, the tubes were put into a quartz boat and loaded into a tube furnace. As the inside of the furnace was preheating to 550 ˚C, the SWNTs were degassed under a 600 mL/min flow of Ar in the tube, just outside of the furnace itself. After 30 minutes, the SWNTs were slid into the furnace (using a magnet on the outside of the tube) and heated for 2 hours. The SWNTs were allowed to cool under Ar and then quickly transferred to a glove box for storage. The cleaned SWNTs were characterized by XPS. Yield: 69.6%

Reaction of HCl cleaned or annealed SWNTs with $Cr(CO)_6$. SWNTs (0.2 g, 5 equivalents of carbon atoms) were placed in a quartz boat with a magnet attached to it by way of a long steel wire. Using another magnet on the outside of the quartz tube of the furnace, the boat was slid into the end of the tube. The tube was degassed with argon for 30 minutes as the furnace was preheated to 550 ˚C. The SWNTs were then slid into the furnace using the outer magnet and heated under a 600 mL/min flow of argon for 1 hour. The SWNTs were slid back to the end of the tube and allowed to cool under argon. The SWNTs were then quickly transferred to an argon-purged Schlenk flask. The flask was immediately taken to the Schlenk line and put under vacuum for 10 minutes to remove any air that followed the SWNTs into the reaction vessel. The vessel was transferred to the glove box where $Cr(CO)_6$ (0.6 g, 1 equivalent) was added. It was then placed under argon on the Schlenk line and THF (~20 mL) was added via cannula to the reaction vessel. This mixture was refluxed for 4 days. After cooling to room temperature, the black mixture was transferred to an argon-purged centrifuge vial and was centrifuged at 4,400 rpm for 30 minutes. The supernatant was decanted off, leaving a black solid. THF was added and the vial was sonicated in a bath sonicator to redisperse the product. The dispersion was centrifuged again. This process was repeated 3 times. The black solid was then dried and stored under vacuum. The product was characterized by XPS.

Reaction of annealed Lockheed Martin SWNT-coated wafer with $M(CO)_6$. An aqueous solution of SWNTs was spin-coated on a silicon wafer by Lockheed Martin. The wafer was diced up into about 1 inch by 0.5 inch rectangles. One SWNT-coated wafer piece was placed in a quartz boat with a magnet attached to it by way of a long steel wire. Using another magnet on the outside of the quartz tube of the furnace, the boat

was slide into the end of the tube. The tube was degassed with argon for 30 minutes as the furnace was preheated to 600 ˚C. The boat was then slid into the furnace using the outer magnet and heated under a 600 mL/min flow of argon for 1 hour. The SWNT-coated wafer was slid back to the end of the tube and allowed to cool under argon. The wafer was removed from the tube furnace and placed under flowing argon. A $M(CO)_6$ solution (~14 mg in 1 mL of THF, M = Cr or W) was drop-coated on the wafer's surface and allowed to dry. The wafer was quickly transferred in air to the tube furnace, where it was allowed to sit under 600 mL/min flowing argon for about 1 minute (longer purge times resulted in significant loss of $M(CO)_6$ due to sublimation). Then, the argon flow rate was decreased to 100 mL/min and the wafer was slid into the 600 ˚C furnace. After 20 minutes, the wafer was slid back out of the furnace and allowed to cool at the end of the quartz tube. The sample was stored under vacuum until it was ready to be analyzed by XPS and SEM.

Exfoliated graphite. This procedure was adapted from the literature.[6] High purity graphite powder (-200 mesh, 99.9999% metals basis, 0.07 g) and o-dichlorobenzene were added to a plastic centrifuge vial. The suspension was sonicated with an ultrasonic probe at 35% amplitude for 1 h. The dispersion was centrifuged at 4,000 rpm for 30 minutes. The resulting black supernatant was decanted off and filtered through a PTFE filter paper. The black solid was rinsed with THF to remove residual o-dichlorobenzene and dried under vacuum. The resulting black powder was annealed at 600 ˚C under a 600 mL/min flow of argon for 2 hours and was immediately transferred to the glove box after cooling.

Reaction of graphene with $Cr(CO)_6$. This synthesis was adapted from the literature.[6] Graphene (50 mg, 5 equivalents of carbon atoms) and $Cr(CO)_6$ (0.18 g, 1

equivalent) were added to a Schlenk flask in a glove box. THF (20 mL) was added to the reaction vessel via cannula and it was then heated to 110 ˚C on a Schlenk line. The mixture was allowed to reflux under argon for 5 days. The suspension was cooled and was then centrifuged at 4,400 rpm for 30 minutes. The yellow supernatant was decanted off, leaving a black solid. THF was added and the vial was sonicated in a bath sonicator to redisperse the product. The dispersion was centrifuged again. This process was repeated 3 times. The black solid was then dried and stored under vacuum. The product was characterized by XPS.

References

1. R. Pandey, B. K. Rao, P. Jena and M. A. Blanco, *J. Am. Chem. Soc.*, 2001, **123**, 3799–3808.
2. S. Niyogi, E. Bekyarova, J. Hong, S. Khizroev, C. Berger, W. de Heer and R. C. Haddon, *J. Phys. Chem. Lett.*, 2011, **2**, 2487–2498.
3. S. Dag, O. Gulseren and S. Ciraci, *Appl. Phys. Lett.*, 2003, **83**, 3180–3182.
4. F. Wang, M. E. Itkis, E. Bekyarova, S. Sarkar, X. Tian and R. C. Haddon, *J. Phys. Org. Chem.*, 2012, **25**, 607–610.
5. I. Kalinina, E. Bekyarova, S. Sarkar, F. Wang, M. E. Itkis, X. Tian, S. Niyogi, N. Jha and R. C. Haddon, *Macromol. Chem. Phys.*, 2012, **213**, 1001–1019.
6. S. Sarkar, S. Niyogi, E. Bekyarova and R. C. Haddon, *Chem. Sci.*, 2011, **2**, 1326–1333.
7. S. Pignataro, A. Foffani and G. Distefano, *Chem. Phys. Lett.*, 1973, **20**, 350–355.
8. G. . Allen and P. . Tucker, *Inorganica Chimica Acta*, 1976, **16**, 41–45.
9. G. Davidson and E. M. Riley, *Spectrochim. Acta*, 1971, **27A**, 1649–1658.

10. S. Myllyoja and T. A. Pakkanen, *J. Mol. Catal. A: Chem.*, 1998, **136**, 153–160.

11. J. C. Cook and E. M. McCash, *Surf. Sci.*, 1996, **364**, L605–L611.

12. K. L. Strong, D. P. Anderson, K. Lafdi and J. N. Kuhn, *Carbon*, 2003, **41**, 1477–1488.

13. I. W. Chiang, B. E. Brinson, A. Y. Huang, P. A. Willis, M. J. Bronikowski, J. L. Margrave, R. E. Smalley and R. H. Hauge, *J. Phys. Chem. B*, 2001, **105**, 8297–8301.

14. L. Cai, J. L. Bahr, Y. Yao and J. M. Tour, *Chem. Mater.*, 2002, **14**, 4235–4241.

15. J. Kayat, V. Gajbhiye, R. K. Tekade and N. K. Jain, *Nanomed Nanotech Biol Med*, 2011, **7**, 40–49.

16. V. E. Kagan, Y. Y. Tyurina, V. A. Tyurin, N. V. Konduru, A. I. Potapovich, A. N. Osipov, E. R. Kisin, D. Schwegler-Berry, R. Mercer, V. Castranova and A. A. Shvedova, *Toxicology Letters*, 2006, **165**, 88–100.

17. G. J. Kubas, *Inorg. Chem.*, 1983, **22**, 692–694.

18. B. L. Ross, J. G. Grasselli, W. M. Ritchey and H. D. Kaesz, *Inorg. Chem.*, 1963, **2**, 1023–1030.

19. G. R. Dobson, M. F. A. E. Sayed, I. W. Stolz and R. K. Sheline, *Inorg. Chem.*, 1962, **1**, 526–530.

20. R. B. King and A. Fronzaglia, *Inorg. Chem.*, 1966, **5**, 1837–1846.

21. E. W. Abel, M. A. Bennett, R. Burton and G. Wilkinson, *J. Chem. Soc.*, 1958, 4559–4563.

22. U. J. Kim, X. M. Liu, C. A. Furtado, G. Chen, R. Saito, J. Jiang, M. S. Dresselhaus and P. C. Eklund, *Phys. Rev. Lett.*, 2005, **95**, 157402.

23. M. C. Biesinger, B. P. Payne, A. P. Grosvenor, L. W. M. Lau, A. R. Gerson and R. S. C. Smart, *Appl. Surf. Sci.*, 2011, **257**, 2717–2730.

24. D. D. Sarma and C. N. R. Rao, *J. Electron. Spectrosc. Relat. Phenom.*, 1980, **20**, 25–45.

25. E. W. Plummer, W. R. Salaneck and J. S. Miller, *Phys. Rev. B*, 1978, **18**, 1673–1701.

26. G. E. McGuire, G. K. Schweitzer and T. A. Carlson, *Inorg. Chem.*, 1973, **12**, 2450–2453.

27. R. P. A. Sneeden, *Organochromium compounds*, Academic Press, New York, 1975.

28. C. D. Hoff, *J. Organomet. Chem.*, 1983, **246**, c53–c56.

29. J. C. Slater, *Phys. Rev.*, 1930, **36**, 57–64.

30. P. Giannozzi, R. Car and G. Scoles, *J. Chem. Phys.*, 2003, **118**, 1003–1006.

31. F. A. Cotton and G. Wilkinson, *Advanced inorganic chemistry*, Wiley, New York, 5th ed., 1988.

32. S. S. Zumdahl and S. A. Zumdahl, *Chemistry*, Houghton Mifflin Company, Princeton, N.J., 5th ed., 2006.

33. A. J. Bard, R. Parsons, J. Jordan and International Union of Pure and Applied Chemistry, Eds., *Standard potentials in aqueous solution*, M. Dekker, New York, 1st ed., 1985.

34. A. Jung, R. Graupner, L. Ley and A. Hirsch, *phys. stat. sol. (b)*, 2006, **243**, 3217–3220.

35. N. S. McIntyre and D. G. Zetaruk, *Anal. Chem.*, 1977, **49**, 1521–1529.

36. E. R. Edwards, E. F. Antunes, E. C. Botelho, M. R. Baldan and E. J. Corat, *Appl. Surf. Sci.*, 2011, **258**, 641–648.

37. V. Gomez, S. Irusta, O. B. Lawal, W. Adams, R. H. Hauge, C. W. Dunnill and A. R. Barron, *RSC Adv.*, 2016, **6**, 11895–11902.

38. P. K. Sahoo, S. S. Kalyan Kamal, M. Premkumar, T. Jagadeesh Kumar, B. Sreedhar, A. K. Singh, S. K. Srivastava and K. Chandra Sekhar, *Int. J. Refract. Met. H.*, 2009, **27**, 784–791.

39. F. Schedin, A. K. Geim, S. V. Morozov, E. W. Hill, P. Blake, M. I. Katsnelson and K. S. Novoselov, *Nature Materials*, 2007, **6**, 652–655.

40. G. Stan, M. J. Bojan, S. Curtarolo, S. M. Gatica and M. W. Cole, *Phys. Rev. B*, 2000, **62**, 2173–2180.

Chapter 2

Metal Coordination to C_{60} Fullerene

Introduction

Shortly after the discovery of fullerenes in 1985[1], many groups began efforts to understand the carbon clusters' chemistry. In 1991, the first covalent organometallic bond was reported between C_{60} fullerene and zero-valent platinum, forming a stable dihapto, (η^2) complex.[2] In the same report, the authors attempted to functionalize C_{60} with η^5-$C_5(CH_3)_5Ru^+$, which commonly forms η^6 bonds with electron rich 6-membered arenes.[2] Contrary to their expectations, they synthesized $\{[\eta^5$-$C_5(CH_3)_5Ru(CH_3CN)_2]_x(C_{60})\}^{x+}(O_3SCF_3)_x^-$, where ruthenium forms an η^2 interaction to C_{60}.[2] Multiple other η^2 metal complexes were synthesized subsequently.[3,4] This phenomenon was found to be the result of C_{60}'s unique curved geometry, which causes a high degree of strain and π orbitals that are pyramidalized by 11.64˚ (see Figure 2.1).[5–7] For η^2 complexation to occur, π orbitals must be pyramidalized by incorporating more s character, thereby shifting the geometry to be more tetrahedral in order to have efficient orbital-overlap with the metal.[7] Because the orbitals in C_{60} already have some degree of pyramidalization, their reactivity toward η^2 bonding is larger relative to planar arenes.[7] Further, it has been found that the strain and hybridization of C_{60} is conserved over the entire molecule, so the increase in pyramidalization required to accommodate η^2 bonding results in a global decrease in pyramidalization and strain of the other 58 carbon atoms.[7] Therefore, the formation of an η^2 bond to C_{60} decreases the overall strain by 8 to 17 kcal/mol.[7]

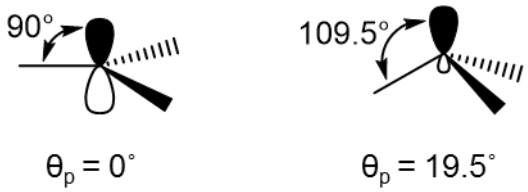

Figure 2.1. The piramidalization angle, $\theta_p = \theta_{\pi\sigma} - 90^\circ$, for a trigonal planar geometry, left, and a tetrahedral geometry, right.

Despite reports of many stable η^2 metal complexes to C_{60}, the literature does not report any η^2 copper complexes to fullerenes.[8] This is surprising, because copper(I) is known to make stable complexes to a variety of different olefins.[9–12] Many of these copper(I) olefin complexes are known for their instability, but, when bound to bidentate nitrogen ligands such as *bis*(2-pyridyl)amine, they are resistant to losing their olefins in solution and in inert atmospheres.[9–14] These complexes are also stabilized by weakly coordinating counter-ions such as BF_4^- and ClO_4^-, which do not compete with the olefin for complexation to copper.[15] Despite the plethora of literature on stable copper(I) olefin complexes and of metal-functionalized fullerenes, there are only a few reports on copper(I) complexes made to fullerenes. In all cases, the fullerene is functionalized at the carbons adjacent to a central five membered ring which reduces the pyramidalization of the ring (Figure 2.2).[16,17] Copper(I) is then complexed via η^5 coordination.[16,17] In Halim's article, gold(I), silver(I) and copper (I) were complexed to pentaaryl-functionalized fullerenes, forming an η^1/ η^3 bond with gold, an η^2/ η^3 bond with silver, and an η^5 bond with copper, despite the metals being in the same group.[16] In the case of copper, the energy level of the p orbitals is similar to that of the π orbitals of the five membered ring, allowing for the formation of a stable η^5 complex.[16] Gold and silver, on the other hand,

have higher energy p orbitals that do not interact as strongly with the π orbitals of the fullerene.[16] Further, the formation η^1 bonds, as is the preference for gold complexes, relieves angle strain in the five membered ring.[16] Thus, the balance between relief of strain and the stability of multihapto bonding determines the degree of haptacity of the metal to the fullerene.[16] Without functional groups, fullerenes are too pyramidalized to accommodate η^5 complexation, and η^2 complexation lends to the greatest relief of strain.[6,7] Thus, given the stability of η^2 copper(I) olefin complexes and of η^2 transition metal-fullerene complexes, we suggest that η^2 complexes of copper(I) to unfunctionalized C_{60} should also form.

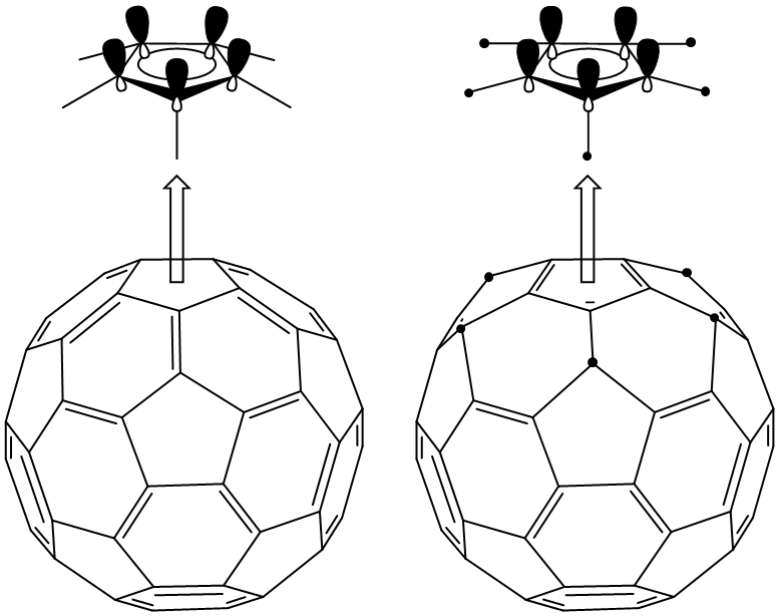

Figure 2.2. The pyramidalization of the π orbitals of C_{60} and C_{60} functionalized at the 5 carbons indicated by black dots.

Fullerenes also have never been reported to form η^6 bonds with metals.[18] A variety of η^5 metal complexes have been synthesized with C_{60}, but this requires

functionalization of the fullerene, as was discussed previously for copper(I) complexes (Figure 2.2).[3,6] The reason for this is explained through pyramidalization, because the π orbitals of the unaltered fullerene are splayed out away from the incoming metal center, orbital overlap with the metal's d orbitals is not efficient for η^5 coordination. The increase in pyramidalization (sp^3 hybridization) of the adjacent carbons allows for a decrease in pyramidalization of the five membered ring between them.[6] This flattening of the five membered ring makes possible the formation of η^5 complexes.[6] Similar functionalization about the six membered rings of C_{60} to accommodate η^6 coordination has not been reported. But, "fullerenocene" and similar η^6 transition metal complexes have been studied from a theoretical standpoint. Unfortunately, these studies are of little help in determining if η^6 complexes can actually be synthesized. In terms of aromaticity, Salcedo calculated that $Cr(C_{60})_2$ and $(C_{60})Cr(C_6H_6)$ have large aromatic stabilization energies relative to $Cr(C_6H_6)_2$, suggesting that these complexes should have similar stability to $Cr(C_6H_6)_2$.[18] On the other hand, Haddon has reported that η^6 bonds to C_{60} do not form as a result of pyramidalization- the π bonds are splayed out from the center of the benzenoid ring by 9.8˚ relative to the normal of the plane of the ring.[7] This translates to poor orbital-overlap with transition metals that favor η^6 bonding, which cannot be corrected with repyramidalization of the orbitals toward the center of the ring since this would lead to increased strain.[7] To gain a better understanding of η^6 coordination to C_{60} fullerenes from an experimentalist's standpoint, functionalization of C_{60} with chromium was attempted.

Results and Discussion

Copper coordination to C_{60} fullerene. Functionalization of C_{60} with copper(I) was first attempted using a previously reported method (Figure 2.3).[9,12] Here, the olefin is

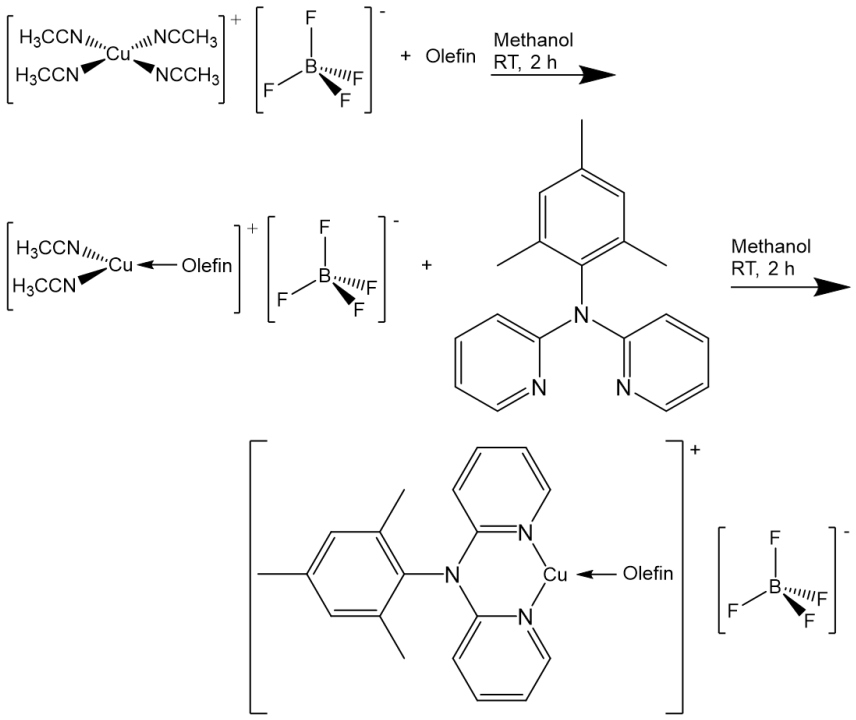

Figure 2.3. Reaction scheme showing the synthesis of [(olefin)Cu(mes-dpa)]BF_4.[9,12]

reacted with [Cu(MeCN)$_4$]BF_4, then the desired *bis*(2-pyridyl)amine derivative is added. For the amine derivative, mesitylene-2,2'-dipyridylamine (mes-dpa) was used because of its stabilizing effect on copper(I) olefin complexes as a result of its ability to fold the dpa portion to reduce steric effects.[12] Initial reactions were run in butanol, as was reported previously;[12] however, C_{60} has very poor solubility in butanol, so subsequent reactions were run in a mixture of butanol and 1,1,1-trichloroethane. The crude product was analyzed by ^{1}H NMR in $CDCl_3$, which shows only very weak signals from mes-dpa in Figure 2.4. Compared to uncomplexed mes-dpa in Figure 2.5, the aromatic signals are shifted downfield (except for "d", which is shifted upfield) and are very broad. Additionally, Figure 2.4 shows two slightly more intense signals, which are shifted further upfield from the "g" and "e" signals. Because all of these signals are very broad, it

is clear that the quadrupolar copper is bound to mes-dpa. The presence of the additional downfield-shifted aromatic signals suggests that mes-dpa exists in two different environments, and is thus showing two sets of signals.

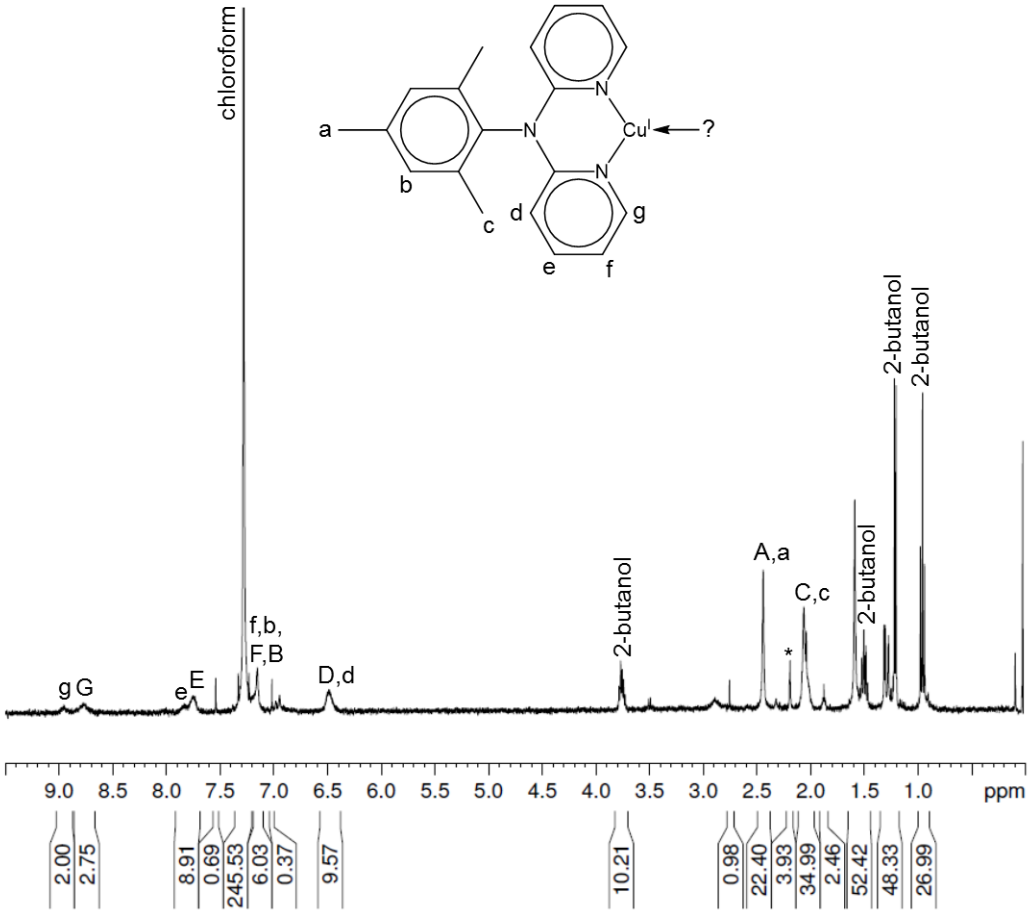

Figure 2.4. ^{1}H NMR of the crude product from the reaction of C_{60} with $[Cu(CH_3CN)_4]BF_4$ and mes-dpa. *An impurity from the mes-dpa starting material.

In an effort to concentrate the desired ionic product, the crude powder was dispersed in butanol and filtered. The ^{1}H NMR in $CDCl_3$ of the resulting solution in Figure 2.6, again, shows two sets of broadened mes-dpa signals. The signals labeled g and e are shifted downfield compared to the g and e uncomplexed mes-dpa signals in

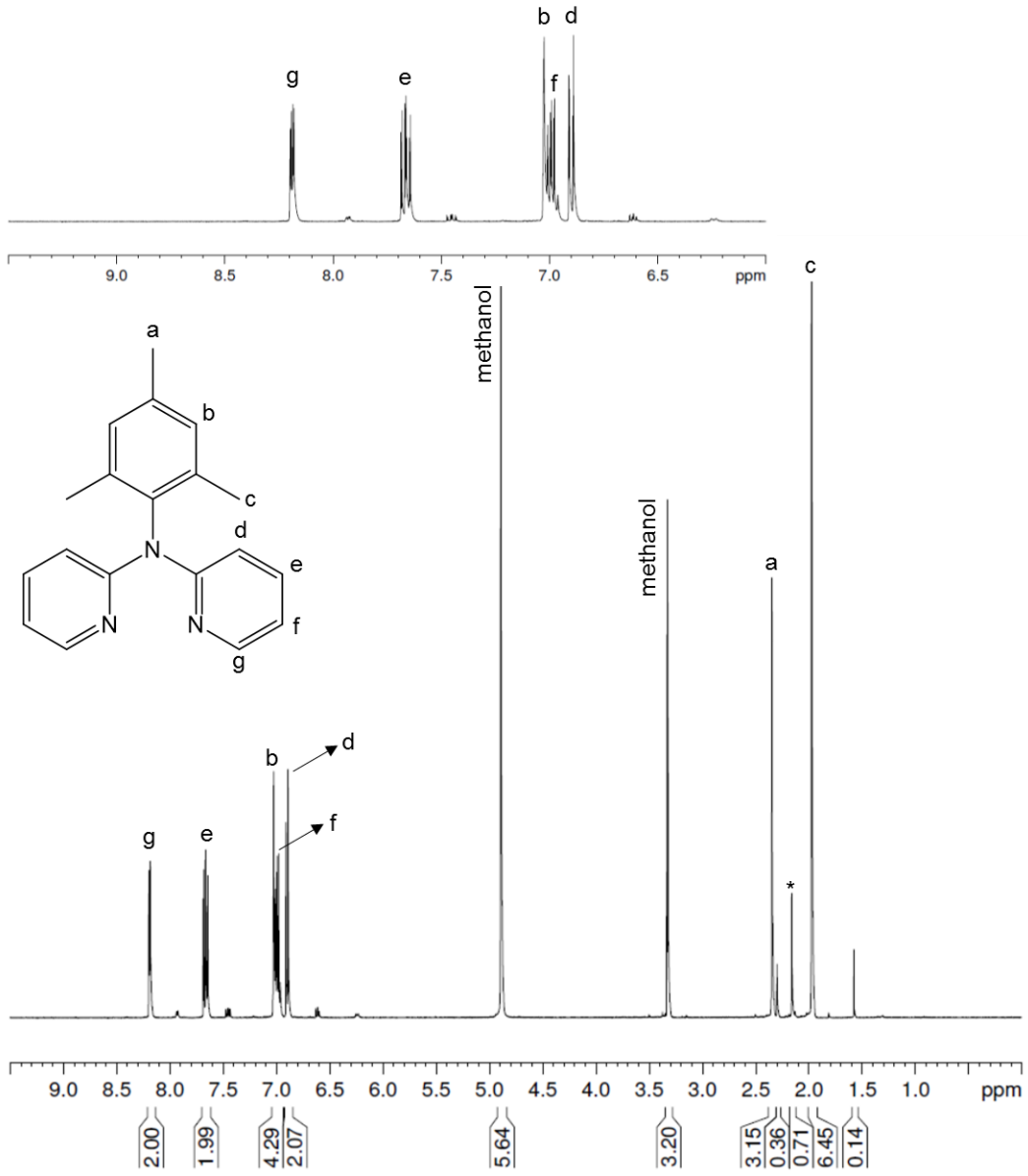

Figure 2.5. ^{1}H NMR of mes-dpa. *An unknown impurity that translates to the products of reactions involving mes-dpa.

Figure 2.5. They also have similar chemical shifts to the g and e signals in Figure 2.4. However, the signals labeled g' and e' are shifted upfield from those seen in Figure 2.4, but shifted downfield from the uncomplexed mes-dpa in Figure 2.5. Additionally, there is a strong signal at 2.16 ppm, which appears in the same location as an impurity found in

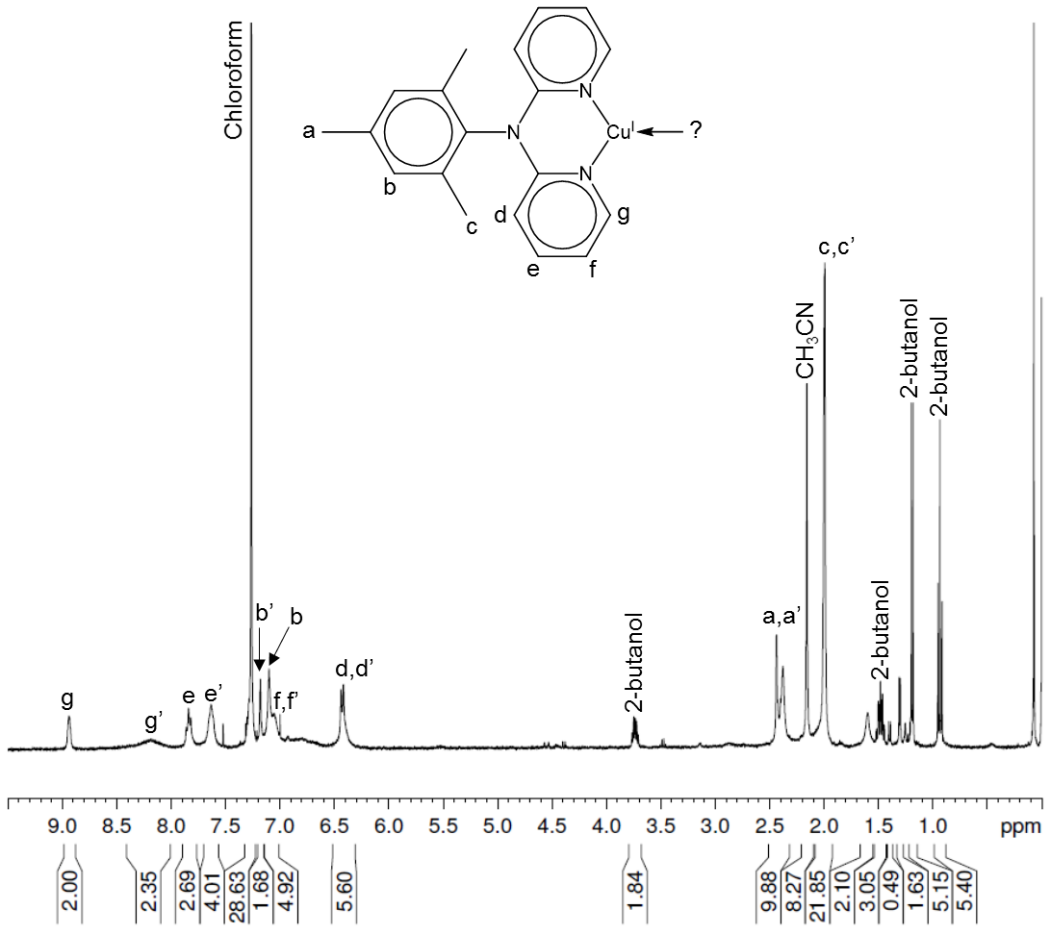

Figure 2.6. ^{1}H NMR of the product extracted with 2-butanol from the reaction of C_{60} with $[Cu(CH_3CN)_4]BF_4$ and mes-dpa.

the mes-dpa (* in Figure 2.5). But, this signal is 13 times the integrated value of the impurity in the starting material. Analysis of the $[Cu(MeCN)_4]BF_4$ starting material shows a singlet at the same chemical shift, indicating that this signal is a result of unreacted $[Cu(MeCN)_4]BF_4$ or possibly the formation of a $(CH_3CN)_2Cu$(mes-dpa) complex (assuming these acetonitrile protons have similar chemical shifts). To determine if C_{60} was bound to copper, the product was also analyzed by ^{13}CNMR (Figure 2.7). However, the spectra does not show enough aromatic carbons above the noise to identify

the products, and further efforts to isolate the desired product by crystallization or extraction were unsuccessful due to decomposition.

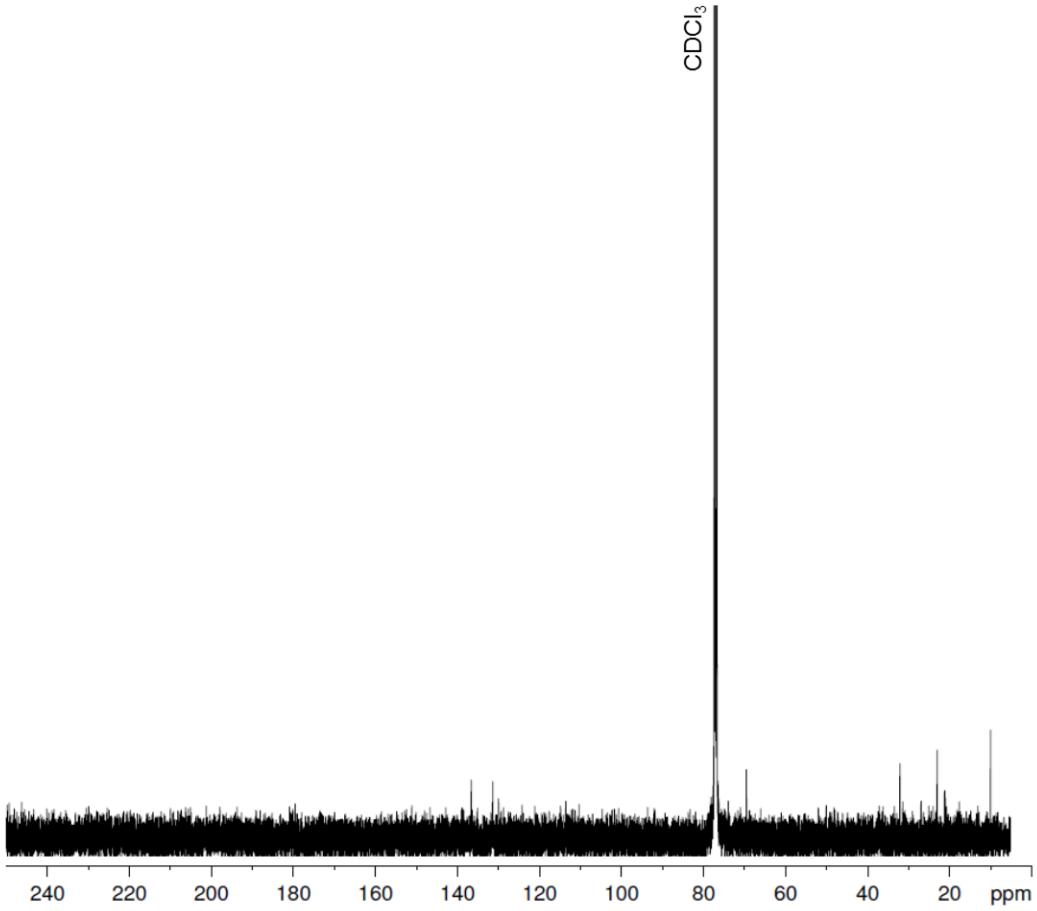

Figure 2.7. ^{13}C NMR of the product extracted with 2-butanol from the reaction of C_{60} with $[Cu(CH_3CN)_4]BF_4$ and mes-dpa.

The ^{1}H NMR spectra discussed up to this point suggests that there are three mes-dpa-Cu complexes present in the crude product. We propose a mixture of $(C_{60})Cu(mes\text{-}dpa)$, $Cu(mes\text{-}dpa)_2$, and $(CH_3CN)_2Cu(mes\text{-}dpa)$. To help in determining that species present in the spectra above, $[Cu(mes\text{-}dpa)_2]BF_4$ was synthesized using a similar method to the one reported for complexing two substituted diquinolylamine groups to copper.[19]

The ^{1}H NMR of this complex in Figure 2.8 shows broadened mes-dpa signals, which are shifted from their original chemicals shifts in Figure 2.5. The signals labeled e, b, and f are all shifted downfield, while the signals labeled g and d are shifted upfield. As was discussed previously, the protons of $[Cu(MeCN)_4]BF_4$ appear at 2.17 ppm and overlap with the contaminant found in mes-dpa. Because the normalized integration of this signal is lower than the signal in the mes-dpa spectrum (0.64 and 0.71, respectively), this signal probably has no contribution from the acetonitrile ligands. Because there are no other significant signals, the presence of $[(MeCN)_2Cu(mes\text{-}dpa)]BF_4$ is also ruled out. Further, the formation of a single bond from one pyridine group of the mes-dpa to the copper center is not enthalpically or entropically favored.[20] This sort complexation is also ruled out by the ^{1}H NMR, because there is only a single set of signals for the mes-dpa ligand, confirming bidentate coordination of the mes-dpa ligand to the copper center. Because copper(I) complexes form tetrahedral or distorted tetrahedral structures in the case of large bidentate ligands,[21,22] we assign the product of this reaction as $[Cu(mes\text{-}dpa)_2]BF_4$. Comparing the chemical shifts of this molecule to those seen for the crude product in Figure 2.4 indicates that $[Cu(mes\text{-}dpa)_2]BF_4$ is not present in the analyzed sample. However, the product extracted with 2-butanol (Figure 2.6) shows one set of mes-dpa signals (indicated by primed letters) that match up very well with those seen for the $[Cu(mes\text{-}dpa)_2]BF_4$ complex, and are thus assigned to this structure. The other two sets of mes-dpa signals cannot be unambiguously assigned to structures, but do imply the formation of $[(MeCN)_2Cu(mes\text{-}dpa)]BF_4$ and possibly the formation of $[(C_{60})Cu(mes\text{-}dpa)]\ BF_4$.

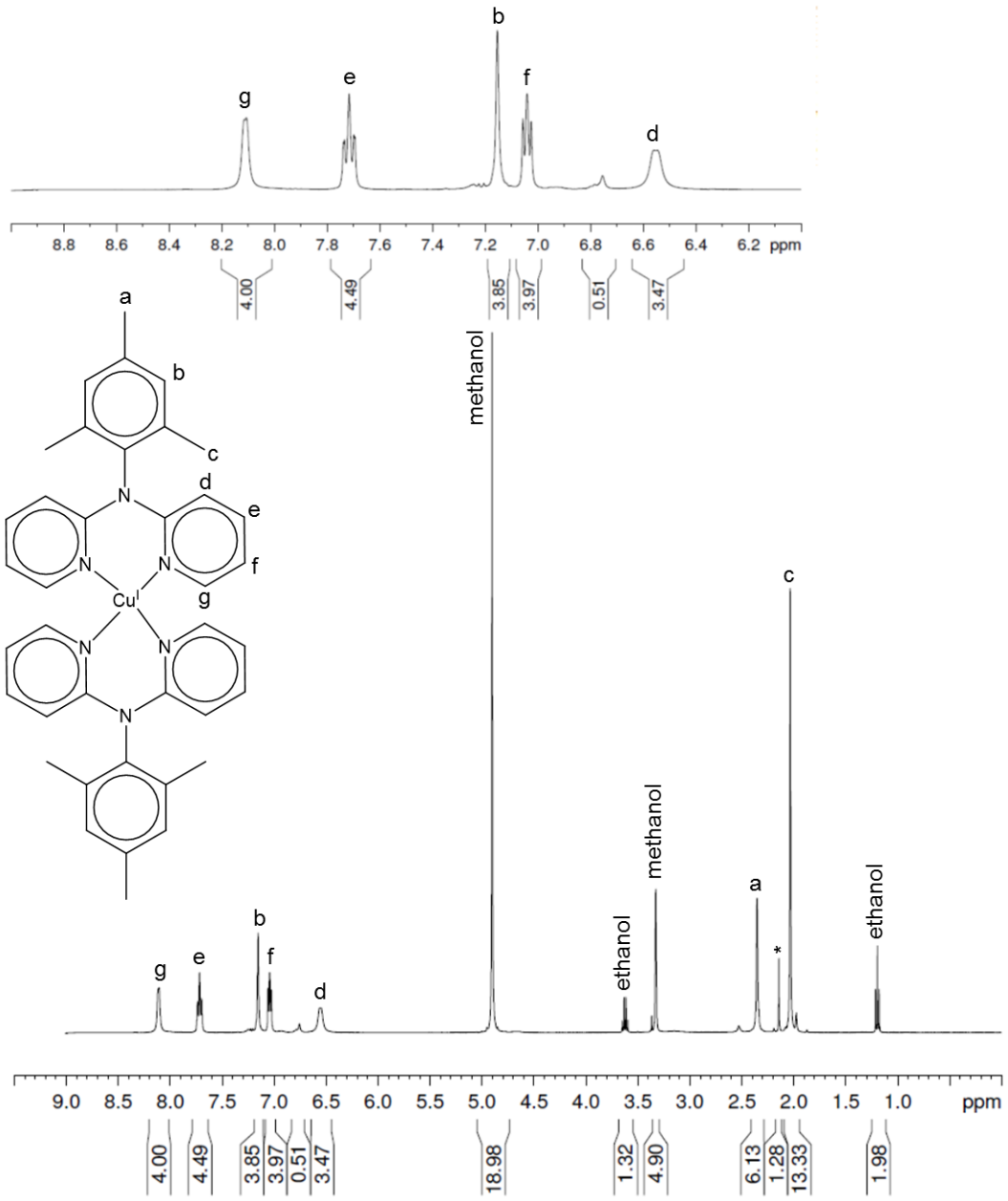

Figure 2.8. ^{1}H NMR of [Cu(mes-dpa)$_2$]BF$_4$. *An impurity from the mes-dpa starting material.

As a result of the complications in functionalizing C_{60} using Allen's method, another method, which was adapted from the literature,[10] was also attempted. Here, fine copper powder, $Cu(ClO_4)_2$ and the olefin are reacted in an alcohol solution to produce a

copper(I)-olefin complex (Figure 2.9). The mes-dpa ligand is then added. Rather than using C_{60} as the starting olefin for this reaction, ethylene was used. There are multiple benefits to synthesizing the $[(C_2H_4)Cu(mes\text{-}dpa)]ClO_4$ complex before trying to incorporate C_{60}- the ethylene synthesis is defined in the literature, bubbling ethylene gas into an air sensitive solution is easier than adding a powder, there is no unreacted olefin to separate from the product, and crystallization of the product is simple. But, most importantly, ethylene is a gas, so any exchange that happens with a non-gaseous olefin like C_{60} will not be reversible.

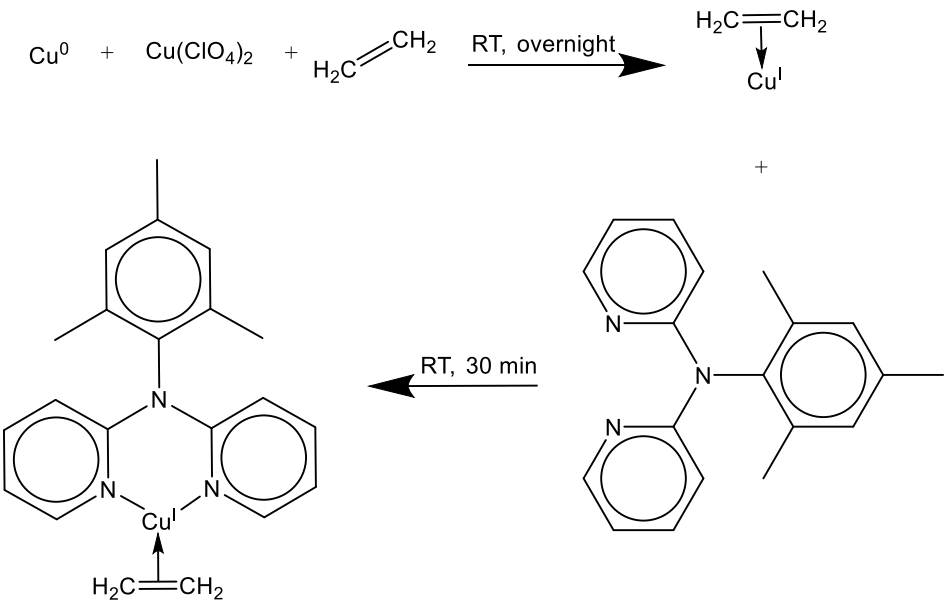

Figure 2.9. Reaction scheme for the synthesis of $[(C_2H_4)Cu(mes\text{-}dpa)]ClO_4$.[10] The perchlorate ion is the counter ion for both copper(I) complexes, and is left out for clarity.

The $[(C_2H_4)Cu(mes\text{-}dpa)]ClO_4$ complex was successfully synthesized and characterized using ^1H NMR. Comparing the ^1H NMR spectra of the copper complex in Figure 2.10 to the mes-dpa starting material in Figure 2.5, the broadening of the mes-dpa

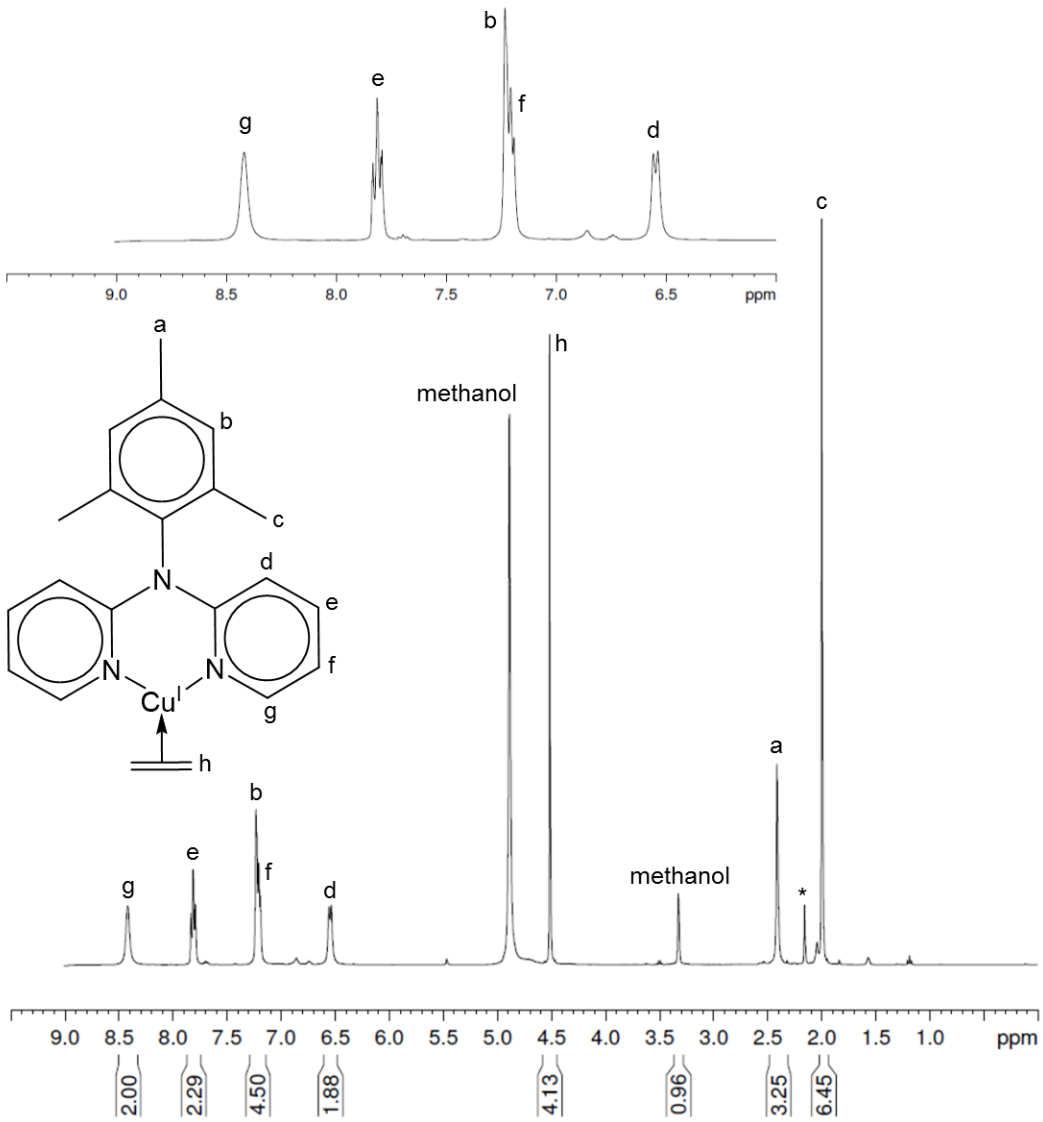

Figure 2.10. ^{1}H NMR of $[(C_2H_4)Cu(mes\text{-}dpa)]ClO_4$. *An impurity from the mes-dpa starting material.

signals as a result of complexation to copper is obvious. The broadening is most severe for the protons that are closest to the copper center on carbon 6 of the pyridine rings (labeled g in Figure 2.10), as is expected. Mes-dpa's complexation to copper is also made

obvious by the downfield shift of the aromatic protons (except for d, which shifts upfield). We assign the singlet at 4.52 ppm to complexed ethylene, in agreement with similar complexes reported in the literature.[9] This signal has an upfield shift of about 0.9 ppm relative to that of free ethylene.[9] Further, this signal's normalized integration (relative to the g protons on the complexed mes-dpa) is 4.13, indicating that there is approximately a one to one ratio of ethylene to mes-dpa. This implies that all of the copper complexes in the sample contain ethylene.

The $[(C_2H_4)Cu(\text{mes-dpa})]ClO_4$ complex was then combined with C_{60} in an ethanol and 1,1,1-trichloroethane solvent mixture (Figure 2.11), which fully dissolved the copper complex and partially dissolved C_{60}. The mixture was bubbled with argon to remove any dissolved ethylene, preventing it from recombining with the copper complex and encouraging it to bind with C_{60}. After 24 hours, the solution was diluted with ethanol to precipitate unreacted C_{60} and filtered. The resulting solution was bubbled with argon to reduce the volume and placed in the freezer in an attempt to crystallize the product. However, no crystals would form and any attempt to dry the product under vacuum or flowing argon resulted in visual decomposition of the product. The color changed from yellowish brown to greenish brown and the ^{1}H NMR of the filtered green product did not show any evidence of mes-dpa.

To eliminate the need for drying or crystallization, a similar reaction was conducted in a mixture of deuterated methanol and chloroform (1:5). After 24 hours, more deuterated methanol was added to encourage the desired product to dissolve and the mixture was filtered. The resulting brown solution was analyzed by ^{1}H NMR, shown in Figure 2.12. As with the other observed copper complexes, the mes-dpa signals are

shifted and broadened. The most notable of these is the shift of the F protons downfield of the B protons, which has not been observed in any of the other spectra. However, overlapping signals in the previous spectra may have made these signals difficult to locate. Comparing the other aromatic signals in this spectra to those seen in the first experiment, we note that the G, E and D signals of Figure 2.12 have the same chemical shifts as those labeled the same in Figure 2.4. Therefore, we assign these signals to the same structure. Observing that the 2.16 ppm signal in Figure 2.12 is very low in intensity, we assume that there are no acetonitrile ligands, and that this signal is the result of the mes-dpa contaminant. Therefore, this structure cannot be assigned to $[(MeCN)_2Cu(mes\text{-}dpa)]ClO_4$. It also cannot be assigned to $[Cu(mes\text{-}dpa)_2]ClO_4$, because the chemical shifts of this spectra do not align with those in Figure 2.8. By process of elimination, we

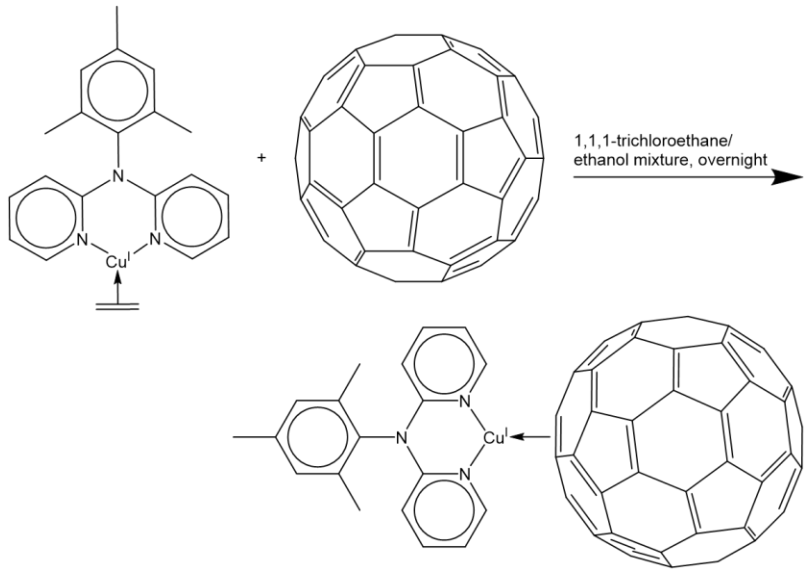

Figure 2.11. Reaction scheme showing the synthesis of $[(C_{60})Cu(mes\text{-}dpa)]ClO_4$. The perchlorate ion is the counter ion for both copper(I) complexes, and is left out for clarity.

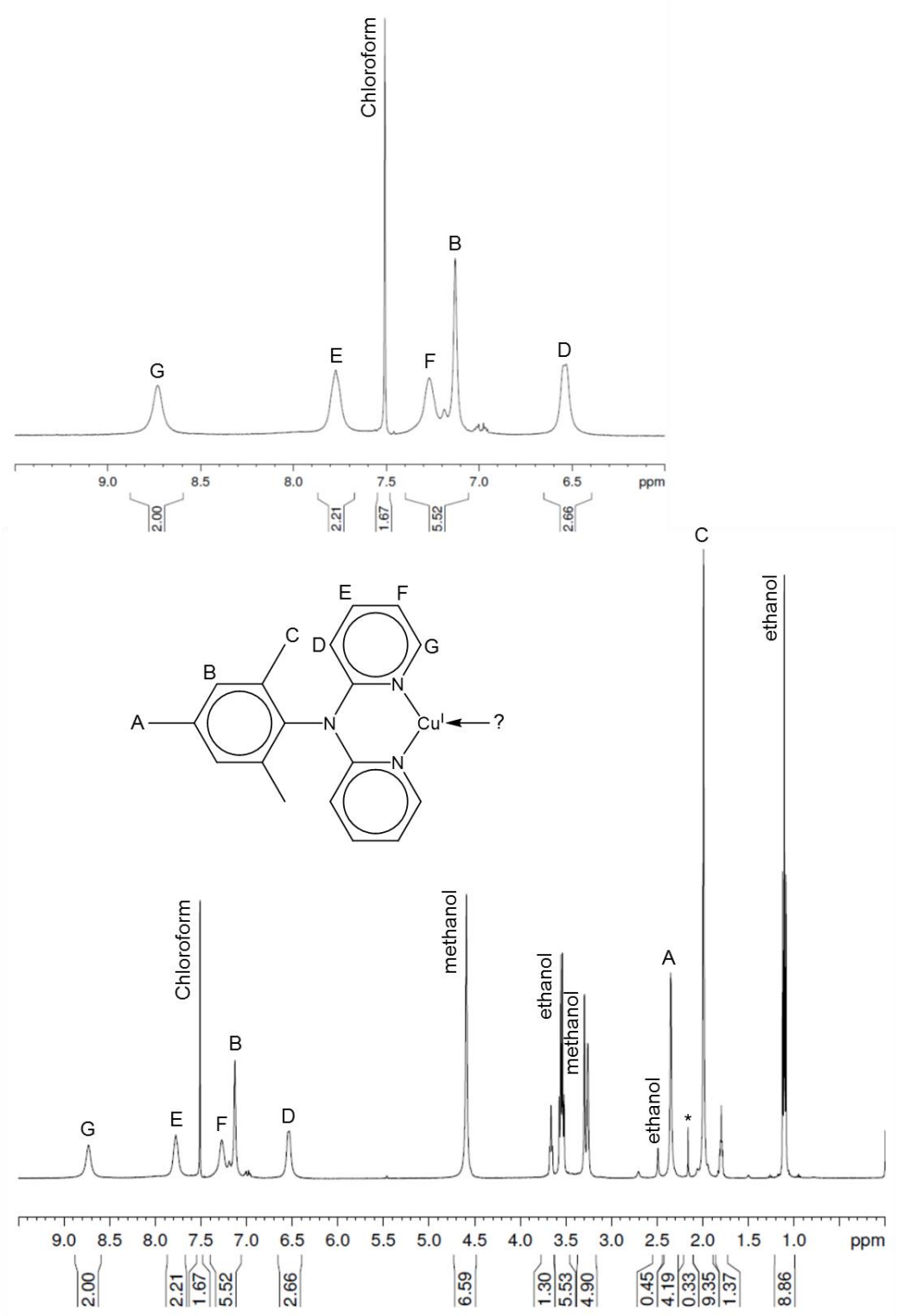

Figure 2.12. ^{1}H NMR of the product of the reaction between $[(C_2H_4)Cu(mes\text{-}dpa)]ClO_4$ and C_{60} in deuterated methanol and chloroform. *An impurity from mes-dpa.

speculate that the ^{1}H NMR can be assigned to $[(C_{60})Cu(mes\text{-}dpa)]ClO_4$. To confirm this assignment, ^{13}C NMR and X-ray crystallography are necessary. Unfortunately, this molecule proved to be very unstable. The ^{13}C NMR was collected immediately after the ^{1}H NMR, but did not show any signals besides those for the solvents. Upon removal from the magnet, the sample was found to have crashed out of solution. Further attempts to collect this data from the same batch resulted in similar problems. Additionally, the ^{1}H NMR spectra of subsequent experiments on the same batch showed different chemical shifts for the mes-dpa ligand, suggesting decomposition of the product. The instability of this complex also made characterization using X-ray crystallography impossible.

Group 6 metal coordination to C_{60} fullerene. Group 6 metal functionalization of C_{60} fullerene was attempted with chromium (Figure 2.13), since it is the most reactive of the Group 6 metals. The first challenge associated with this chemistry was finding an appropriate solvent. C_{60} has the best solubility in benzene-derived molecules, especially napthalenes, 1,2-dichlorobenzene and tetralin.[23] However, these molecules are all reactive toward the $Cr(CO)_6$ starting material and cannot be used. C_{60} has reasonably good solubility in carbon disulfide at 7.9 mg/mL and is also a good solvent for ^{1}H NMR analysis since it has no protons, but it has a boiling point of only 46.3 ˚C.[23] Haloalkanes and some large, cyclic alkanes provide minimal solubility.[23] Because these are compatible with the chemistry and have reasonably high boiling points, these sorts of solvents were tested. Cycloctane, diglyme (0.7 mg C_{60}/mL)[24], and 1,1,1-trichloroethane (0.15 mg C_{60}/mL)[25] were used for reactions between C_{60} and $Cr(CO)_6$ or the more reactive $(CH_3CN)_3Cr(CO)_3$. For reference, the solubility of C_{60} in cyclopentane, cyclohexane and decalins is 0.002, 0.036 and 4.6 mg/mL, respectively.[23] Because the

solubility increases with increasing number of carbons in these examples, it was assumed that solubility in cycloctane would be better than in cyclopentane and cyclohexane.

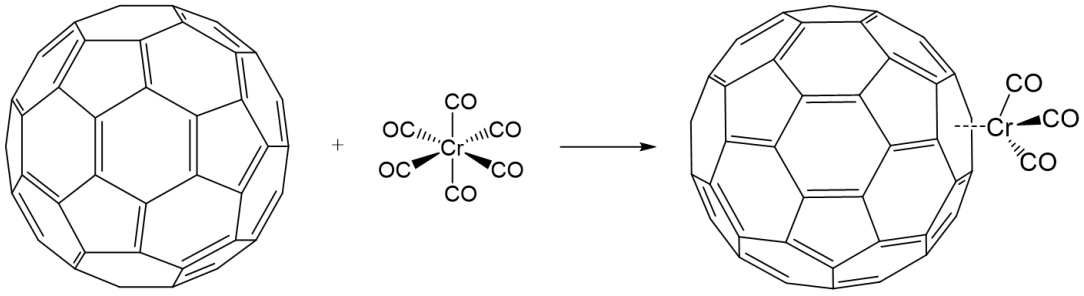

Figure 2.13. Reaction scheme showing the desired η^6 complexation of C_{60} to chromium.

The crude products from these reactions were dried under vacuum to remove the solvent and any unreacted chromium starting material and were analyzed by ^{13}C NMR in carbon disulfide. All three products showed a similar spectrum to the one in Figure 2.14, with a single peak for C_{60}. This indicates that C_{60} was not functionalized with chromium in any of the experiments. Further, there is no evidence of metal carbonyls, which appear at 232.77 ppm in the ^{13}C NMR of $(C_6H_6)Cr(CO)_3$. As a result of the poor solubility of C_{60} in diglyme and cycloctane, this was not very surprising. But, both C_{60} and $(CH_3CN)_3Cr(CO)_3$ showed relatively good solubility in 1,1,1-trichloroethane compared to the other two solvents tested (despite the low solubility of C_{60} reported in the literature), making the reaction more favorable. Additionally, 1,1,1-trichloroethane has a boiling point of 74 ˚C. THF, the solvent used for the reaction between SWNTs and $Cr(CO)_6$ in Chapter 1, has a slightly lower boiling point of 66 ˚C. Therefore, if C_{60} has a similar reactivity toward chromium as SWNTs, 1,1,1-trichloroethane should be an appropriate solvent, especially given the kinetic advantage from C_{60}'s solubility. However, the

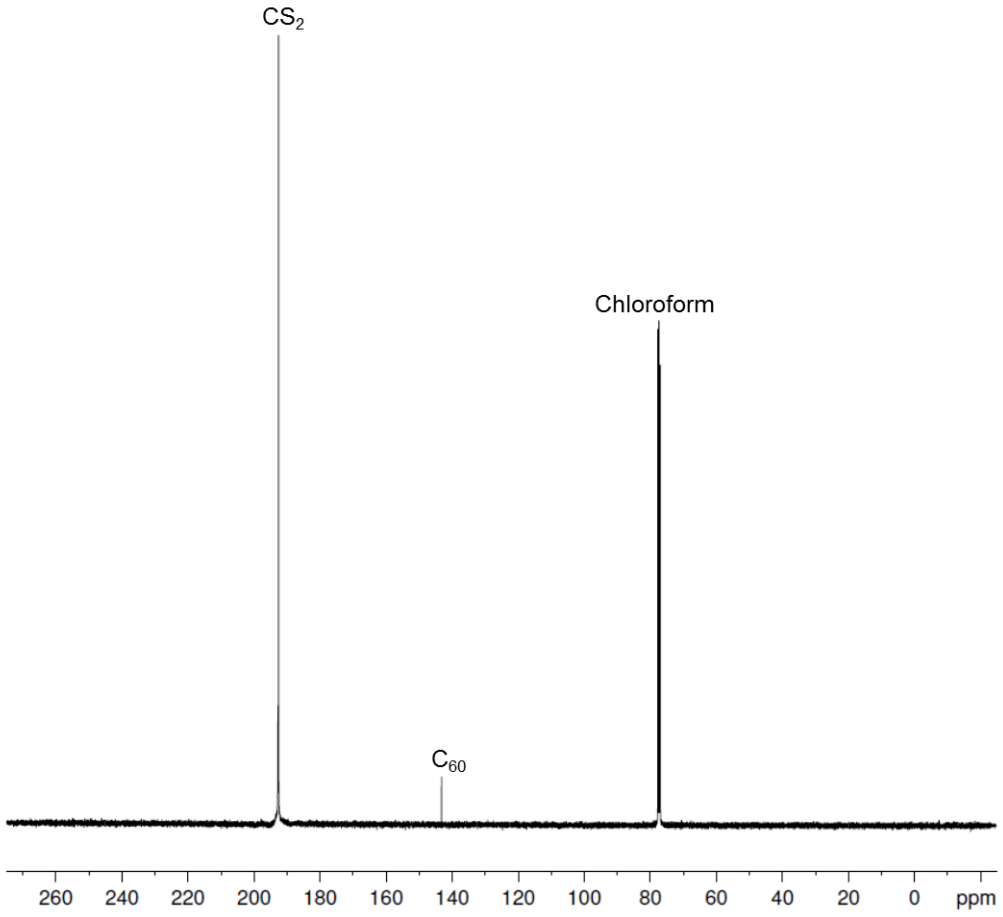

Figure 2.14. ^{1}H NMR of the product of the reaction between C_{60} and $Cr(CO)_6$.

reactivity of SWNTs are very different from that of C_{60}, despite HiPco SWNTs generally having only a slightly smaller diameter (7.10 vs 7.0 Å).[23] This originates from differences is strain in the two molecules- SWNTs have circular strain due to their tube-like geometry, while C_{60} has spherical strain.[23] This translates to a higher degree of pyramidalization of C_{60} at about 11.5˚ compared to HiPco SWNTs at around 5.5˚, where the pyramidalization angle is defined as the angle between the π and σ bonds minus 90˚.[23] For the majority of covalent functionalization reactions, an increase in pyramidalization angle leads to an increase in reactivity; the π bonds are larger on the convex side of the

molecule, increasing orbital overlap with the incoming atom, and the strain on the system is reduced upon binding.[7,23] But, as was discussed in the introduction of this chapter, pyramidalization is not beneficial to the formation of η^6 complexes. Thus, C_{60} is actually less reactive toward Group 6 metals than SWNTs from a pyramidalization standpoint. And, based on this unsuccessful attempt to functionalize C_{60} with chromium, the most reactive of the Group 6 metals, it seems likely that the increased aromaticity reported for the theoretical complex is not correct or is not enough to overcome the hindrance from the pyramidalization.

Conclusions

The hexahapto functionalization of C_{60} with chromium in a variety of different solvents proved to be unsuccessful. From this result, we conclude that the pyramidalization of C_{60}'s π orbitals prevents efficient orbit overlap with the d orbitals of chromium. The instability of the proposed complex from poor orbital overlap, therefore, appears to be more influential than the aromatic stability suggested by theory.[18]

The dihapto functionalization of C_{60} with copper was not confirmed, but was suggested by our results. The attempted synthesis using $[Cu(CH_3CN)_4]BF_4$ as the copper starting material resulted in a mixture of three different copper-mes-dpa complexes, evidenced by their ^{1}H NMR analysis. Based on the obvious structure options given the starting materials and the tetrahedral geometry preference of copper(I), we suggested the formation of $[(C_{60})Cu(mes\text{-}dpa)]BF_4$, $[(CH_3CN)_2Cu(mes\text{-}dpa)]BF_4$ and $[Cu(mes\text{-}dpa)_2]BF_4$. The presence of $[Cu(mes\text{-}dpa)_2]BF_4$ in the product was confirmed after synthesizing this complex and comparing chemical shifts in the ^{1}H NMR spectra. The formation of $[(CH_3CN)_2Cu(mes\text{-}dpa)]BF_4$ was inferred by the presence of a metal-

complexed acetonitrile signal. $[(C_{60})Cu(mes\text{-}dpa)]BF_4$ was then speculated to exist, since there were no other obvious structures to assign to the third set of mes-dpa signals. We also tried forming the complex of interest from $[(C_2H_4)Cu(mes\text{-}dpa)]ClO_4$. This method proved to be better than the previous method, because it eliminates the possibility of forming $(CH_3CN)_2Cu(mes\text{-}dpa)$ and decreases the chances of forming $Cu(mes\text{-}dpa)_2$. Also, the removal of gaseous ethylene is not reversible, and, therefore, encourages the formation of the C_{60} complex. The ^1H NMR of the product formed by this method showed only one set of broadened mes-dpa signals, indicating a single copper-mes-dpa complex. Based on comparison with the products formed using the previous method, we suggested that this product is the desired $[(C_{60})Cu(mes\text{-}dpa)]ClO_4$. However, methods to prove this assignment were not possible as a result of the product's instability.

Experimental

All reagents were used as received unless otherwise noted. Glassware was placed in a base bath overnight, then washed with soap and water and dried in an oven overnight before use. Mes-dpa was synthesized previously and was analyzed by ^1H NMR. $(CH_3CN)_3Cr(CO)_3$ was synthesized using the methods discussed in Chapter 1 immediately before use. Diglyme and cycloctane were stored over molecular sieves and degassed with bubbling argon. 2-Butanol, ethanol, methanol, $CDCl_3$ and 1,1,1-trichloroethane were distilled over CaH_2 and degassed with argon. CD_3OD was degassed under argon. C_{60} fullerene was degassed under vacuum for an hour before use. All reactions were carried out under argon on a Schlenk line. ^1H NMR and ^{13}C NMR spectra were collected on a Bruker 400 MHz instrument.

Reaction of C_{60} with $Cr(CO)_6$ or $(CH_3CN)_3Cr(CO)_3$. C_{60} (0.2 g) and the chromium starting material ($Cr(CO)_6$ or $(CH_3CN)_3Cr(CO)_3$, 0.12 g) were added to a Schlenk flask in the glove box. The solvent (diglyme, cycloctane or 1,1,1-trichloroethane; 15 mL) was added via cannula. The solution was stirred and heated to reflux for four days. The resulting mixture was filtered using inert atmosphere techniques. The filtered powder and the filtrate were analyzed by ^{13}C NMR in CS_2.

Reaction of C_{60} with $[Cu(CH_3CN)_4]BF_4$ and mes-dpa. Mes-dpa (0.3 g), $[Cu(CH_3CN)_4]BF_4$ (0.3 g) and C_{60} (1.5 g) were added to separate Schlenk flasks in the glove box. $[Cu(CH_3CN)_4]BF_4$ was dissolved in 2-butanol (20 mL) and C_{60} was suspended in 1,1,1-trichloroethane (15 mL). The C_{60} suspension was transferred with a large cannula needle to the $[Cu(CH_3CN)_4]BF_4$ solution. The suspension was stirred overnight. Mes-dpa was dissolved in 2-butanol (15 mL) and was transferred via cannula to the $[Cu(CH_3CN)_4]BF_4/C_{60}$ mixture and stirred overnight. The crude product was dried under vacuum and analyzed by ^1H NMR in $CDCl_3$. It was then resuspended in 2-butanol and filtered using inert atmosphere techniques. The filtrate was analyzed by ^1H NMR and ^{13}C NMR in $CDCl_3$.

Synthesis of $[Cu(mes\text{-}dpa)_2]BF_4$. $[Cu(CH_3CN)_4]BF_4$ (0.19 g) and mes-dpa (0.3 g) were added to a Schlenk flask in the glove box. A 1:1 ethanol/methanol mixture (13.5 mL) was added to the flask via cannula. The yellow solution was stirred at room temperature under argon for 2 h and 30 min. An aliquot was then dried under flowing argon and analyzed by ^1H NMR in CD_3OD.

Synthesis of $[(C_2H_4)Cu(mes\text{-}dpa)]ClO_4$. Fine copper powder (0.2 g) and $Cu(ClO_4)_2$ (0.25 g) were added to a Schlenk flask in the glove box. CD_3OD (10 mL) was

added to the flask via cannula, and the mixture was stirred under a slow flow of ethylene overnight. Mes-dpa (0.37 g) was added to the mixture as a powder, causing the solution to turn yellow. The mixture was stirred under ethylene for 30 min, then filtered under argon. An aliquot of the solution was analyzed by ^{1}H NMR. The remaining solution was decreased by about half using bubbling ethylene and was then placed in the freezer overnight. The resulting pale green crystals were isolated from the solution, analyzed by ^{1}H NMR and stored in the glove box for future use.

Reaction of [(C_2H_4)Cu(mes-dpa)]ClO_4 with C_{60}. [(C_2H_4)Cu(mes-dpa)]ClO_4 (0.65 mmol) was dissolved in a 2:1:1 solvent mixture of 1,1,1-trichloroethane, ethanol and methanol (40 mL, or 10 mL of $CDCl_3$). C_{60} (0.45 g) was partially dissolved in 1,1,1-trichloroethane (30 mL). The [(C_2H_4)Cu(mes-dpa)]ClO_4 solution was added to the C_{60} suspension via cannula. The mixture was stirred and bubbled with argon for an hour, then placed under flowing argon overnight. The solution was diluted with ethanol (or CD_3OD) to precipitate unreacted C_{60} and filtered. The $CDCl_3$ reaction was analyzed by ^{1}H NMR and ^{13}C NMR at this point. The resulting solution was bubbled with argon to reduce the volume and placed in the freezer in an attempt to crystallize the product. But, no crystals would form. Further attempts to isolate the product by drying under vacuum or bubbling argon resulted in decomposition.

References

1. H. W. Kroto, J. R. Heath, S. C. O'Brien, R. F. Curl and R. E. Smalley, *Nature*, 1985, **318**, 162–163.

2. P. J. Fagan, J. C. Calabrese and B. Malone, *Science*, 1991, **252**, 1160–1161.

3. M. A. Lebedeva, T. W. Chamberlain and A. N. Khlobystov, *Chemical Reviews*, 2015, **115**, 11301–11351.

4. A. L. Balch and M. M. Olmstead, *Chem. Rev.*, 1998, **98**, 2123–2166.

5. E. D. Jemmis, M. Manoharan and P. K. Sharma, *Organometallics*, 2000, **19**, 1879–1887.

6. R. C. Haddon, *J. Comput. Chem.*, 1998, **19**, 139–143.

7. R. C. Haddon, *Science*, 1993, **261**, 1545–1550.

8. A. L. Balch and K. Winkler, *Chem. Rev.*, 2016, **116**, 3812–3882.

9. J. J. Allen and A. R. Barron, *Dalton T.*, 2009, 878–890.

10. J. S. Thompson and R. M. Swiatek, *Inorg. Chem.*, 1985, **24**, 110–113.

11. J. S. Thompson and J. F. Whitney, *Inorg. Chem.*, 1984, **23**, 2813–2819.

12. J. J. Allen, C. E. Hamilton and A. R. Barron, *Dalton T.*, 2010, **39**, 11451.

13. C. Martín, J. M. Muñoz-Molina, A. Locati, E. Alvarez, F. Maseras, T. R. Belderrain and P. J. Pérez, *Organometallics*, 2010, **29**, 3481–3489.

14. M. Munakata, S. Kitagawa, S. Kosome and A. Asahara, *Inorg. Chem.*, 1986, **25**, 2622–2627.

15. D. A. Edwards and R. Richards, *J. Organomet. Chem.*, 1975, **86**, 407–414.

16. M. Halim, R. D. Kennedy, M. Suzuki, S. I. Khan, P. L. Diaconescu and Y. Rubin, *J. Am. Chem. Soc.*, 2011, **133**, 6841–6851.

17. M. Sawamura, H. Iikura and E. Nakamura, *J. Am. Chem. Soc.*, 1996, **118**, 12850–12851.

18. R. Salcedo, *MRS Proceedings*, 2012, **1483**.

19. J. J. Allen, Ph.D. Dissertation, Rice University, 2011.

20. F. A. Cotton and G. Wilkinson, *Advanced inorganic chemistry*, Wiley, New York, 5th ed., 1988.

21. P. J. Burke, D. R. McMillin and W. R. Robinson, *Inorg. Chem.*, 1980, **19**, 1211–1214.

22. M. Munakata, S. Kitagawa, A. Asahara and H. Masuda, *Bull. Chem. Soc. Jpn.*, 1987, **60**, 1927–1929.

23. R. S. Ruoff, D. S. Tse, R. Malhotra and D. C. Lorents, *J. Phys. Chem.*, 1993, **97**, 3379–3383.

24. S. Talukdar, P. Pradhan and A. Banerji, *Fullerene Sci. Techn.*, 1997, **5**, 547–557.

25. K. N. Semenov, N. A. Charykov, V. A. Keskinov, A. K. Piartman, A. A. Blokhin and A. A. Kopyrin, *J. Chem. Eng. Data*, 2010, **55**, 13–36.

26. Z. Chen, W. Thiel and A. Hirsch, *ChemPhysChem*, 2003, **4**, 93–97.

Chapter 3

Seed Functionalization of Carbon Nanotubes with Copper

Portions of this chapter are included in a manuscript by K.D. Wright, C.E. Gowenlock and A.R. Barron submitted for publication.

Introduction

The majority of power distribution today is via the electrical grid, which relies on aluminium (or copper) cables within an iron sheath. Unfortunately, over 10% of the power transmitted is lost due in the main to resistive heating effects within the cables. To compensate for each 200 MW of line loss, another coal plant has to be on-line. In 2011, summertime electrical generation in the US was 1,026 GW. Therefore, a 10% loss would be equivalent to ca. 200 average-sized coal power plants. Furthermore, because of limits in grid capacity, wind turbines are routinely turned off, because the excess electricity cannot be transported as needed. In addition to issues associated with power loss, the weight of any conductor has a significant impact on energy consumption. This is particularly true in the automotive and aerospace industries.[1]

Proposed long term solutions to the low loss transmission of electricity involve carbon nanotubes (CNTs), in particular metallic single walled carbon nanotubes (SWNTs),[2,3] or high temperature superconducting materials.[4] Both of these approaches have significant technical challenges to be overcome; however, a near term solution involves the improvement in conductivity and ampacity of copper by the addition of CNTs, resulting in a Cu-CNT composite material termed ultraconductive copper

(UCC).[5–7] While undoped CNT fibers show relatively low electrical conductivity experimentally (5 x 10^3 S/cm)[8] compared to copper (5.8 x 10^5 S/cm),[7] they have been shown to have high ampacity (10^5 A/cm^2)[9] which approaches that of copper (10^6 A/cm^2).[7] Individually, CNTs have been reported to have ampacities as high as 10^9 A/cm^2.[10,11] This behavior is typical in conductors; high ampacity occurs in systems with strong bonds, whereas high conductivity occurs in systems with weak bonds.[7] Thus, simultaneous high ampacity and conductivity in a single material is impossible. But, by incorporating CNTs into Cu wires, it may be possible to obtain a composite material with high conductivity as well as high ampacity.[5,7]

The fabrication of such composites has been accomplished in a variety of different ways including electrolytic co-deposition,[12,13] powder metallurgy,[14,15] powder injection molding,[16] electroless plating[17,18] and others. Despite a large number of reports on the fabrication of strong and highly conductive composites,[12,13,15,16] there appears to be little obvious correlation between the Cu-CNT performance and the concentration or identity of the CNTs (SWNTs or MWNTs) or method of fabrication of the composite (Table 3.1). Given the disparate methods reported, developing a consistent controlled route to Cu-CNT composites for future studies is important.

One of the best performing Cu-CNT composites was reported by Subramaniam et al., showing a conductivity of 4.7 x 10^5 S/cm and an ampacity of 630 x 10^6 A/cm^2, which is a 100 fold increase in the ampacity of the Cu-CNT composite versus Cu.[7] Although Subramaniam's reported ampacity may be artificially high due heat transfer from the short test structure (50 μm) to the contacts and the substrate,[9] we were interested in their Cu growth method nonetheless. They reported that the Cu was grown on the CNTs in a

two step process: organic electroplating of seed particles followed by aqueous electroplating to create the bulk.[7] They proposed that a controlled homogeneous seeding of Cu onto the surface is key to their results,[7] suggesting that an understanding of the factors that control this seeding process are important in controlling the Cu-CNT composite formation, and hence its performance.

Table 3.1. A comparison of the conductivities and ampacities of CNT-Cu composites synthesized by various methods.

Material	Method	CNT Load	Conductivity (x 10^5 S/cm)	Ampacity (A/cm^2)
SWNT[5,10,11,19]	N/A	100%	11.3* (theory) 1.9 – 0.08* (exp)	10^9 (theory) 10^7 – 10^9 (exp)
Cu[7]	N/A	N/A	5.8	10^6
Cu-SWNT[5]	Simulation	30 – 40% w/w	12*	N/A
Cu-SWNT[20]	Electroplating	10% v/v	6.06*	N/A
Cu-CNT[7]	Electroplating	45% v/v	2.1 - 4.7	6 x 10^8
Cu-MWNT[21]	Electroplating	1.0 – 1.4% w/w	0.27 – 0.31*	N/A
Cu-MWNT[22]	Electroplating	~10% v/v	4.5*	N/A
Cu-MWNT[23]	Electroplating	~1 g/cm^3	3.22	N/A
Cu-MWNT[18]	Electroless	5% v/v	~ 4.6‡	N/A
Cu-MWNT[15]	Powder metallurgy	0.1% w/w	5.8	N/A

*Conductivity was calculated by taking the inverse of the resistivity. ‡Value was extrapolated from a graph.

Careful study of the protocol reported by Subramaniam et al.[7] shows that they also appear to pre-coordinate Cu(II) ions to the CNTs presumably via sidewall functional

groups,[24] since it is well known that as prepared and after purification CNTs have significant sidewall functionality.[25,26] Our studies confirm the result reported by Subramaniam et al., which indicates the main influence of the CNTs (in Cu-CNT) is to reduce the temperature coefficient of resistivity as compared to Cu, rather than act as additional conduction pathways.[7,20] As such, sidewall purity would not be expected to be important, and in the wide range of Cu-CNT studies, no special care was taken in purifying the CNTs with regard to functional groups (as opposed to the removal of residual catalyst).

We have shown that functionalization with pyridine, phosphines, and thiols of CNTs can be achieved in a number of ways to allow for coordination of metal ions, compounds or nanoparticles.[27,28] Of these substituents, pyridine functionality not only acts as an efficient ligand,[28–30] but also facilitates a decrease in the copper reduction potential, resulting in the preferential reduction of the surface bound Cu(II) to Cu(I).[30–36] This coordinated Cu can then act as a catalyst for the deposition of further Cu(II) ions from solution, allowing controlled seeded growth by electroless deposition.[29,30,37] In the case of CNTs, we have reported that pyridine functionalization may be achieved through 1,3-dicyclohexylcarbodiimide (DCC) coupling of isonicotinic acid (with CNT-OH groups) or 4-hydroxypyridine (with CNT-CO_2H groups).[28]

Based upon the forgoing, we proposed a study to understand and control the seeded growth of Cu on py-functionalized CNTs in order to synthesize templates for subsequent Cu growth. In the present study, we have investigated two classes of CNTs: acid purified HiPco SWNTs and oxidized ultra-short SWNTs (US-SWNTs). The latter have lengths <100 nm and extensively oxidized sidewalls, including carboxylic

groups.[38–40] The comparison between py-functionalized SWNTs (py-SWNTs) and py-functionalized US-SWNTs (py-US-SWNTs) allows for the effects of the concentration of the functional groups (i.e., py:C ratio) to be studied.

Results and Discussion

Characterization of py-SWNTs and py-US-SWNTs. Pyridine functionalized SWNTs and US-SWNTs were prepared according to Figure 3.1, using modifications of previously reported methods.[28]

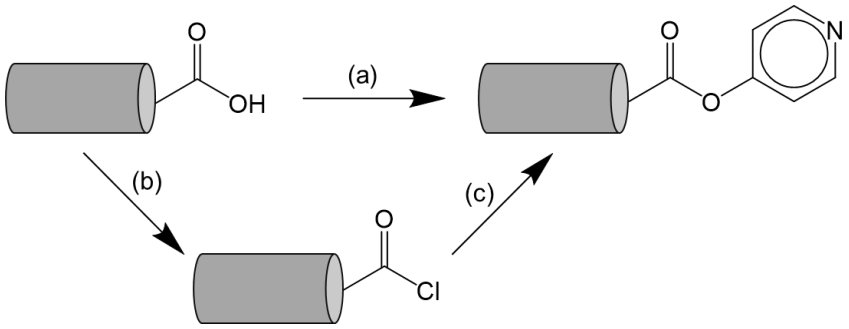

Figure 3.1. Schematic of the synthetic routes to py-functionalized SWNTs by way of (a) 4-hydroxypyridine/DCC/DMAP in MeOH or (b) $SOCl_2$/DMF and (c) 4-hydroxypyridine in $CHCl_3$.

The TEM image of HiPco SWNTs after cleaning by wet oxidation and HCl washing is shown in Figure 3.2. The presence of small unevenly shaped particles (~8 nm), which, given the presence of Fe in the XPS (see below), are likely to be residue from the iron catalyst used in the HiPco process. After piranha etching and functionalization, some particles are still present, albeit distributed unevenly across the sample (Figure 3.2b). The presence of catalyst residue in py-SWNTs must be taken into

account in considering the seeded growth of Cu, both in terms of TEM characterization, but also with regard to the seeding process.

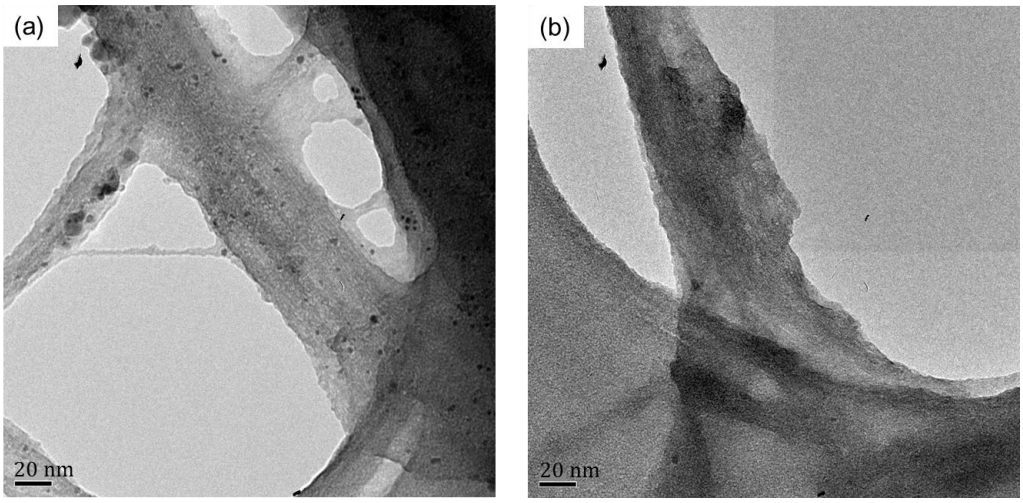

Figure 3.2. TEM image of (a) cleaned HiPco SWNTs and (b) py-SWNTs showing the presence of irregularly shaped nanoparticles with a range of sizes. Scale bar = 20 nm.

In contrast to the HiPco SWNTs, the TEM of the py-US-SWNTs (shown in Figure 3.3) does not show any significant concentration of nanoparticles, suggesting that the Fe catalyst residue (from the HiPco SWNTs from which the US-SWNTs are made) is removed during the synthesis of US-SWNTs.[38,39,41,42] Given the lack of Fe in the XPS, the soft edged dark spots seen in the TEM image are possibly due to small bundles of tubes rather than metals, although the residue observed in the TGA (see below) suggests that some (1.3% w/w) catalyst residue is present.

TGA of piranha etched SWNTs and py-SWNTs in air (Figure 3.4a) show weight loss due to functional groups coinciding with the pyrolysis of the SWNTs. The residue in each case is the oxidized catalyst residue.[43,44] Comparing the initial weight loss beginning at 200 ˚C, the py-SWNTs show a more drastic weight decrease than the piranha etched

SWNTs. This is consistent with the presence of additional functional groups (c.f., Figure 3.1). This is confirmed by the TGA analysis in argon (Figure 3.4b), where weight loss at 850 °C can be attributed to the loss of the functional groups to leave unfunctionalized SWNTs and the catalyst residue.[45] Here, the purified SWNTs, piranha etched SWNTs, and py-SWNTs lose 7.2%, 24.7% and 32.7% respectively. This is consistent with increasing functionality from mild oxidation during purification (epoxides[26]), to more aggressive oxidation during piranha etching (carboxylic acid groups[46]), and to pyridine functionalization.[28]

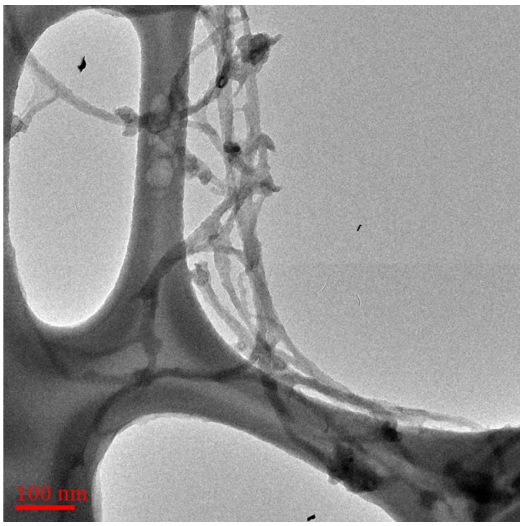

Figure 3.3. TEM image of py-US-SWNTs. Scale bar = 100 nm.

The TGA analysis of oxidized US-SWNTs and py-US-SWNTs in air is shown in Figure 3.5a. Beginning around 200 ˚C, the weight percent begins to drop as a result of the pyrolysis of functional groups. In the case of py-US-SWNTs, there is increased weight loss in this region, indicating that pyridine groups were added to the US-SWNTs (c.f., Figure 3.1) in agreement with the XPS data below. The final drop in weight beginning at

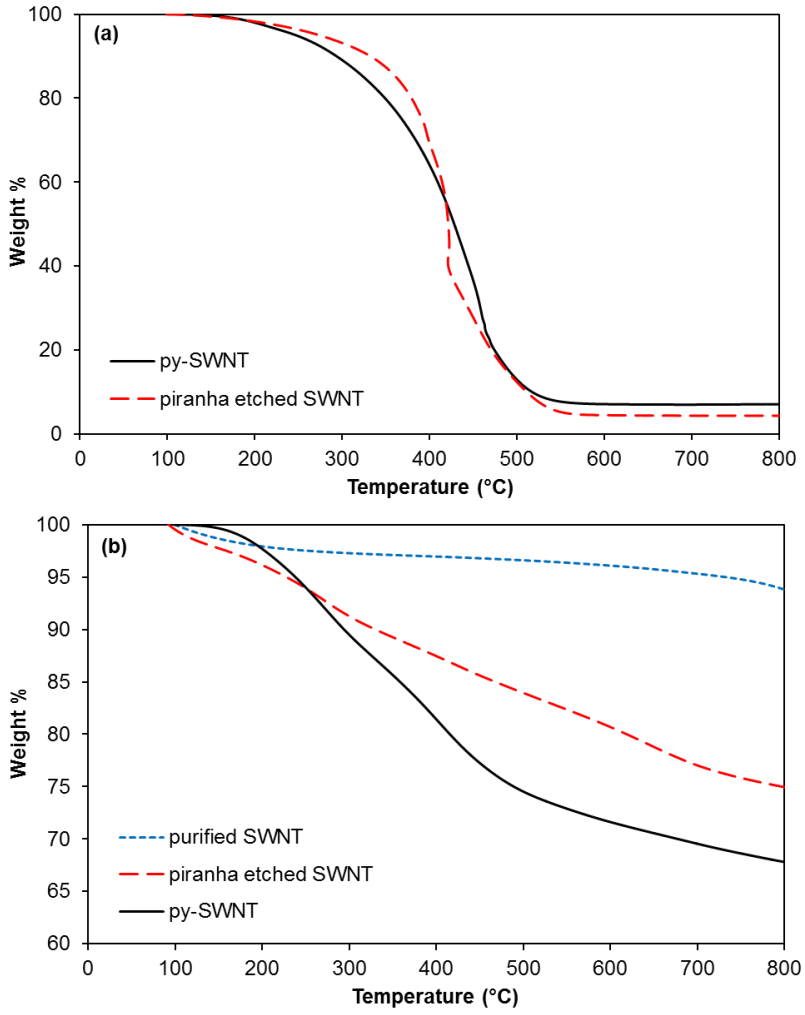

Figure 3.4. TGA of (a) piranha etched SWNTs and py-SWNTs in air and (b) purified SWNTs, piranha etched SWNTs, and py-SWNTs in argon.

500 ˚C corresponds to the burning of US-SWNTs. The residue remaining at 800 ˚C only contributes 1.4% w/w to the US-SWNT samples, indicating a very small residual catalyst content. This is consistent with XPS, which did not indicate any significant Fe content (see below). The TGA in argon of the US-SWNT samples shows an increase from 20.3% to 24.8% w/w contribution of functional groups on oxidized US-SWNTs and py-US-

SWNTs, respectively, indicating that the oxidized US-SWNTs were functionalized with pyridine groups (Figure 3.5b).

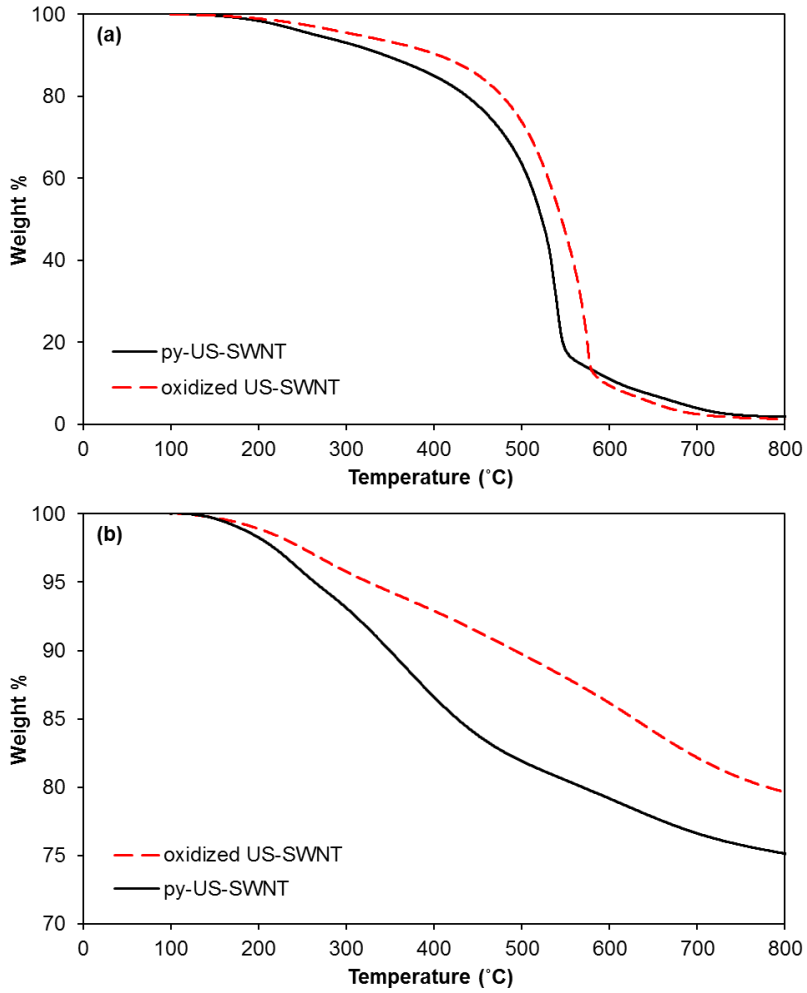

Figure 3.5. TGA of oxidized US-SWNTs and py-US-SWNTs in (a) air and (b) in argon.

XPS analysis of the purified SWNTs shows an O:C ratio of 1:12.9 which increases to 1:6.9 for the piranha etched SWNTs (Table 3.2), consistent with significant sidewall functionalization having taken place. XPS analysis of py-SWNTs and py-US-SWNTs both show the presence of nitrogen (e.g., Figure 3.6), confirming the

Table 3.2. XPS analysis and element ration for purified and functionalized SWNTs.

Sample	C (%)	O (%)	N (%)	Fe (%)	N:C ratio	O:C ratio	N:O ratio
purified SWNTs	92.8	7.2	0.0	0.0	n/a	1:12.9	n/a
piranha etched SWNTs	86.1	12.5	0.0	1.4	n/a	1:6.9	n/a
py-SWNTs	86.9	11.6	1.2	0.3	1:73.0	1:7.5	1:9.7
US-SWNTs	87.5	12.5	0.0	0.0	n/a	1:7.0	n/a
py-US-SWNTs	82.8	15.0	2.2	0.0	1:38.8	1:5.4	1:7.1

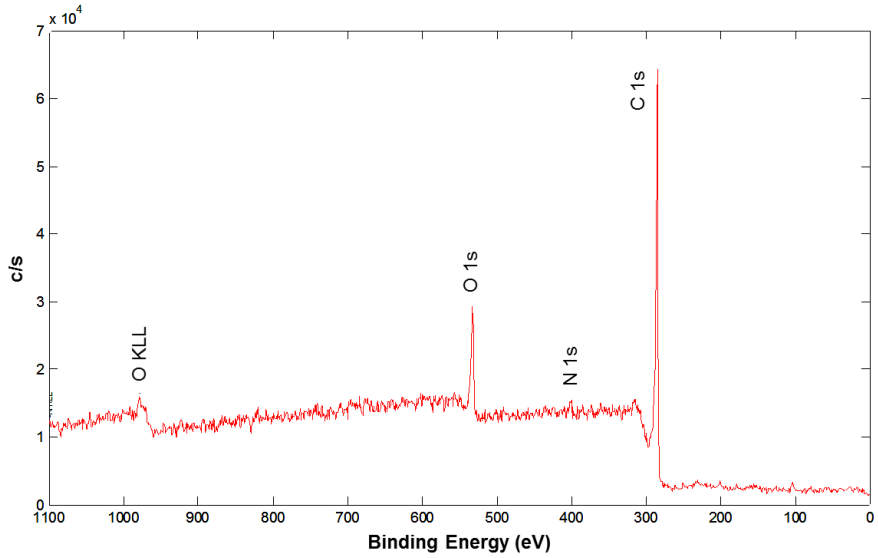

Figure 3.6. XPS survey scan for US-SWNT.

functionalization with pyridine substituents (Table 3.2). If it is assumed that all of the oxygen present on the samples is in the form of carboxylic acid groups (-CO_2H) and that all of these become functionalized upon reaction (Figure 3.1) then a N:O ratio of 1:2 is expected. However, the observed ratio for py-SWNTs is 1:9.7, while for py-US-SWNTs

the ratio is 1:7.1. The lower N:O ratios suggest that either the reaction is incomplete or that much of the O content is associated with non-carboxylic acid functionality. An explanation for this would be that more of the oxygen signal in the py-SWNT could be due to sidewall epoxide groups, consistent with previous studies which show that supposedly purified SWNTs can contain significant epoxide substitution.[26] The N:C ratio represents a measure of the number of pyridine functional groups per unit length of the CNT. As such, the ratio for py-SWNTs is lower (1:73.0) than that for py-US-SWNTs (1:38.8), showing that the ultra-short tubes contain a greater amount of pyridine functionality than the sample derived from piranha etched SWNTs.

Deconvolution of the O1s spectra of piranha etched SWNTs and US-SWNTs (Figure 3.7) show a ratio of oxygen atoms in carboxyl groups to carbon atoms of 1:72 and 1:42, respectively. This would suggest a higher carboxylic acid functionality content in US-SWNTs, which is consistent with the higher py functionality. Indeed, these ratios are very similar to the N:C ratios in Table 3.2, suggesting that most of the carboxylic acid groups are functionalized with pyridine. In fact, from the composition, it is possible to determine that for both py functionalized samples the N:carboxylic acid ratio is ca. 1:1, suggesting both a high conversion and uniform reactivity.

With regard to the Fe content observed in Table 3.2, it was found that the XPS results varied depending on the area analyzed. In addition, residual catalyst is often encapsulated with amorphous carbon, resulting in a lower Fe signal than expected.

Cu(II) binding to py-SWNTs and py-US-SWNTs. To determine how well copper ions interact with py-SWNTs and py-US-SWNTs before they are reduced to zero-valent copper, a UV-visible spectroscopy experiment was conducted to measure the

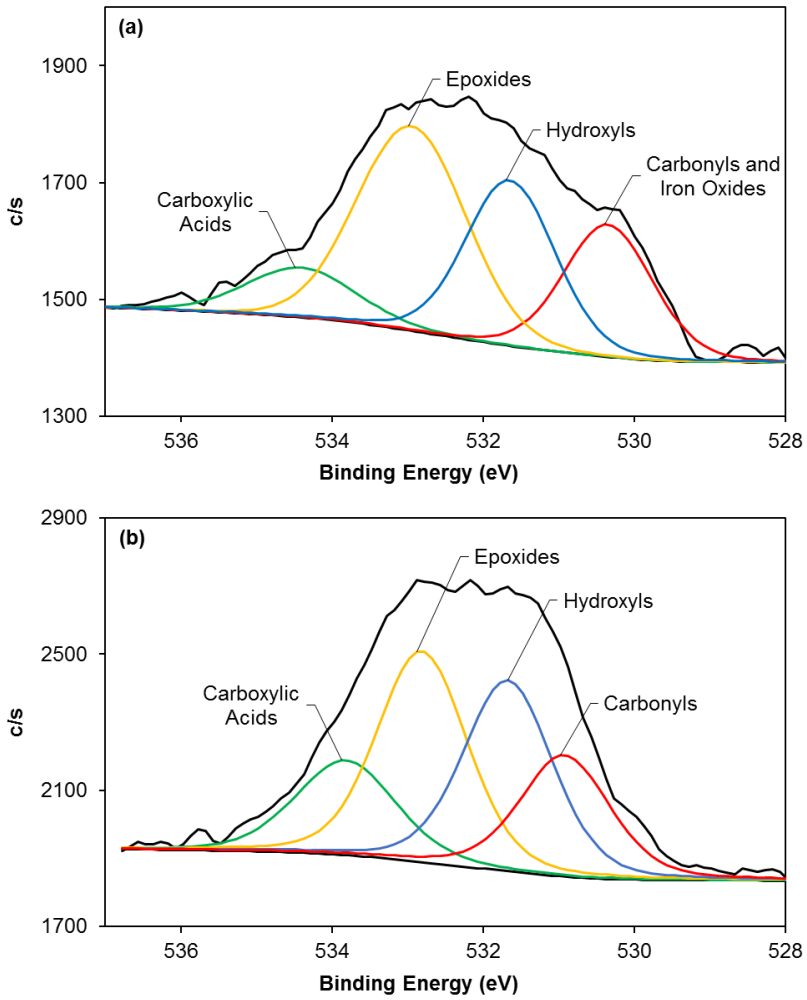

Figure 3.7. High resolution O1s XPS peaks for (a) piranha etched SWNTs and (b) US-SWNTs.

adsorption of Cu(II) ions from a standard solution. All SWNT and US-SWNT samples were suspended in copper nitrate solutions for 24 hours, then filtered. The resulting filtrate solution was analyzed by UV-visible spectroscopy. As can be seen in Figure 3.8, the maximum absorbance (790 nm) decreases upon addition of both carboxylic acid functionalized SWNTs (US-SWNTs and piranha etched SWNTs) and pyridine functionalized SWNTs (py-US-SWNTs and py-SWNTs). From these spectra, the specific

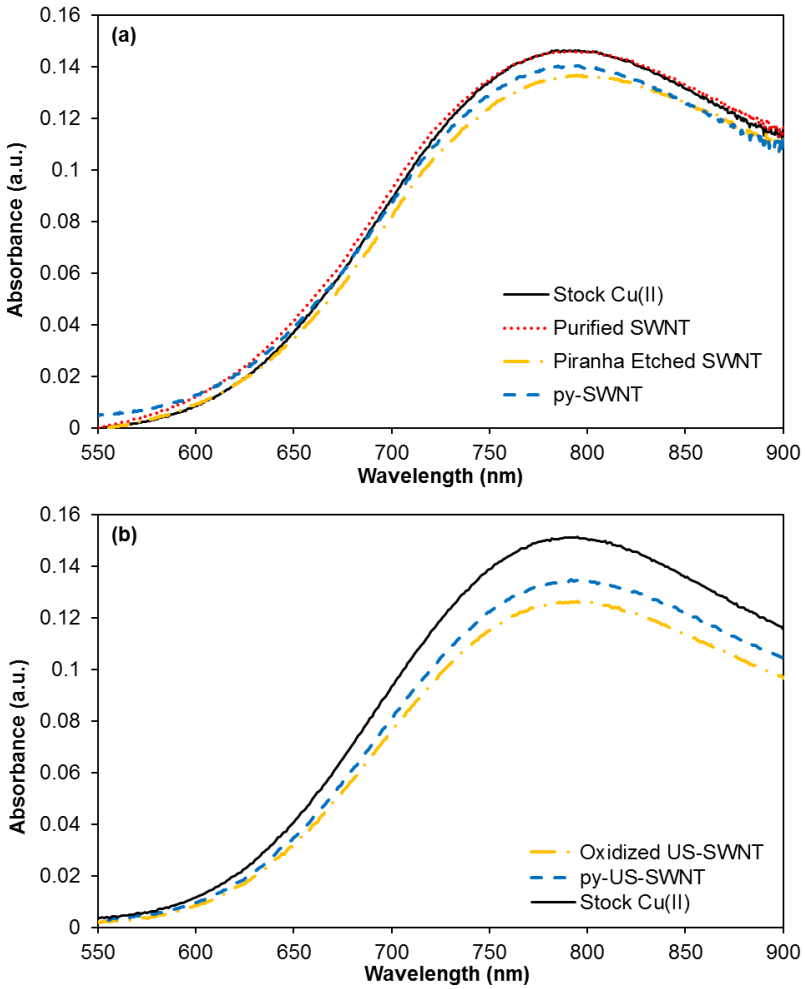

Figure 3.8. The UV-visible absorbance of copper solutions filtered from (a) purified SWNTs, piranha etched SWNTs and py-SWNT and from (b) oxidized US-SWNTs and py-US-SWNTs.

adsorption (mg Cu/g SWNT) may be calculated (Table 3.3). As an example, the absorption decreases from 0.15098 a.u. for the stock copper nitrate solution to 0.13383 a.u. for the py-US-SWNT/copper nitrate solution, indicating that copper is being taken up by the py-US-SWNTs. Using the calibration curve in Figure 3.9 and Beer's Law (Equation 1), where *A* is the absorbance of light at a particular wavelength, ε is the molar extinction coefficient, *b* is the path length, and *c* is the concentration of the solution, the

Table 3.3. Weight of copper ions absorbed from a standard divalent copper solution by SWNTs.

Sample	Cu adsorption (mg Cu/g SWNT)
Purified SWNT	0.5
Piranha Etched SWNTs	14.2
py-SWNT	8.0
US-SWNT	14.7
py-US-SWNT	7.3

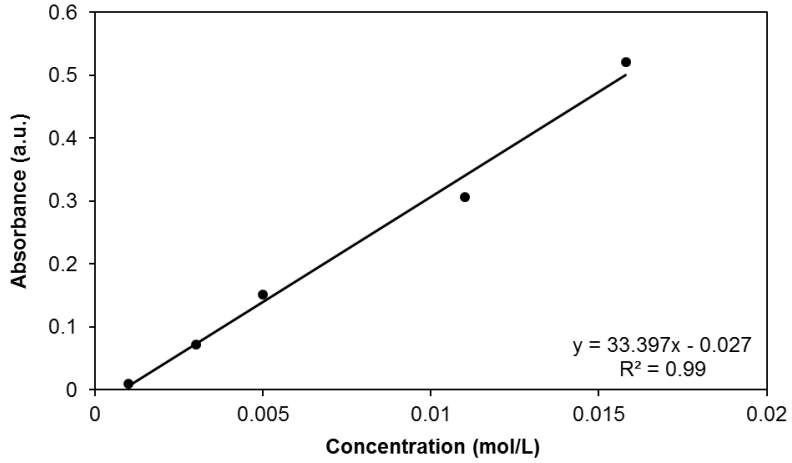

Figure 3.9. The UV-visible absorbance at 790 nm of copper nitrate stock solutions with various concentrations and the equation of the linear fit.

$$A = \varepsilon bc \quad (1)$$

specific adsorption of copper ions was calculated to be 7.3 mg Cu/g py-US-SWNTs. These results show that copper ions have a good interaction with the pyridine functional groups, ensuring that the copper seeds will be bound to those groups upon reduction. For

comparison, a similar experiment was conducted with oxidized US-SWNTs, resulting in a maximum absorbance of 0.12579 a.u. and a corresponding copper absorption value of 14.7 mg Cu/g US-SWNTs. This higher absorption of copper may be attributed to the multiplicity of oxygen species that can bind the Cu(II),[47] or the greater steric bulk of the pyridine functionality hindering binding.[48,49]

Seeded growth of Cu(0) on py-US-SWNTs. Given the low catalyst content in the py-US-SWNTs and the higher concentration of pyridine functional groups per C, the seeded growth of Cu on py-US-SWNTs was investigated first. Copper was seeded onto the py-US-SWNT pyridine groups using electroless plating (Figure 3.10).[37] To determine the best method for Cu seed growth and to understand how different parameters effect the size and quantity of the seeds, a time and concentration study was conducted (Table 3.4).

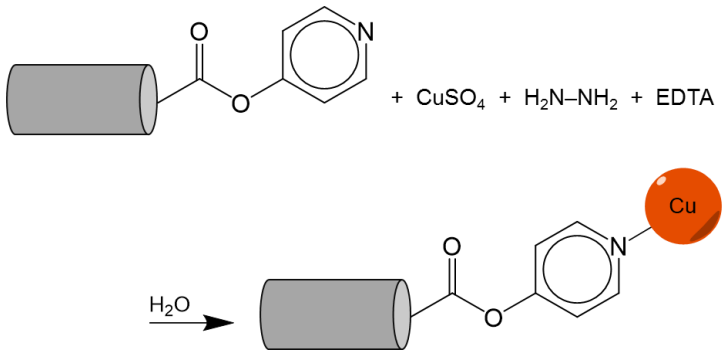

Figure 3.10. Schematic representation of the electroless Cu growth reaction on py-US-SWNTs.

The initial trial (**1** in Table 3.4) employed the same reagent concentrations as a method reported in the literature for Cu growth on isonicotinic acid functionalized alumina,[29,30,37] and the reaction was allowed to proceed until gas evolution stopped. This results in the formation of large (>100 nm) agglomerated cubic particles sparsely

distributed across the sample (Figure 3.11). Unfortunately, no growth is observed on the majority of the py-US-SWNTs. This suggests that the reduction of copper is happening too quickly, i.e., once an initial seed occurs, grain growth occurs rapidly. It is also possible to observe some smaller Cu NPs (35 nm), see Figure 3.11.

Table 3.4. The quantaties of reagents used per liter of water in three different trials of copper electroless plating on py-US-SWNTs.

Trial	Py-US-SWNT (g/L)	$CuSO_4 \cdot 5H_2O$ (g/L)	EDTA (g/L)	Hydrazine (mL/L)
1	0.31	11.84	8.96	28.56
2	0.31	8.88	6.72	21.42
3	0.31	1.48	1.12	3.57

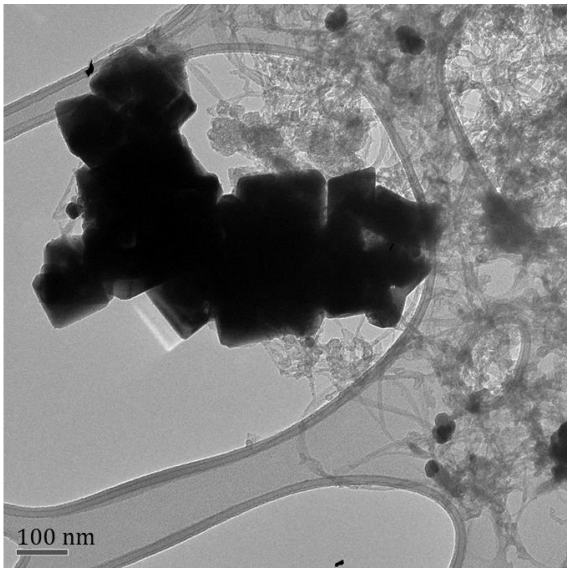

Figure 3.11. TEM image of Cu crystals grown on py-US-SWNTs by electroless deposition using 11.84 g/L $CuSO_4 \cdot 5H_2O$, 8.96 g/L EDTA, and 28.56 mL/L hydrazine in aqueous solution at 25 °C. Scale bar = 100 nm.

In order to slow the reaction, all of the reagent concentrations were reduced to ¾ of their original quantities (**2** in Table 3.4) and the reaction was run for 5, 10, 15 and 30 minutes. The TEM images in Figure 3.12 show large agglomerated cubic crystals of Cu for all four reactions times (120 – 225 nm), with the prevalence of cubes increasing with

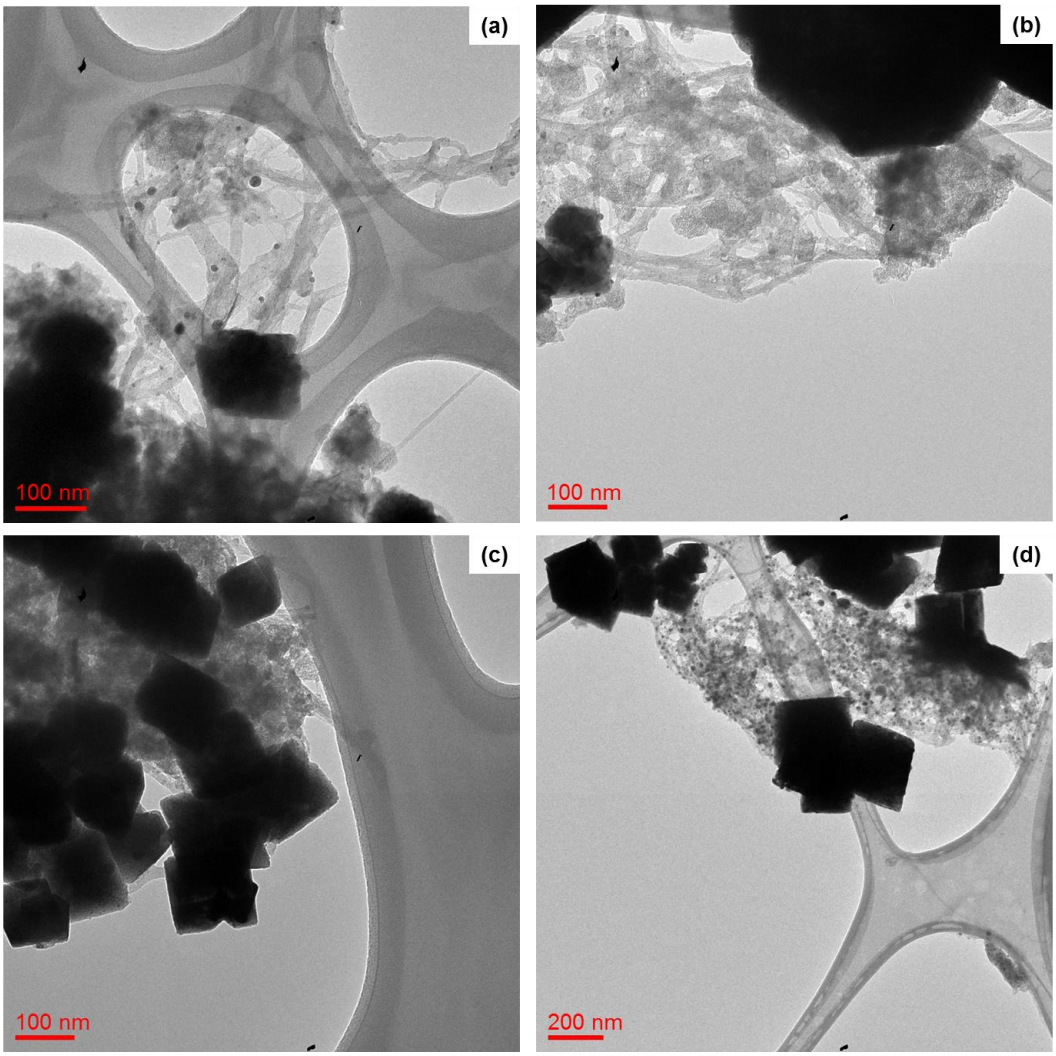

Figure 3.12. TEM images of the electroless deposition of copper onto py-US-SWNTs using 8.88 g/L $CuSO_4 \cdot 5H_2O$, 6.72 g/L EDTA, and 21.42 g/L hydrazine in aqueous solution at 25 °C for (a) 5 min, (b) 10 min, (c) 15 min, and (d) 30 min of reaction time. Scale bar = 100 nm (a-c) and 200 nm (d).

time. However, the occurrence of the desired small Cu spheres increased overall relative to the higher concentration reaction and also increases with increasing reaction time (Figure 3.12d).

In an effort to eliminate the large cubes and maximize the small spheres, the reaction was run with $^1/_8$ of the original reagent concentrations for 2, 5, 10, 15 and 30 minutes (**3** in Table 3.4). The TEM images in Figure 3.13 shows the growth of many of the desired seed particles, which range in size from 3 – 12 nm for reaction times up to 15 minutes. However, beginning at 5 minutes (Figure 3.13b), larger (>50 nm) spherical particles begin to grow. At 30 minutes, the particles become hexagonal or square in shape, and many of them are not associated with SWNTs at all (Figure 3.13f), suggesting homogeneous crystal growth rather than seeded growth. Additionally, there are very few small spherical particles present after 30 minutes, which may be due to Ostwald ripening.[50] Therefore, to obtain small copper seeds on the SWNTs, the ideal reagent concentrations are $^1/_8$ the reported concentrations and the ideal reaction time is 2 minutes. The resulting material meets the requirements of a uniform dispersion of seeded Cu NPs on the surface of the SWNTs without significant homogeneous nucleation.

The selective area electron diffraction (SAED) pattern for the material after 2 minutes of growth is shown in Figure 3.14. The distance between the center beam and the rings of the diffraction pattern were measured to obtain each ring's *r* value. The pattern was then indexed by inputting two different *r* values into Equation 2 along with possible Miller indices, *h*, *k*, and *l*, for each respective ring.[51] After some trial and error, the rings were assigned to the 111, 200, 220, and 311 atomic planes. This corresponds to a face-centered cubic (FCC) lattice structure.[51]

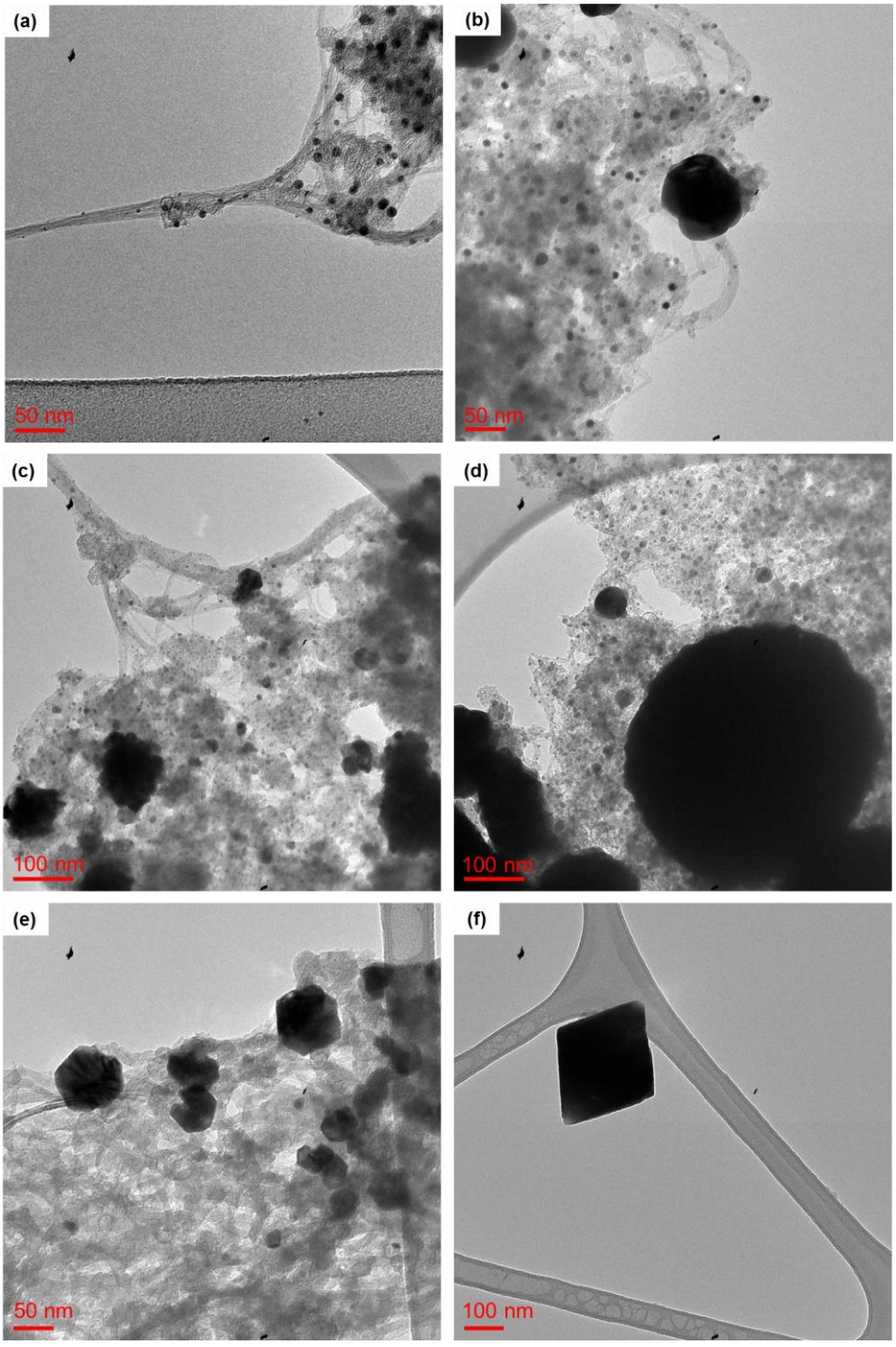

Figure 3.13. TEM images of the electroless deposition of copper onto py-US-SWNTs using 1.48 g/L $CuSO_4 \cdot 5H_2O$, 1.12 g/L EDTA, and 3.57 g/L hydrazine in aqueous solution at 25 °C for (a) 2 min, (b) 5 min, (c) 10 min, (d) 15 min and (e and f) 30 min of reaction time.

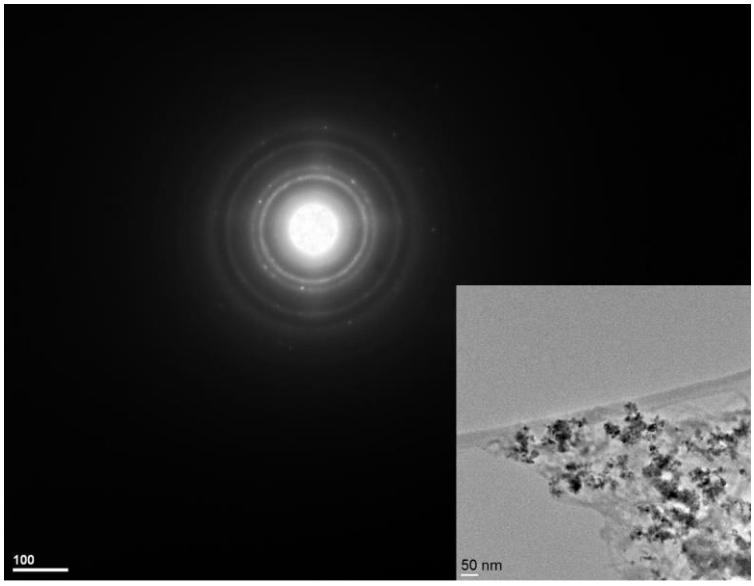

Figure 3.14. The SAED pattern of the electroless deposition of copper onto py-US-SWNTs using 1.48 g/L $CuSO_4 \cdot 5H_2O$, 1.12 g/L EDTA, and 3.57 g/L hydrazine in aqueous solution at 25 °C for 2 mins. The TEM image is shown in the bottom right corner (scale bar = 50 nm). This pattern was obtained using a 100 cm camera length and a 200 kV beam.

$$\frac{r_1}{r_2} = \frac{\sqrt{h_1^2+k_1^2+l_1^2}}{\sqrt{h_2^2+k_2^2+l_2^2}} = \frac{d_2}{d_1} \quad (2)$$

The plane spacing of the crystal, *d*, can be found using Equation 3, where *L* is the distance from the sample to the detector (camera length), λ is the wavelength of the electrons, and *r* is the distance from the resulting diffraction ring to the center beam.[51] The wavelength of the electrons, λ, can be found from the accelerating potential of the electron gun, *U*, using the relation in Equation 4, where *h* is Planck's constant, m_0 is the mass of an electron at rest, *c* is the speed of light and *e* is the elementary charge of an electron. This equation takes into consideration relativistic effects.[51] Using Equation 3,

the plane spacing, *d*, was found for each ring (plane) with a camera length, *L*, of 100 cm and wavelength, λ, of $2.5279*10^{-12}$ m (calculated using Equation 4 with an accelerating voltage, *U*, of 200,000 V).

$$d = \frac{L\lambda}{r} \tag{3}$$

$$\lambda = h\sqrt{2m_0eU\left(\frac{1+eU}{2m_0c^2}\right)} \tag{4}$$

The lattice parameter, *a*, of a cubic crystal is then calculated using the plane spacing, d_{hkl}, and the Miller indices of that plane, *h*, *k*, and *l*.[51] Using the relation in Equation 5, we obtain a lattice parameter, *a*, of 3.6 Å. This, combined with the FCC lattice structure, confirms that this diffraction pattern is from zero-valent copper metal.[51] Further, the SAED leaves little doubt that the observed particles are not from copper oxide, iron, or iron oxides from residual catalyst material because these species have very different lattice structures; CuO has a monoclinic structure,[52] zero-valent iron has a body-centered cubic structure[51] and, under ambient conditions, iron(III) oxide has a rhombohedral or cubic spinel structure.[53] Therefore, the particles shown in the TEM image in Figure 3.14 are confirmed to be zero-valent copper, which is in agreement with the XPS data below.

$$a = \frac{d_{hkl}}{\sqrt{h^2+k^2+l^2}} \tag{5}$$

The XPS analysis of Cu-py-US-SWNTs (e.g., Figure 3.15) confirms the presence of Cu(0) for the 2, 5, 10, 15 and 30 min reaction times (Table 3.5). As expected, the amount of Cu increases from 2 to 5 minutes of reaction time (Figure 3.16). However, contrary to expectations, reaction times between 5 and 15 minutes show similar Cu

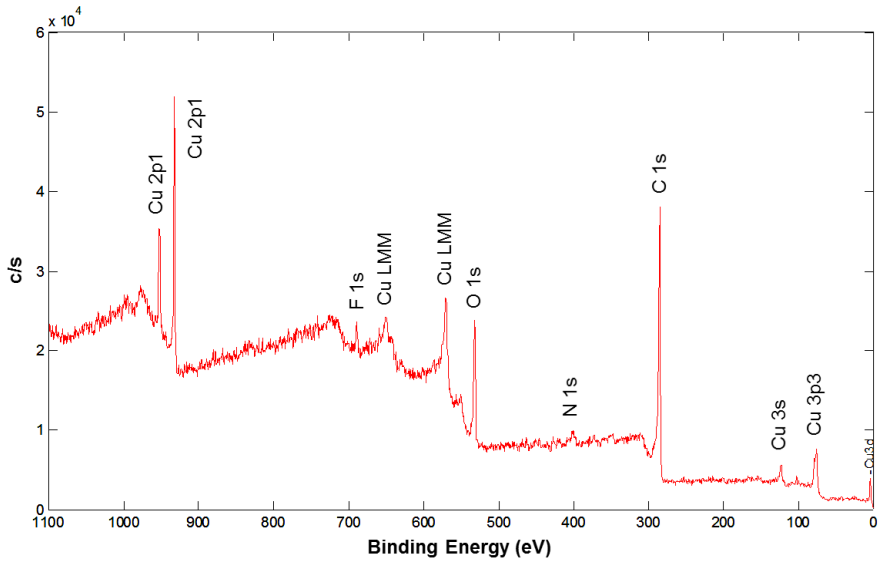

Figure 3.15. XPS survey scan for Cu-py-US-SWNTs prepared using 1.48 g/L $CuSO_4 \cdot 5H_2O$, 1.12 g/L EDTA, and 3.57 g/L hydrazine in aqueous solution at 25 °C for 2 mins.

Table 3.5. XPS analysis and element ratio for Cu seeded py-US-SWNTs.

Reaction time (mins)	C (%)	O (%)	N (%)	Cu (%)
2	74.0	18.8	2.3	4.9
5	73.6	18.1	1.6	6.6
10	72.1	19.7	1.8	6.5
15	72.8	18.8	1.8	6.6
30	74.3	19.1	2.3	4.2

content, and the 30 minute reaction time shows a decrease in Cu concentration. This decrease may be a result of the Ostwald ripening observed in TEM (Figure 3.13e); although the Cu particles are larger, they are also more widely dispersed across the SWNTs. However, this explanation does not hold for the reaction times between 5 and 15

minutes, which showed larger and more densely packed particles with reaction time (Figure 3.13b-d). As these results demonstrate, XPS is not a bulk analysis method, and the location of analysis has an effect on the observed Cu concentration.

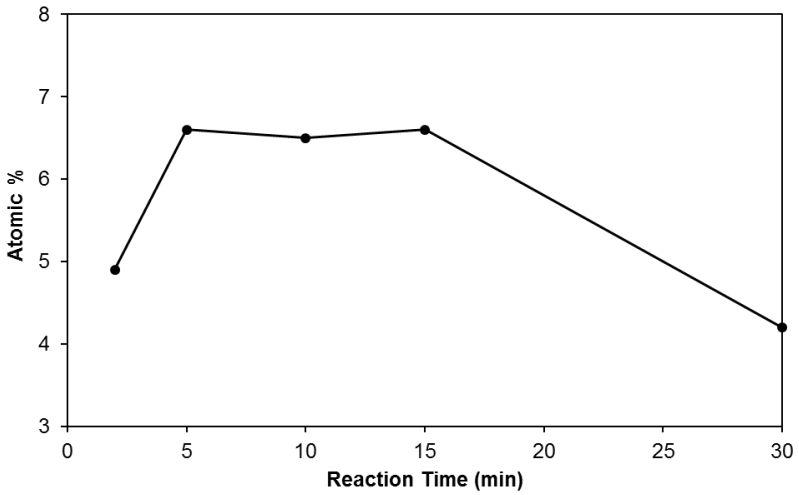

Figure 3.16. Plot of Cu content for Cu-py-US-SWNTs prepared using 1.48 g/L $CuSO_4 \cdot 5H_2O$, 1.12 g/L EDTA, and 3.57 g/L hydrazine in aqueous solution at 25 °C as a function of reaction time.

In agreement with the SAED data, the deconvolution of the high resolution Cu $2p_{3/2}$ XPS signal (Figure 3.17) shows a 91-93% Cu(0) contribution to the overall Cu signal (932.4 eV).[54] The remaining signal is consistent with CuO (933.8 eV),[54] which is presumably on the particle surface. The amount of CuO increases for the 30 min reaction time, resulting in a slightly lower Cu(0) content at 86%.

Given the low levels of Cu and the error in the XPS analysis, TGA was used as an independent method for determining how much Cu is added to the py-US-SWNTs. In this regard, the 2 min and 30 min products were analyzed by TGA in air, such that the residue should represent Cu (oxide) only. The results shown in Figure 3.18 shows the onset of

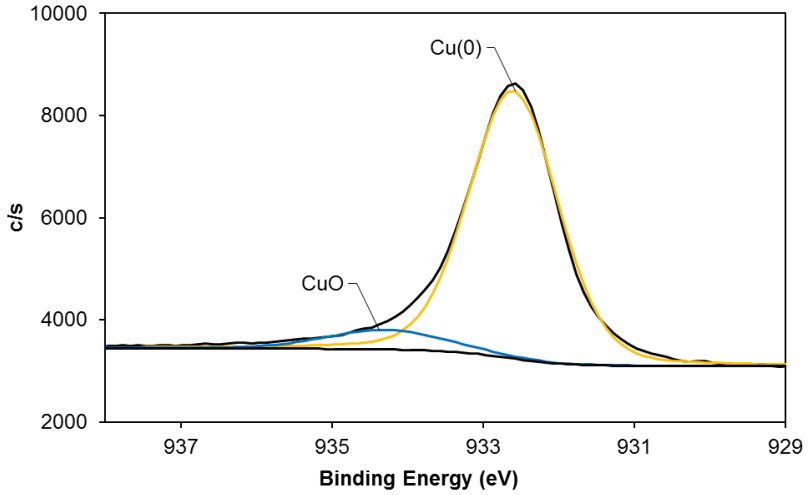

Figure 3.17. The high resolution Cu $2p_{3/2}$ XPS signal for Cu-py-US-SWNTs prepared using 1.48 g/L $CuSO_4 \cdot 5H_2O$, 1.12 g/L EDTA, and 3.57 g/L hydrazine in aqueous solution at 25 °C after a reaction time of 2 min.

combustion around 200 °C, which continues until about 400 °C. Compared to the data for py-US-SWNTs, the range of combustion is shifted down by 200 °C. We suspect that this is due to the combustion catalytic activity of the copper.[55] A steady weight percent is reached at 400 ˚C for the 2 minute reaction and at 500 ˚C for the 30 minute reaction. At this point, the only species left to contribute to the weight percent is copper oxides (assuming negligible residual catalyst content). In agreement with the TEM images (Figure 3.13a and e), these results show an increase in copper with increased reaction time. Comparing these results with those from the UV-visible Cu(II) adsorption experiment (above), more copper was seeded onto the tubes in the 2 min electroless deposition (~220 mg Cu/g py-US-SWNTs) than was adsorbed on the py-US-SWNTs (7.3 mg Cu/g py-US-SWNT). This is expected, since the functional groups on the electroless deposited py-US-SWNTs are bound to seeds that contain many atoms, while the

functional groups in the UV-visible experiment are presumably bound to single copper ions. Doing a similar comparison for the 30 min electroless deposition shows that 2.6 times more copper was deposited on py-US-SWNTs compared to the 2 min reaction. However, as was discussed previously, the TEM image in Figure 3.13e shows sparse coverage of the py-US-SWNTs with large copper particles for the 30 min reaction time. Thus, there are not necessarily more pyridine groups bound by Cu but, rather, there are just larger Cu particles.

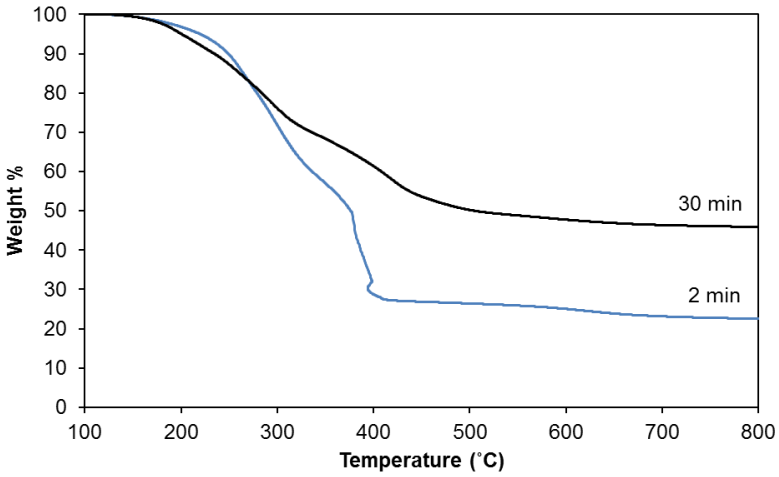

Figure 3.18. TGA in air of Cu-py-US-SWNTs prepared using 1.48 g/L $CuSO_4 \cdot 5H_2O$, 1.12 g/L EDTA, and 3.57 g/L hydrazine in aqueous solution at 25 °C for 2 min and 30 min.

We have shown that with the correct choice of reaction time and reagent concentration, the py-US-SWNTs can be decorated with seed crystals of Cu(0). However, one important question is whether the resulting Cu(0) nanoparticles (NPs) are actually bound to the py-US-SWNTs. To ensure that the copper seeds are bound to the pyridine functional groups, ^{1}H NMR spectroscopy was employed. Because solid state NMR

produces spectra with broad peaks and requires a large amount of material, free Cu particles in solution were used to determine Cu's interaction with pyridine in Cu-py-US-SWNTs. The copper particles were synthesized according to method **3** in Table 3.4, but without py-US-SWNTs. The particles were filtered and then mixed in a D_2O solution of pyridine. This caused the particles to dissolve, generating a clear, brown-orange solution (Figure 3.19). This solution was filtered, and the filtrate was collected in an NMR tube. The resulting ^1H NMR is shown in Figure 3.20a in comparison with that of pyridine (Figure 3.20b). The peaks in the presence of the Cu NPs are shifted downfield and are broadened as compared to the spectra of pyridine (Figure 3.20). Further, the protons that are on the carbon attached to the nitrogen atom ("*o*" in Figure 3.20) show the most severe broadening, suggesting that the copper is bound to the nitrogen atom. To ensure that copper particles were actually present in the NMR sample, the solution was analyzed under TEM. Figure 3.21 confirms that the filtrate does contain copper nanoparticles.

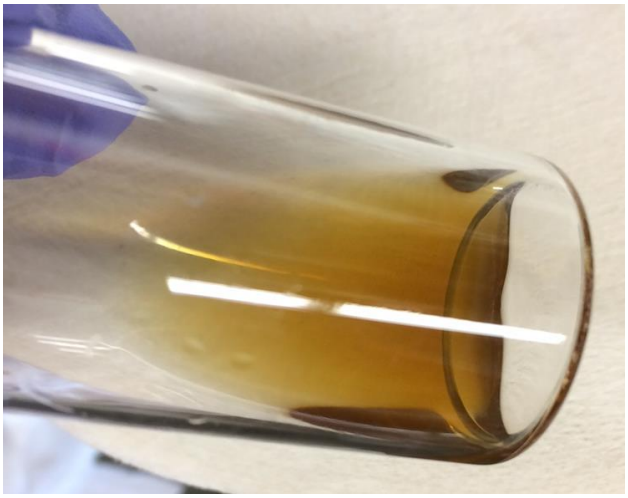

Figure 3.19. Image of dissolved Cu particles in a D_2O solution of pyridine.

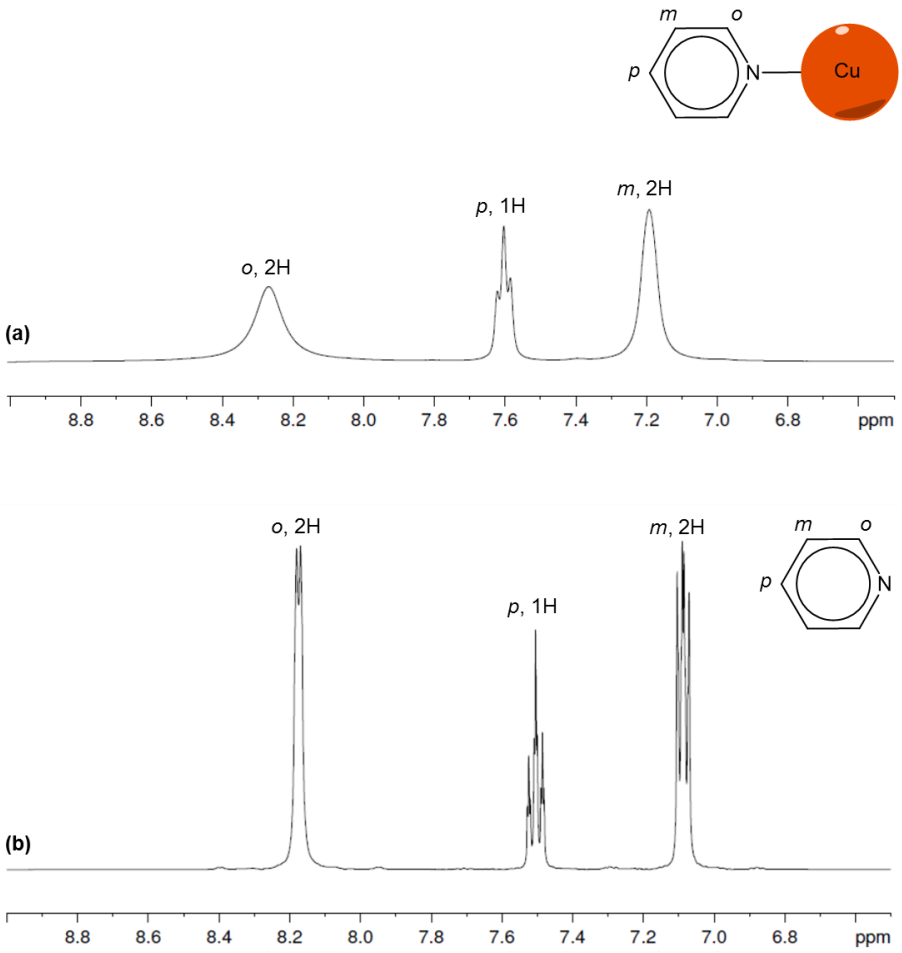

Figure 3.20. ^{1}H NMR spectra of (a) pyridine-capped copper nanoparticles and (b) pyridine in D_2O at 25 °C.

In order to determine the effect that the pyridine functional groups have on Cu morphology, oxidized US-SWNTs were also deposited with Cu using the optimized method for py-US-SWNTs (**3** in Table 3.4). As the TEM images in Figure 3.22 show, deposition on oxidized US-SWNTs results in the formation of Cu particles with a wider size distribution than those on py-US-SWNTs. After 2 minutes of reaction time, which was shown to be ideal for 3–12 nm seed growth on py-US-SWNTs (Figure 3.13a), the Cu

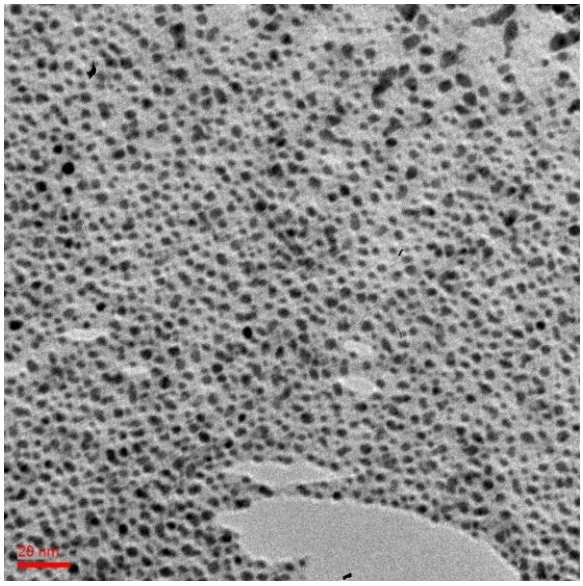

Figure 3.21. The TEM image of the filtrate of a copper particle and pyridine solution. Scale bar is 20 nm.

particles appear comparatively large (~30 nm) and agglomerated (Figure 3.22a). Beginning at 5 min (Figure 3.22b), even larger particles (~100 nm) grow and become more closely packed with increasing reaction time (Figure 3.22b-d). After 30 minutes, large agglomerated particles are seen, but square particles are also formed (Figure 3.22e). Although large amorphous particles are also seen after 5 minutes of reaction time in the presence of py-US-SWNTs, they are much more abundant on the oxidized US-SWNTs. Further, small Cu seeds (2.5 - 5 nm) on oxidized US-SWNTs only occurred intermittently at all reaction times and did not seem to grow in size with deposition time (see Figure 3.22f for a representative image). On the contrary, py-US-SWNTs showed uniform copper seed deposition between 2 and 15 min of reaction time (Figure 3.13a-d). These results show that pyridine functional groups are crucial to the formation of well dispersed Cu seeds with a narrow size distribution (after 2 min) on SWNTs.

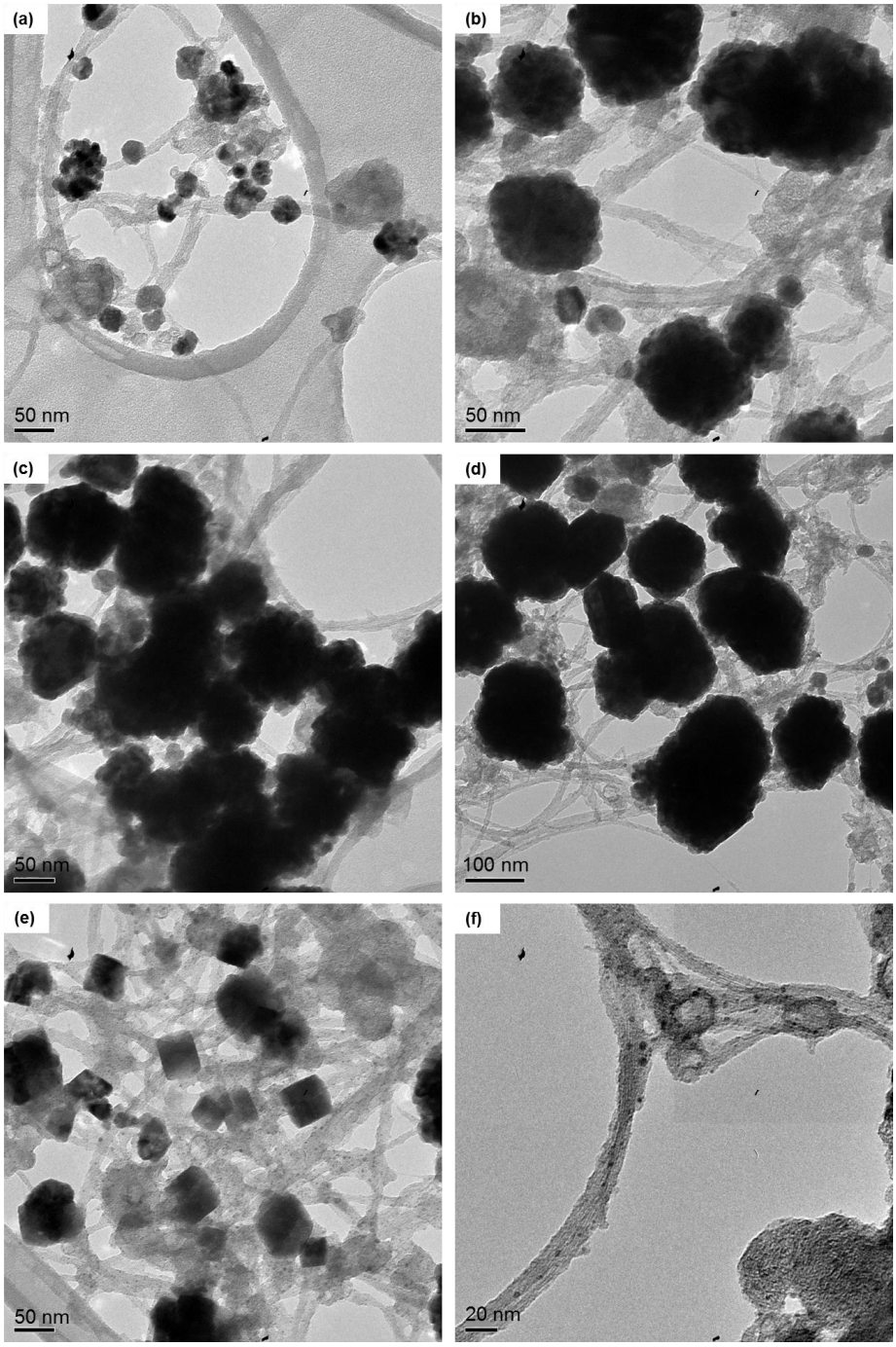

Figure 3.22. TEM images of the electroless deposition of copper onto US-SWNTs using 1.48 g/L $CuSO_4 \cdot 5H_2O$, 1.12 g/L EDTA, and 3.57 g/L hydrazine in aqueous solution at 25 °C showing large particle growth at (a) 2 min, (b) 5 min, (c) 10 min, (d) 15 min and (e) 30 min of reaction time and (f) some intermittent seed growth at all reaction times. Scale bars are (a,b,c,e) 50 nm, (d) 100 nm and (f) 20 nm.

Seeded growth of Cu(0) on py-SWNTs. Given the success of the aqueous electroless deposition results with py-US-SWNTs, the first trial conducted with py-SWNTs was also in aqueous medium with the same reagent concentrations as the optimized method for py-US-SWNTs (Table 3.4), as shown in **4** of Table 3.6. After 2 min of reaction time, the TEM image of the resulting sample showed a uniform dark staining of the py-SWNTs (Figure 3.23a) compared to unreacted py-SWNTs (Figure 3.23b). They also showed irregularly shaped particles that are typical of residual catalyst material (Figure 3.23). The stained appearance suggests that Cu is deposited in a very uniform manner along the entire length of the py-SWNTs. However, we do acknowledge that the appearance of the TEM image changes depending on how over- or under-focused it is. Therefore, the presence of Cu was confirmed by energy dispersive X-ray spectroscopy (EDX) mapping of the surface of py-SWNT after 2 min Cu deposition (Figure 3.24). The Cu K_α EDX map (Figure 3.24c) shows copper distributed over the entire surface of the sample, consistent with the dark staining of the py-SWNTs seen in Figure 3.23a. Further, the defined particles seen in TEM images are confirmed to be catalyst material by the Fe K_α EDX map (Figure 3.24b). For comparison, EDX mapping was also used to characterize unreacted py-SWNTs (Figure 3.25). Here, the Cu K_α map

Table 3.6. The quantities of the reagents used per liter of solvent in two different trials of copper electroless plating on py-SWNTs.

Trial	Py-SWNT (g/L)	$CuSO_4 \cdot 5H_2O$ (g/L)	EDTA (g/L)	Hydrazine (mL/L)	Solvent
4	0.31	1.48	1.12	3.57	H_2O
5	1.73	84.07	-	25.38	MeOH

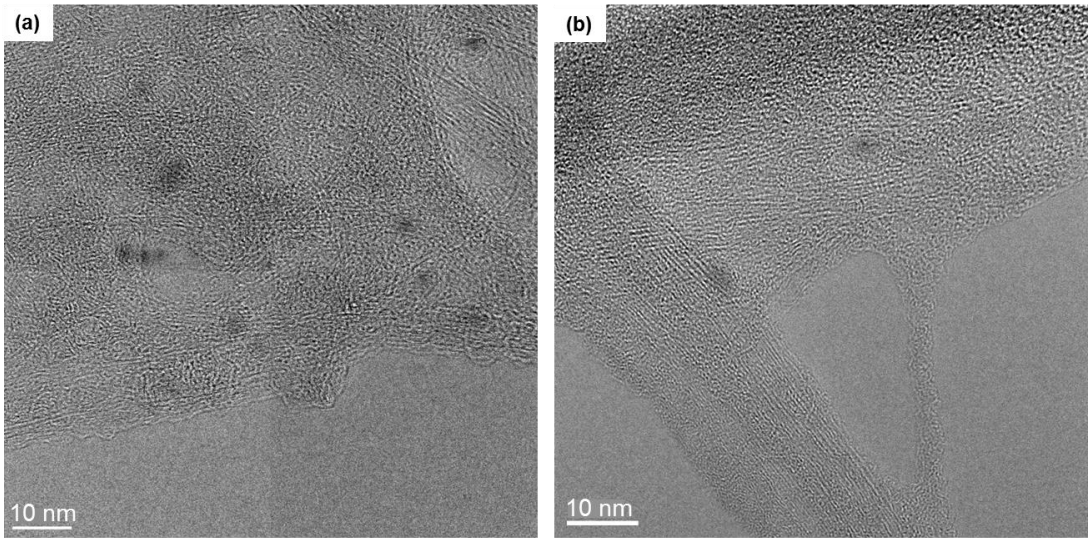

Figure 3.23. TEM images of (a) the electroless deposition of copper onto py-SWNTs using 1.48 g/L $CuSO_4 \cdot 5H_2O$, 1.12 g/L EDTA, and 3.57 g/L hydrazine in aqueous solution at 25 °C for 2 min of reaction time and (b) py-SWNTs.

also shows Cu signals, but these are dispersed evenly across the map, including in regions of vacuum (Figure 3.25c). Because these signals do not correlate with the py-SWNTs in the scanning transmission electron microscopy (STEM) image (unlike those for Cu functionalized py-SWNTs in Figure 3.24c), they are attributed to scattered X-rays from the Cu sample holder. These results confirm that Cu deposition on py-SWNT with short reaction times results in a highly uniform coating of Cu across the CNT surface.

When the reaction is allowed to proceed for 30 min, large spherical particles are then formed as well as small nanoparticle seeds of Cu (Figure 3.26). The small seeds show a similar morphology to the copper seeds obtained with py-US-SWNT after 2 and 5 min reaction times (Figure 3.13a and b). However, this result suggests that while a uniform distribution of Cu onto the SWNT surface is the initial result, either not all these act as potential seeds or, once a seed grows, Ostwald ripening results in a small number

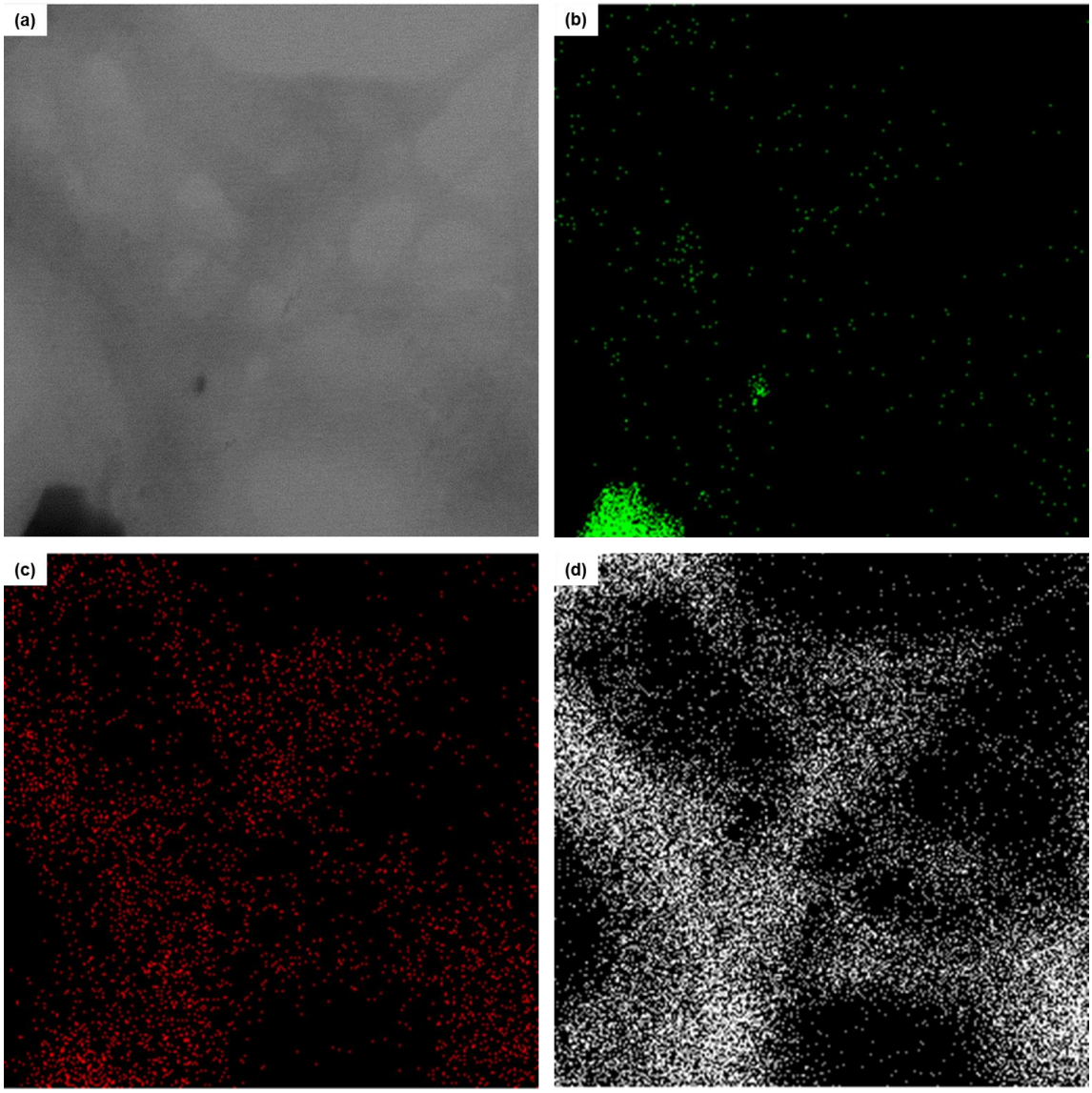

Figure 3.24. STEM image (a) and associated EDX maps of (b) Fe, (c) Cu and (d) C of a sample of py-SWNT after electroless deposition of copper using 1.48 g/L $CuSO_4 \cdot 5H_2O$, 1.12 g/L EDTA, and 3.57 g/L hydrazine in aqueous solution at 25 °C for 2 min of reaction time.

growing. Interestingly, if the sample shown in Figure 3.23 was subjected to secondary Cu electroless deposition, the morphology of the resulting Cu features is very similar to that observed for py-US-SWNTs. After 5 min of secondary reaction time, there were many

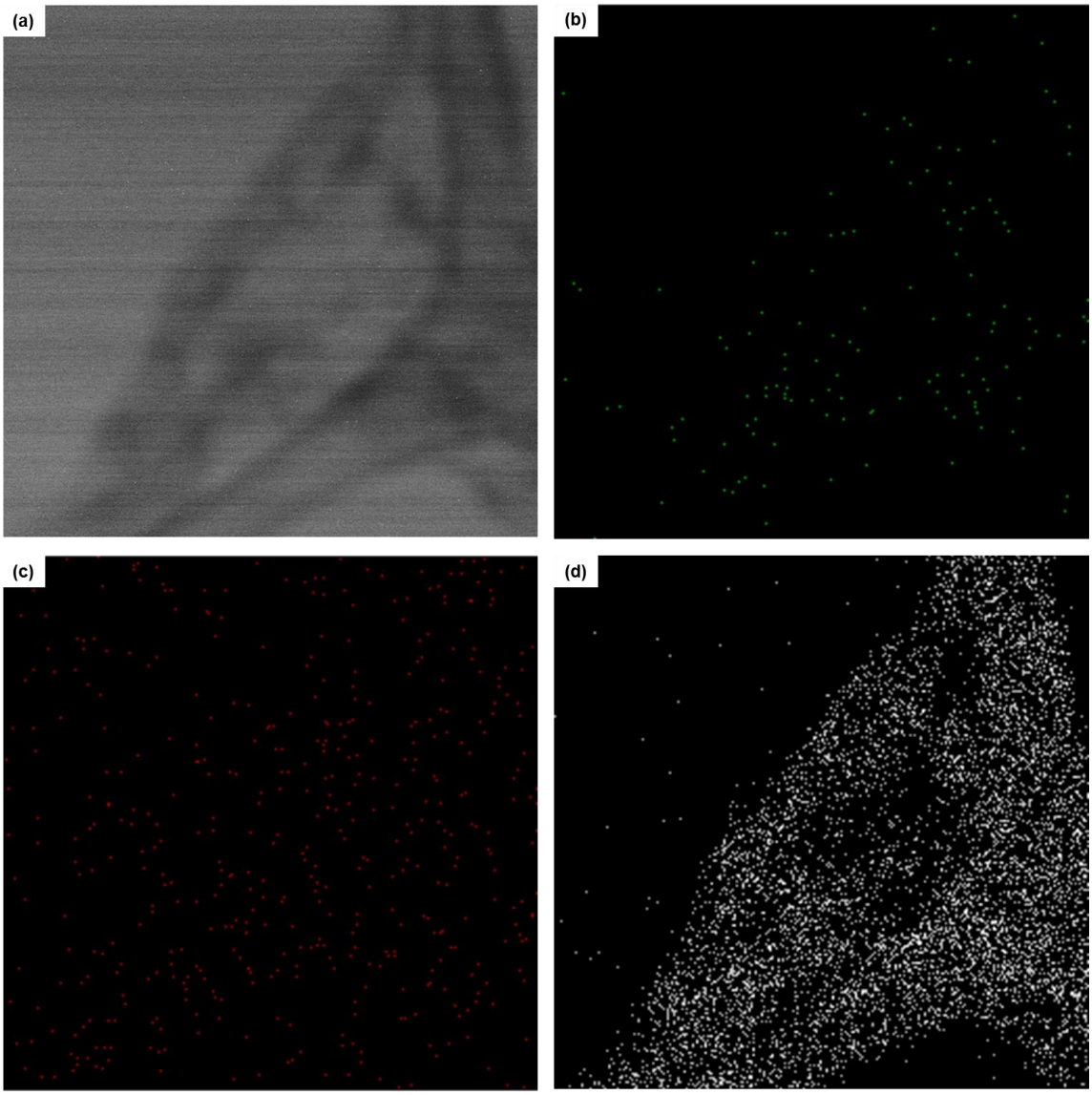

Figure 3.25. STEM image (a) and associated EDX maps of (b) Fe, (c) Cu and (d) C of a sample of py-SWNT.

small spherical copper seeds formed (Figure 3.27). However, as with the py-US-SWNTs, it is difficult to inhibit the extended growth and formation of a few larger particles.

The above results for the aqueous deposition of Cu on SWNTs shows a clear difference in the rate at which the Cu particles form on the tubes compared to similar

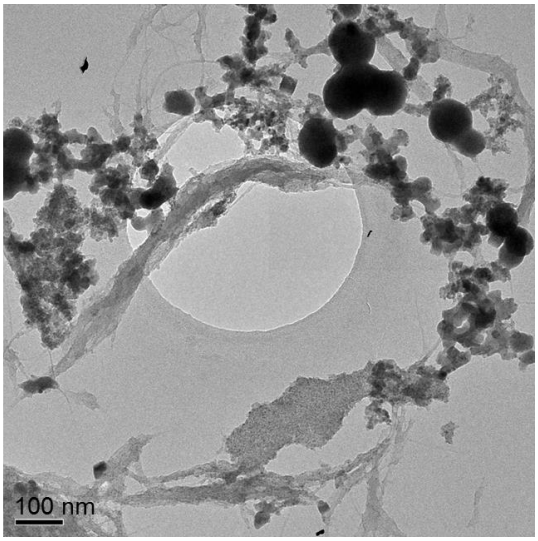

Figure 3.26. TEM image of py-SWNTs after electroless deposition of copper using 1.48 g/L $CuSO_4 \cdot 5H_2O$, 1.12 g/L EDTA, and 3.57 g/L hydrazine in aqueous solution at 25 °C for 30 min reaction time, showing large particles of copper and clusters of small copper seeds.

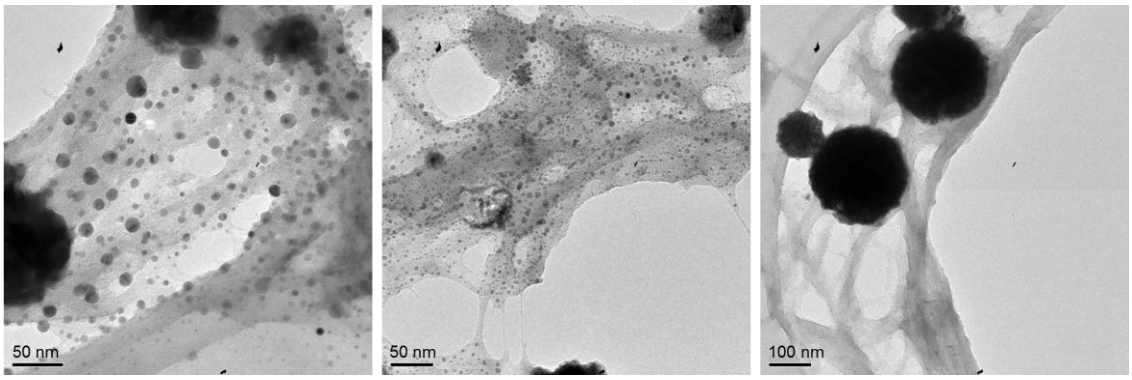

Figure 3.27. TEM images of py-SWNTs after two rounds of electroless deposition of copper using 1.48 g/L $CuSO_4 \cdot 5H_2O$, 1.12 g/L EDTA, and 3.57 g/L hydrazine in aqueous solution at 25 °C for 2 min and then for 5 min under identical conditions.

depositions on US-SWNTs. Although this may be the result of a combination of factors such as tube length and degree of pyridine functionality, we also suspected that the low dispersability of SWNTs in water might play a role in this as well. For this reason, a second trial (**5** in Table 3.6) of electroless deposition of copper on the py-SWNTs was conducted in MeOH to aid suspension of the py-SWNTs. Because EDTA showed low solubility in MeOH, it was omitted from the reaction. After 30 mins of electroless deposition, the TEM image showed a dark coating over the surface of the py-SWNTs (Figure 3.28a), similar to that observed in the aqueous deposition (Figure 3.23). There was also the presence of small nanoparticles (Figure 3.28b), but these are likely due to Fe rather than Cu seeds given their irregular shape (see Figure 3.2a) and the EDX results above (Figure 3.24).

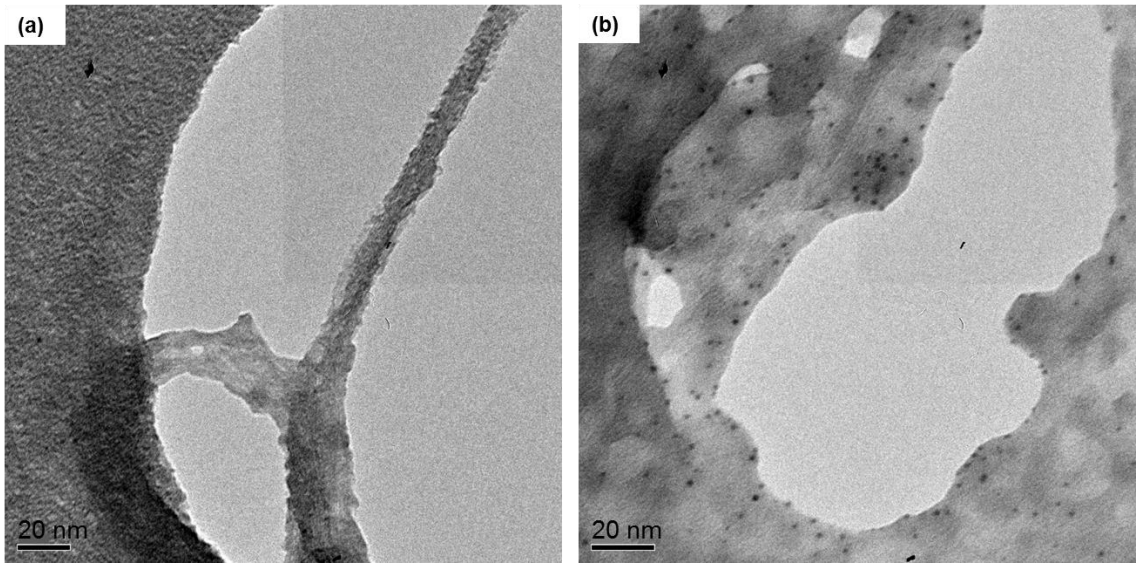

Figure 3.28. TEM images of the electroless deposition of copper onto py-SWNTs using 84.07 g/L $CuSO_4 \cdot 5H_2O$ and 25.38 mL/L hydrazine in MeOH solution at 25 °C for 30 min of reaction time, showing (a) SWNTs with a dark coating and (b) residual catalyst particles. Scale bars are 20 nm.

If the electroless deposition was allowed to proceed for 24 h, eventually the copper growth forms ‘sea urchin’ type structures (Figure 3.29). Although the concentration of the SWNTs and $CuSO_4 \cdot 5H_2O$ are higher than any of the US-SWNT trials, it is interesting that the morphology of the Cu is vastly different from that with extended growth using py-US-SWNTs. Further, the 30 minute deposition in MeOH with higher $CuSO_4 \cdot 5H_2O$ and without Cu(II)-complexing EDTA resulted in the same Cu morphology as the 2 minute aqueous reaction. Because the 30 minute aqueous reaction showed the presence of large particles and Cu seeds, it seems that the MeOH actually reduces the reaction rate or alters the solubility/reactivity of the py-SWNTs.

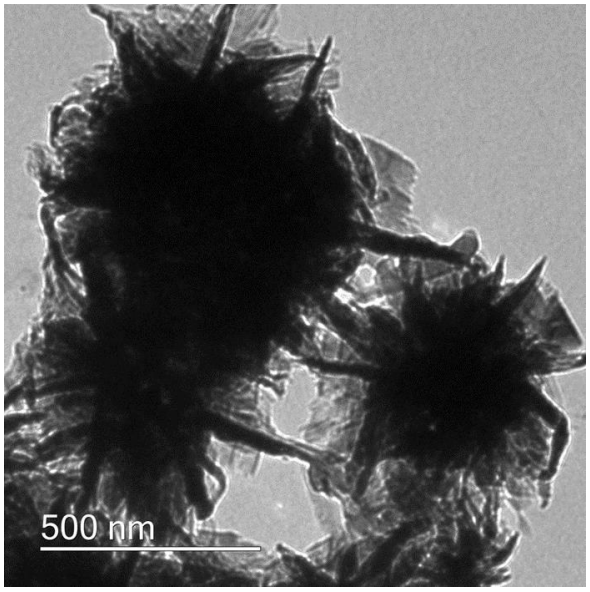

Figure 3.29. TEM images of the electroless deposition of copper onto py-SWNTs using 84.07 g/L $CuSO_4 \cdot 5H_2O$ and 25.38 mL/L hydrazine in MeOH solution at 25 °C for 24 h of reaction time showing the growth of ‘sea urchin’ type structures.

To determine how much copper has been grown on the py-SWNTs, the 2 min and 24 h electroless deposition products were analyzed by TGA in air (Figure 3.30). Residues

at the end of the TGA analysis can be attributed to copper and iron oxides, with the 24 h sample clearly showing a greater residue than the 2 min sample, in agreement with the TEM images.

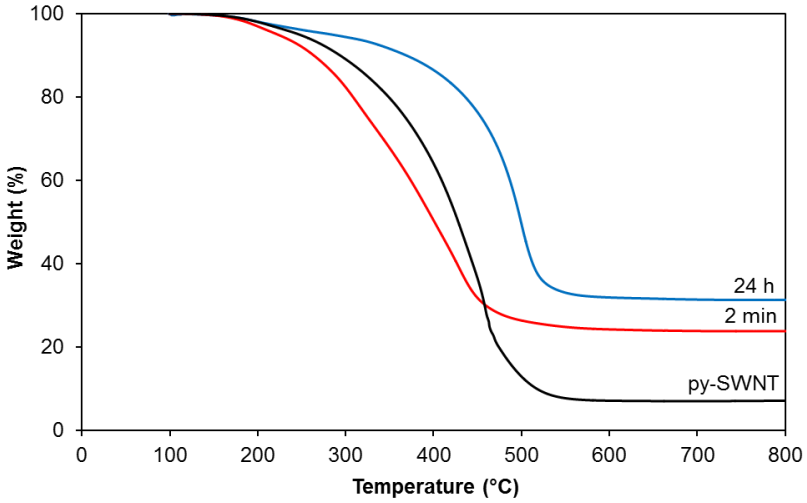

Figure 3.30. TGA in air of py-SWNT and py-SWNTs after electroless deposition of Cu using 1.48 g/L $CuSO_4 \cdot 5H_2O$, 1.12 g/L EDTA, and 3.57 g/L hydrazine in aqueous solution for 2 min and using 84.07 g/L $CuSO_4 \cdot 5H_2O$ and 25.38 mL/L hydrazine in MeOH solution for 24 h of reaction time.

Conclusions

Pyridine functionalized SWNTs and US-SWNTs were synthesized and functionalized with copper seeds. XPS analysis of the samples showed that US-SWNTs contain a higher atomic % of carboxylic acid groups and, correspondingly, the py-US-SWNTs contain a higher concentration of pyridine groups as compared to the piranha etched SWNTs and py-SWNTs. A UV-visible spectroscopy experiment showed that Cu(II) ions are taken up by py-functionalized SWNTs and US-SWNTs, confirming the ions' interaction with the pyridine groups. After optimization of reaction time and

concentration, 3 – 12 nm Cu seeds were deposited uniformly on US-SWNTs. These were confirmed to be Cu(0) by XPS and SAED. A ^{1}H NMR study showed that free copper seeds are capped by pyridine groups, indicating that the seeds are indeed bound to the pyridine groups on py-US-SWNTs and py-SWNTs. A comparison of Cu deposition using the optimized method on py-US-SWNTs and oxidized US-SWNTs indicated that the pyridine groups are critical to the formation of evenly dispersed Cu seed particles with a small size distribution. However, using the same 2 min optimized protocol with py-SWNTs resulted in the observation of dark coatings on the tubes in TEM, suggesting the formation of small Cu clusters on the tubes. This was verified using EDX mapping, which showed a uniform layer of Cu across the py-SWNTs. When py-SWNTs underwent 30 min of Cu deposition time using the optimized protocol, Cu seed structures as well as some larger copper particles emerged. However, when a higher $CuSO_4 \cdot 5H_2O$ concentration was used without EDTA in MeOH for 30 min of deposition time, the py-SWNTs were deposited with a dark coating of Cu similar to the optimized aqueous 2 min reaction. Given the higher Cu(II) concentration, lack of Cu(II)-complexing EDTA and increased reaction time, these results are unexpected. Despite better dispersion of py-SWNTs in MeOH, our results suggest that it slows the Cu deposition rate. Allowing the MeOH solution to proceed for 24 h resulted in large ‘sea urchin’ type structures. These results suggest that the length of the SWNT and/or the degree of pyridine functionality, as well as the choice of solvent, all have an effect on Cu growth rate and morphology. As expected, TGA analysis of the Cu-deposited py-SWNTs and py-US-SWNTs indicated increasing copper with increasing reaction time.

Future work on this project should include further deposition of copper to form complete copper composites. These should be measured for improvements in conductivity compared to the SWNTs themselves as well as compared to other composites.

Experimental

All reagents were purchased from Sigma Aldrich and used as received unless otherwise noted. 4-Hydroxypyridine was dried over sulfuric acid for 2 days in a vacuum desiccator before use. HPLC grade ultra-high purity water from Sigma Aldrich was used for all aqueous reactions. Oxidized US-SWNTs were kindly donated by the Wilson group at Rice University and were placed under vacuum for an hour before use. Pristine HiPco single-walled carbon nanotube, 09-HiPco-0093 batch No. 195.7 (p-SWNT), were obtained from the Carbon Nanotube Laboratory (CNL) at Rice University and used as received. SWNT purification, piranha treatment and all Cu depositions of SWNTs were carried out at Swansea University in Wales.[56] Glassware was placed in a base bath overnight, then washed with soap and water and dried in an oven overnight before use. XPS was measured on a PHI Quantera XPS Scanning Microprobe using a monochromated Al K_α X-ray source. All spectra were recorded using a charge neutralizer to limit differential charging and subsequently calibrated to the carbon peak at a binding energy of 284.5 eV. Survey scans were recorded at a pass energy of 140 eV and high-resolution data at a pass energy of 26 eV. Data was fitted using MultiPak software. TEM measurements were taken on a Jeol 1230 High Contrast TEM with a W filament and an operating voltage of 80 kV or on a Jeol 2100 TEM with a field emission electron gun and an operating voltage of 200 kV. TEM samples were prepared by drop-drying a dilute

solution of carbon nanotubes suspended in ethanol onto a 300-mesh gold grid with a lacey carbon film (Agar-Scientific Ltd). SAED and EDX were acquired using a Jeol 2100 TEM with a field emission electron gun and an operating voltage of 200 kV. UV-visible spectroscopy was acquired using Cary 100 and Agilent 8453 UV-visible spectrophotometers, scanning between 550 and 900 nm with a step size of 0.5 nm. ^{1}H NMR experiments were performed on a Bruker 400 MHz instrument in D_2O at 25 ˚C. TGA was carried out using TA Instruments SDT Q600 thermo gravimetric analyzer (TA Instruments, USA) at Swansea University in Wales.[56] All samples for TGA were purged for 1 h, then ramped at 10 ˚C/min to 100 ˚C, where they remained for 1 h under 100 mL/min flow of argon. For TGA experiments run in argon, the temperature was then ramped at 10 ˚C/min to 1000 ˚C. For TGA experiments run in air, the gas was switched to air with a 100 mL/min flow rate and the samples were held at 100 ˚C for another 5 min. Then, the temperature was ramped at a rate of 10 ˚C/min to 1100 ˚C.

Synthesis of US-SWNT-COCl. This method was adapted from the literature.[28] Oxidized US-SWNTs (30 mg) were added to an oven-dried Schlenk flask equipped with stir bar and a reflux condenser. The apparatus was put under vacuum for an hour, then backfilled with argon. Anhydrous dimethylformamide (DMF, 0.3 mL) and thionyl chloride (7.25 mL) were added to the reaction flask via syringe. The suspension was stirred and heated to 60 ˚C in an oil bath for 2 days. The suspension was allowed to cool to room temperature, then dichloromethane from the solvent purification system was added until the total volume was around 25 mL. The functionalized US-SWNTs were allowed to settle, and the liquid was decanted off using a cannula. This was repeated 3 times. When as much liquid had been removed as possible, the US-SWNTs were dried

under vacuum. The resulting black powder was stored under argon in its reaction flask for future use.

Synthesis of py-US-SWNT. This method was adapted from the literature.[28] Hydroxypyridine (90 mg) was added to the reaction flask containing US-SWNT-COCl (~30 mg) in the glove box. The flask was then put on a Schlenk line under argon and equipped with a reflux condenser. Dichloromethane from the solvent purification system (25 mL) was added to the flask via cannula, and the mixture was stirred and heated to 50 ˚C in an oil bath for 2 days. The suspension was cooled to room temperature, and the product was filtered on a PTFE filter in air. The black powder was rinsed with dichloromethane and ethanol. It was then placed in a vacuum desiccator to dry before TEM, XPS and TGA analysis.

UV-Vis study of divalent copper adsorption by py-US-SWNTs. Py-US-SWNTs (10 mg) were bath sonicated in methanol (4 mL) for 10 minutes. Then, 2 mL of a 0.016 M copper nitrate solution was added, and the suspension was sonicated for another 10 minutes. It was then placed on a rotary shaker for 24 hours. The suspension was then filtered through a syringe filter, and the filtrate was analyzed using UV-Vis spectroscopy between 550 and 900 nm with a step size of 0.5 nm. For comparison, the 0.016 M copper nitrate stock solution was also filtered and analyzed.

Functionalization of py-US-SWNTs and US-SWNTs with copper seeds. This method was adapted from the literature using 1/8 of the original reagent concentrations (see Table 3.4 for variations).[37] Py-US-SWNTs (12.9 mg), $CuSO_4 \cdot 5H_2O$ (62 mg), ethylenediaminetetraacetic acid (EDTA, 47 mg) and ultra-high purity water (HPLC grade, 42 mL) were added to a round bottom flask (100-mL) equipped with a stir bar. The

mixture was bath sonicated to disperse the py-US-SWNTs, then promptly placed on a stir plate to keep the py-US-SWNTs from settling. Hydrazine (78%, 0.15 mL) was added to the solution dropwise. At the end of the hydrazine addition, a timer was started. Aliquots of solution were removed, filtered and rinsed with water at 2, 5, 10 and 15 minutes of reaction time. At 30 minutes, all of the remaining mixture was filtered and rinsed with water. All samples were placed in a vacuum desiccator to dry before they were analyzed by XPS and TEM.

Preparation of pyridine-capped seeds for ^{1}H NMR. $CuSO_4 \cdot 5H_2O$ (90 mg) and EDTA (70 mg) were dissolved in ultra-high purity water (42 mL). The solution was stirred and hydrazine (0.22 mL) was added dropwise. The solution was allowed to stir until the bubbling stopped. The product was filtered and rinsed with ultra-high purity water. The resulting orange cake was allowed to dry. The particles were then placed in a D_2O solution of pyridine (3.5 mL and 0.35 mL, respectively) and mixed. The particles dissolved, producing an orange-brown solution. This was filtered through a syringe filter into an NMR tube. The sample was analyzed by ^{1}H NMR and TEM.

References

1. J. Baur and E. Silverman, *MRS Bull.*, 4AD, **32**, 328–334.

2 P. L. McEuen, M. S. Fuhrer and Hongkun Park, *IEEE Trans. Nanotechnol.*, 2002, **1**, 78–85.

3. P. Jarosz, C. Schauerman, J. Alvarenga, B. Moses, T. Mastrangelo, R. Raffaelle, R. Ridgley and B. Landi, *Nanoscale*, 2011, **3**, 4542–4553.

4. M. Stemmle, F. Merschel, M. Noe and A. Hobl, IEEE, 2013, pp. 323–326.

5. O. Hjortstam, P. Isberg, S. Soderholm and H. Dai, *Appl. Phys. A*, 2004, **78**, 1175–1179.

6. D. F. Lee, M. Burwell and H. Stillman, *Priority Research Areas to Accelerate the Development of Practical Ultra-conductive Copper Conductors*, Oak Ridge National Laboratory, 2015.

7. C. Subramaniam, T. Yamada, K. Kobashi, A. Sekiguchi, D. N. Futaba, M. Yumura and K. Hata, *Nat. Commun.*, 2013, **4**, 2202.

8. N. Behabtu, C. C. Young, D. E. Tsentalovich, O. Kleinerman, X. Wang, A. W. K. Ma, E. A. Bengio, R. F. ter Waarbeek, J. J. de Jong, R. E. Hoogerwerf, S. B. Fairchild, J. B. Ferguson, B. Maruyama, J. Kono, Y. Talmon, Y. Cohen, M. J. Otto and M. Pasquali, *Science*, 2013, **339**, 182–186.

9. X. Wang, N. Behabtu, C. C. Young, D. E. Tsentalovich, M. Pasquali and J. Kono, *Adv. Funct. Mater.*, 2014, **24**, 3241–3249.

10. B. Q. Wei, R. Vajtai and P. M. Ajayan, *Appl. Phys. Lett.*, 2001, **79**, 1172–1174.

11. Z. Yao, C. L. Kane and C. Dekker, *Phys. Rev. Lett.*, 2000, **84**, 2941–2944.

12. Q. Chen, US Patent 7651766 B2, 2010.

13. G. Chai, Y. Sun, J. 'Jenny' Sun and Q. Chen, *J. Micromech. Microeng.*, 2008, **18**, 035013.

14. S. R. Dong, J. P. Tu and X. B. Zhang, *Mater. Sci. Eng. A*, 2001, **313**, 83–87.

15. S. M. Uddin, T. Mahmud, C. Wolf, C. Glanz, I. Kolaric, C. Volkmer, H. Höller, U. Wienecke, S. Roth and H.-J. Fecht, *Compos. Sci. Technol.*, 2010, **70**, 2253–2257.

16. A. S. Muhsan, F. Ahmad, N. M. Mohamed, P. S. M. Megat Yusoff and M. R. Raza, *Nanosci. Nanotechnol. Lett.*, 2014, **6**, 865–874.

17. C. Xu, G. Wu, Z. Liu, D. Wu, T. T. Meek and Q. Han, *Mater. Res. Bull.*, 2004, **39**, 1499–1505.

18. W. M. Daoush, B. K. Lim, C. B. Mo, D. H. Nam and S. H. Hong, *Mater. Sci. Eng. A*, 2009, **513**–**514**, 247–253.

19. T. W. Ebbesen, H. J. Lezec, H. Hiura, J. W. Bennett, H. F. Ghaemi and T. Thio, *Nature*, 1996, **382**, 54–56.

20. Y. L. Yang, Y. D. Wang, Y. Ren, C. S. He, J. N. Deng, J. Nan, J. G. Chen and L. Zuo, *Mater. Lett.*, 2008, **62**, 47–50.

21. J. J. Yoo, J. Y. Song, J. Yu, H. K. Lyeo, S. Lee and J. H. Hahn, IEEE, 2008, pp. 1282–1286.

22. Y. Chai, P. C. H. Chan, Y. Fu, Y. C. Chuang and C. Y. Liu, IEEE, 2008, pp. 412–420.

23. G. Xu, J. Zhao, S. Li, X. Zhang, Z. Yong and Q. Li, *Nanoscale*, 2011, **3**, 4215–4219.

24. K. T. Kim, S. I. Cha, T. Gemming, J. Eckert and S. H. Hong, *Small*, 2008, **4**, 1936–1940.

25. H. R. Jafry, E. Whitsitt and A. R. Barron, *J. Mater. Sci.*, 2007, **42**, 7381–7388.

26. D. Ogrin, J. Chattopadhyay, A. K. Sadana, W. E. Billups and A. R. Barron, *J. Am. Chem. Soc.*, 2006, **128**, 11322–11323.

27. D. Ogrin, R. E. Anderson, Colorado Ramon, B. Maruyama, M. J. Pender, V. C. Moore, S. T. Pheasant, L. McJilton, H. K. Schmidt, R. H. Hauge, W. E. Billups, J.

M. Tour, R. E. Smalley and A. R. Barron, *J. Phys. Chem. C*, 2007, **111**, 17804–17806.

28. C. E. Hamilton, D. Ogrin, L. McJilton, V. C. Moore, R. Anderson, R. E. Smalley and A. R. Barron, *Dalton T.*, 2008, 2937.

29. C. E. Gowenlock, V. Gomez, J. D. McGettrick, E. Andreoli and A. R. Barron, *J. Coat. Technol. Res.*, 2017, **14**, 195–205.

30. C. E. Gowenlock, J. D. McGettrick, P. D. McNaughter, P. O'Brien, C. W. Dunnill and A. R. Barron, *Main Group Chem.*, 2016, **15**, 1–15.

31. A. M. Lyons, M. J. Vasile, E. M. Pearce and J. V. Waszczak, *Macromolecules*, 1988, **21**, 3125–3134.

32. P. B. Bowman and L. B. Rogers, *Journal of Inorganic and Nuclear Chemistry*, 1966, **28**, 2215–2224.

33. J. F. Weiss, G. Tollin and J. T. Yoke, *Inorg. Chem.*, 1964, **3**, 1344–1348.

34. J. R. Clifton and J. T. Yoke, *Inorg. Chem.*, 1968, **7**, 39–46.

35. K. M. Lincoln, M. E. Offutt, T. D. Hayden, R. E. Saunders and K. N. Green, *Inorg. Chem.*, 2014, **53**, 1406–1416.

36. S. P. Rawat and M. Choudhary, *Int. J. Inorg. Chem.*, 2014, **2014**, 1–8.

37. G. Mondin, F. M. Wisser, A. Leifert, N. Mohamed-Noriega, J. Grothe, S. Dörfler and S. Kaskel, *J. Colloid Interface Sci.*, 2013, **411**, 187–193.

38. J. M. Ashcroft, K. B. Hartman, Y. Mackeyev, C. Hofmann, S. Pheasant, L. B. Alemany and L. J. Wilson, *Nanotechnol.*, 2006, **17**, 5033.

39. Z. Gu, H. Peng, R. H. Hauge, R. E. Smalley and J. L. Margrave, *Nano Lett.*, 2002, **2**, 1009–1013.

40. A. Jung, R. Graupner, L. Ley and A. Hirsch, *phys. stat. sol. (b)*, 2006, **243**, 3217–3220.

41. A. Gizzatov, M. Hernández-Rivera, V. Keshishian, Y. Mackeyev, J. J. Law, A. Guven, R. Sethi, F. Qu, R. Muthupillai, M. da G. Cabreira-Hansen, J. T. Willerson, E. C. Perin, Q. Ma, R. G. Bryant and L. J. Wilson, *Nanoscale*, 2015, **7**, 12085–12091.

42. J. Zhang, H. Zou, Q. Qing, Y. Yang, Q. Li, Z. Liu, X. Guo and Z. Du, *J. Phys. Chem. B*, 2003, **107**, 3712–3718.

43. I. W. Chiang, B. E. Brinson, A. Y. Huang, P. A. Willis, M. J. Bronikowski, J. L. Margrave, R. E. Smalley and R. H. Hauge, *J. Phys. Chem. B*, 2001, **105**, 8297–8301.

44. V. Gomez, S. Irusta, O. B. Lawal, W. Adams, R. H. Hauge, C. W. Dunnill and A. R. Barron, *RSC Adv.*, 2016, **6**, 11895–11902.

45. H. R. Darabi, M. Jafar Tehrani, K. Aghapoor, F. Mohsenzadeh and R. Malekfar, *Appl. Surf. Sci.*, 2012, **258**, 8953–8958.

46. V. Datsyuk, M. Kalyva, K. Papagelis, J. Parthenios, D. Tasis, A. Siokou, I. Kallitsis and C. Galiotis, *Carbon*, 2008, **46**, 833–840.

47. P. N. Alagappan, J. Heimann, L. Morrow, E. Andreoli and A. R. Barron, 2017.

48. C. A. Tolman, *Chem. Rev.*, 1977, **77**, 313–348.

49. T. L. Brown and K. J. Lee, *Coord. Chem. Rev.*, 1993, **128**, 89–116.

50. P. W. Voorhees, *J. Stat. Phys.*, 1985, **38**, 231–252.

51. B. D. Cullity and S. R. Stock, *Elements of X-ray diffraction*, Pearson/Prentice Hall, Upper Saddle River, NJ, 3rd ed., 2001.

52. J. B. Forsyth and S. Hull, *Journal of Physics: Condensed Matter*, 1991, **3**, 5257.

53. L. Machala, J. Tuček and R. Zbořil, *Chem. Mater.*, 2011, **23**, 3255–3272.

54. T. H. Fleisch and G. J. Mains, *Appl. Surf. Sci.*, 1982, **10**, 51–62.

55. J. C. Zhou, D. F. Wu, W. Jiang and Y. D. Li, *Chem. Eng. Technol.*, 2009, **32**, 1520–1526.

56. K. D. Wright, C. E. Gowenlock and A. R. Barron, submitted for publication.

Chapter 4

XPS of Microwave-Treated Hot Mill Sludge from the Steel Industry

Portions of this chapter are included in a manuscript by V. Gomez, K.D. Wright, G.L. Esquenazi and A.R. Barron submitted for publication.

Introduction

The hot rolling mill (HRM) process in steel production results in an oily HRM sludge containing a high percentage of iron oxides, alloying elements, along with oils and other organic residues. The recycling and recovery processes of the sludge are particularly challenging due to the presence of hydrocarbons with a low flash point in its composition.[1] High amounts of sludges are generated by the steel industry with one estimate suggesting that 0.9 ton of oily sludge is produced for every 1000 tons of rolling steel.[2] Mill sludge cannot be recycled via sintering because of its high oil level (5 - 20%) and is normally treated as a landfill waste.[3,4] This waste product is creating an adverse impact on the environment due to the content of hazardous organic compounds, especially if it is landfilled. The reuse of the iron content also is of economic necessity in reducing manufacturing costs within the steel industry in the West, which is currently struggling to compete worldwide with cheap imports, cope with increasing energy bills, and with the increased legislated standards.[5] The cost of manufacturing is a major contributor to the contraction in the US and European steel industry. By transforming or reusing hot rolling mill wastes, metals and mineral resources can be recovered and the environmental impact reduced.

A small fraction of HRM sludge is re-used, however, the presence of flammable hydrocarbons limits its use since it causes fires within the electrostatic precipitators in the plant. Mill sludges with high oil content could be recycled via sintering, however, due to the high volatile organic compounds and dioxin emissions in exhaust fume systems, they are normally treated as landfill waste.[4] Several approaches have been studied for the recovery of the metals and the removal of oils from the iron sludges. Conventional methods for recycling HRM sludge include physiochemical and heating treatments. Heating methods are very expensive since they require a secondary fuel, and they have a low oil removal efficiency.[1] Some researchers have proposed using a reduction followed by a magnetic separation step to recover the iron in the samples.[6–8] Vacuum distillation followed by either an oxidizing roasting or a hydrogen reduction step have also been employed to obtain high purity ferric oxide powders.[9]

Microwaves have been used as a first processing step in the recovery of different sludge and industrial wastes.[10–15] The rheological behaviour of different metallic slurries has been modified by using microwave (MW) energy.[15] In addition, microwave pyrolysis has been used as a disposal method for waste oil by using a bed of highly microwave-absorbent material.[16] Pyrolysis of waste engine oil using a metallic pyrolysis char as a microwave-absorbent material has been reported.[14] Rapid heating, decreased sintering temperatures and improved physical and mechanical properties have prompted us to investigate microwave energy for the synthesis and processing of a range of materials,[17–19] as well as the use of nanoparticles as nano susceptors for rapid processing.[20–22] Of particular interest with regard to the present study was the role of residual catalyst particles during the microwave purification of carbon nanotubes.[22] The potential of these

iron oxide/iron nanoparticles to promote microwave heating suggested that similar effects could occur for HRM sludge.

In this study, microwaves were used to remove the water and reduce the amount of oils in industrial steel hot mill sludge.[23] The metals present in the sludge act as a highly microwave-absorbent material catalysing the combustion of the oils under air. Because the goal is to recycle the metals in order to reduce the environmental and economic cost of landfilling it, it is important to identify the end state of these metals. To this end, XPS was used to characterize microwaved and heated sludge samples.

Results and Discussion

Hot mill sludge is a steel industry waste product formed by a concentrated mixture of solid and water (Figure 4.1). It generally contains metallic iron, iron oxides, traces of non-ferrous metals, alkaline compounds and oils from the rolling process.[24] Generally, the chemical composition of the mill scale varies according to the type of steel produced and the process used. Maghemite (Fe_2O_3) and pure iron (Fe) were identified to be the most abundant iron phases from a cold rolling mill sludge,[25] while others have reported a rolling mill scale comprised mainly of metallic iron and a mixture of the iron oxides wüstite (FeO), hematite (α-Fe_2O_3) and magnetite ($FeO.Fe_2O_3$).[24] X-ray diffraction of our material showed a composition which is closer to the latter.[23] This is confirmed by the high resolution Fe $2p_{3/2}$ XPS (Figure 4.2) of the as received sludge, which shows the presence of Fe(0), Fe(II) and Fe(III). It should be noted that these samples have a very high concentration of oils; XPS shows that the sludge is 85.14% carbon, 8.20% oxygen and 6.67% iron.

Figure 4.1. A photograph of the as received HRM sludge sourced from Tata Steel Strip Products UK Port Talbot Works (Wales).

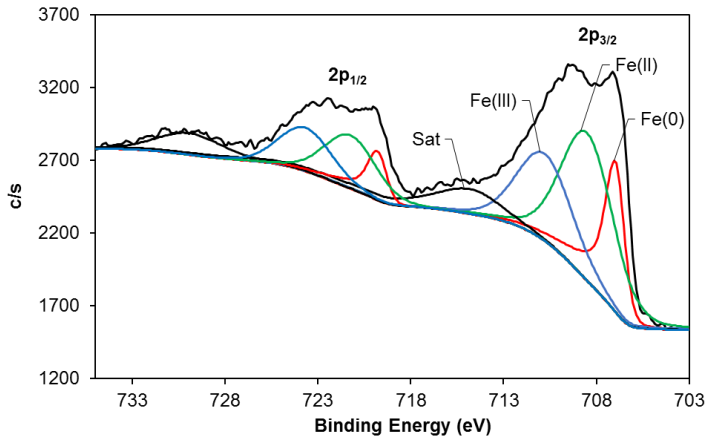

Figure 4.2. The high resolution Fe 2p XPS peak of the as received HRM sludge.

Treatment of HRM sludge. Sludge samples were heated by microwave irradiation with different times (SL-MW_n, where n is the number of 1 min heat cycles) and by a thermal treatment at 200 °C and 500 °C (Table 4.1). The position of two weight-loss steps seen in TGA of the as received HRM sludge[23] defined the choice of 200 °C and 500 °C for the thermal treatment (SL-200 and SL-500, respectively) as comparison with the microwave treatments.

Table 4.1. Summary of sample abbreviations.

Sample name	Description
SL	As received sludge
SL-MW_n	*n* x 1 min of microwave irradiation
SL-200	200 °C for 4 h in air
SL-500	500 °C for 4 h in air

The samples were studied by XPS in order to assess the oil to iron ratio and the iron oxidation state after the heating and microwaving processes. XPS analysis shows spectral bands attributed to Fe 2p, O 1s and C 1s. With the exception of SL-500, the samples are primarily made of carbon (Table 4.2), indicating a high oil concentration even after microwaving or heating to 200 °C. SL-500, on the other hand, shows a notable reduction in the carbon concentration from >90% to only 22.5%, suggesting a reduction in the amount of oils present in the sludge sample after they are treated at 500 °C. Because XPS does not give atomic concentrations that are necessarily representative of the bulk, it is unsurprising that the Fe to C ratios observed by XPS do not completely

Table 4.2. The Fe and C atomic concentrations of the as-received and treated sludge samples measured by XPS after 1 min of sputtering with a 3 kV Ar ion beam.

Sample	Fe (%)	C (%)
SL	7.26	92.74
SL-MW_1	3.35	96.65
SL-MW_5	0.75	99.25
SL-200	1.12	98.88
SL-500	77.47	22.53

agree with the TGA and FTIR data for SL-MW_n or SL-200.[23] According to these data, all treated samples show a decrease in oil content with SL-MW_5 and SL-500 leading to the greatest decrease.[23]

The high resolution Fe 2p XPS signals of the treated samples are shown in Figure 4.3, and the relative atomic concentrations of the different iron oxidations states obtained from these signals is shown in Table 4.3. After heating the sludge to 500 °C, the sample contains no metallic iron and is found to be primarily composed of Fe(III). Figure 4.3 shows a dramatic reduction of the intensity of the Fe(II) peak while increasing the Fe(III) peak after heating the sludge at 200 and 500 °C. After microwaving the samples, there is also a decrease in the observed abundance of Fe(0) and an increase in the oxidized iron compared to the untreated sludge. However, a comparison of SL-MW_1 and SL-MW_5 shows an increase in Fe(0) as well as an increase in Fe(III) with longer microwave irradiation. These results show a general increase in iron oxidation state with heating, which is expected since the samples were heated in air. Thus, we expect that the relatively low Fe(0) concentration observed for SL-MW_1 is not representative of the sample as a whole. Comparing the microwaved and thermal treated samples, it is clear that microwave irradiation leads to less extensive oxidation than heating the sample, which is an advantage in case a reduction step is added to recover the iron in the samples. Although the concentrations do not match, the general increase in oxidation state with heating observed in XPS is in agreement with the X-ray diffraction (XRD) data shown in Table 4.4. We suspect that the reason for the disagreement in atomic concentrations is due to iron reduction by argon beam sputtering in XPS and the fact that XPS is a surface analysis technique.[23,26,27]

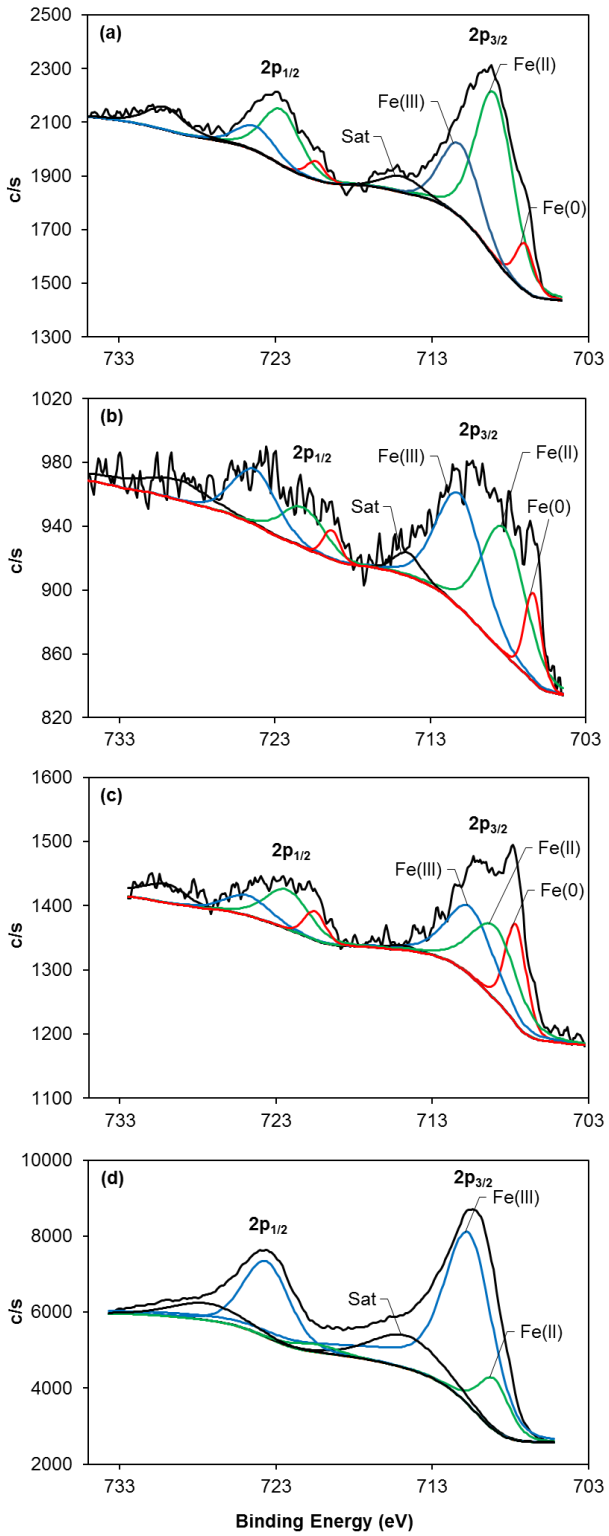

Figure 4.3. The high resolution Fe 2p XPS signals of (a) SL-MW_1, (b) SL-MW_5, (c) SL-200 and (d) SL-500. "Sat" indicates the Fe oxide satellite peaks.[27]

Table 4.3. The atomic concentrations of various iron oxidation states in as-received and treated sludge samples obtained from the high resolution Fe 2p XPS deconvolution.

Sample	Fe(0) (Atomic %)	Fe(II) (Atomic %)	Fe(III) (Atomic %)
SL	22.7	47.8	29.5
SL-MW_1	9.5	63.6	26.9
SL-MW_5	11.7	45.2	43.1
SL-200	23.1	38.8	38.0
SL-500	0.0	14.4	85.6

Table 4.4. XRD Rietveld quantitative % phase analysis of HRM sludge samples after microwave and thermal treatment.[23]

Sample	Iron Fe(0)	Wüstite FeO	Magnetite $FeO.Fe_2O_3$	Hematite α-Fe_2O_3	Goethite
SL	1	48	39	11	1
SL-MW_5	3	41	44	14	-
SL-500	3	2	37	58	-

Conclusions

Hot mill sludge is an iron oxide steel industry by-product with a high content of oils, resulting in a sticky solid that is difficult to manipulate and to recycle. In this study, sludge samples have been treated by microwave irradiation and thermolysis in order to reduce their content of oils while minimizing iron oxidation so that the iron may be recycled later.

Although microwave irradiation did not significantly reduce the oil content according to XPS, other methods of analysis have shown otherwise.[23] But, heating the samples to 500 °C for 4 h resulted in the most drastic decrease in oil content according to FT-IR, TGA and XPS.[23] Despite this, the microwave treatments are still a faster and more efficient way for "drying" sludge than conventional heating, since they only require minutes rather than hours to reduce the oil content. In addition, microwaving the samples leads to less oxidation of the samples than heating them, which is an advantage in case a reduction step is added to recover the iron.

Experimental

Hot rolling mill (HRM) sludge was provided by Tata Steel Strip Products UK Port Talbot Works (Wales, UK). X-ray photoelectron spectroscopy (XPS) measurements were obtained using a PHI Quantera system with an aluminium X-ray source at 1486.7 eV. Data was analysed with PHI MultiPak program. A spectrum energy calibration was performed with respect to the C1s peak with binding energy set to 284.8 eV. All thermal and microwave treatments, XRD, TGA and FT-IR were performed at Swansea University in Wales.[23]

References

1. J.-W. Park, J.-C. Ahn, H. Song, K. Park, H. Shin and J. Ahn, *Resour. Conserv. Recy.*, 2002, **34**, 129–140.
2. L. Qin, J. Han, X. He, Y. Zhan and F. Yu, *J. Environ. Manage.*, 2015, **154**, 177–182.
3. L. Camci, S. Aydin and C. Arslan, *Turkish J. Eng. Env. Sci.*, 2001, **26**, 37–44.

4. M. I. Martin, F. A. Lopez, M. E. Rabanal and J. M. Torralba, in *1st Spanish National Conference on Advances in Materials Recycling and Eco-Energy Madrid*, 2009, pp. 4–5.

5. *Report to the Department of Energy and Climate Change, The Scottish Government, The Welsh Government and The Northern Ireland Department of the Environment*, 2015.

6. C. L. Wang, H. F. Yang, B. P. Jiang, J. L. Zhang, L. F. Lu and Q. Y. Tang, *Adv. Mater.*, 2014, **878**, 254–263.

7. L. M. Yu, *AMM*, 2014, **692**, 332–336.

8. N. Alavifard, H. Shalchian, A. Rafsanjani-Abbasi, J. Vahdati Khaki and A. Babakhani, *IJMSE*, 2016, **13**, 60–71.

9. B. Liu, S. Zhang, J. Tian, D. Pan, Y. Liu and A. A. Volinsky, *Int. J. Min. Met. Mater.*, 2013, **20**, 941–946.

10. S. W. Kingman, K. Jackson, S. M. Bradshaw, N. A. Rowson and R. Greenwood, *Powder Technol.*, 2004, **146**, 176–184.

11. P. Kumar, B. K. Sahoo, S. De, D. D. Kar, S. Chakraborty and B. C. Meikap, *J. Ind. Eng. Chem.*, 2010, **16**, 805–812.

12. Y. Saito, K. Kawahira, N. Yoshikawa, H. Todoroki and S. Taniguchi, *ISIJ Int.*, 2011, **51**, 878–883.

13. E. R. Bobicki, Q. Liu and Z. Xu, *Miner. Eng.*, 2014, **61**, 97–104.

14. S. S. Lam, R. K. Liew, C. K. Cheng and H. A. Chase, *Appl. Catal. B*, 2015, **176**–**177**, 601–617.

15. B. K. Sahoo, S. De and B. C. Meikap, *J. Ind. Eng. Chem.*, 2015, **25**, 122–130.

16. S. S. Lam, A. D. Russell and H. A. Chase, *Ind. Eng. Chem. Res.*, 2010, **49**, 10845–10851.

17. V. Gomez, A. M. Balu, J. C. Serrano-Ruiz, S. Irusta, D. D. Dionysiou, R. Luque and J. Santamaría, *Appl. Catal. A*, 2012, **441**–**442**, 47–53.

18. V. Gomez, A. Clemente, S. Irusta, F. Balas and J. Santamaria, *Environ. Sci.: Nano*, 2014, **1**, 496–503.

19. C. C. Landry, J. Lockwood and A. R. Barron, *Chem. Mater.*, 1995, **7**, 699–706.

20. V. Gomez, C. W. Dunnill and A. R. Barron, *Carbon*, 2015, **93**, 774–781.

21. V. Gomez, S. Alexander and A. R. Barron, *Colloids Surf. A*, 2017, **513**, 297–305.

22. V. Gomez, S. Irusta, O. B. Lawal, W. Adams, R. H. Hauge, C. W. Dunnill and A. R. Barron, *RSC Adv.*, 2016, **6**, 11895–11902.

23. V. Gomez, K. D. Wright, G. L. Esquenazi and A. R. Barron, 2017, submitted for publication.

24. M. I. Martín, F. A. López and J. M. Torralba, *Ironmak. Steelmak.*, 2012, **39**, 155–162.

25. B. Liu, S.-G. Zang, J. Tian, D. Pan and H.-X. Zhu, *Rare Metals*, 2013, **32**, 518–523.

26. E. Paparazzo, *Appl. Surf. Sci.*, 1986, **25**, 1–12.

27. P Mills and J L Sullivan, *J. Phys. D: Appl. Phys.*, 1983, **16**, 723.

Conclusions

Compared to organic functionalization, methods for functionalizing CNTs with metals is lacking. Although metal particles have been attached to CNTs in a variety of different ways, there is a need for the development of novel approaches in many cases. For instance, copper has only been attached to CNTs by way of van der Waals interactions or through bonding to carboxylic acid functional groups. Likewise, the attachment of metal atoms to CNTs is severely under-studied, with only two groups reporting CNT-metal complexes. Thus, in an effort to expand the field of CNT functionalization, SWNTs and other conjugated carbon materials were deposited with copper and Group 6 metals.

In attempting to functionalize SWNTs with Group 6 metal atoms, we found that the formation of such species is very sensitive to oxidation by adsorbed/bound oxygen and by oxidized residual catalyst material. By annealing and acid treating the SWNTs, we were able to decrease the amount oxygen species and residual catalyst material, allowing for the addition of some zero-valent chromium. By using very high purity SWNTs (with negligible metal catalyst material), we were able to deposit primarily zero-valent tungsten, which is less prone to oxidation than chromium. Similar experiments with high purity graphene showed deposition of chromium metal as well as the formation of $Cr(graphene)_2$ sandwich complexes. This work illustrates the importance of the residual catalyst material on SWNT chemistry- a subject that has not been discussed except in terms of biological toxicity.

We also attempted to functionalize C_{60} fullerene with Group 6 metals, which would allow for the characterization of this complex using NMR. However, the literature

reports contradicting results regarding the stability of such a complex. After attempting the synthesis using a variety of different experiments, we concluded that C_{60}-Cr complexes are not stable enough (at ambient temperature) to be isolated or characterized.

As a result of our previous studies showing oxidation issues with SWNTs and because of the limited characterization methods available for SWNTs, we also used C_{60} fullerene to study dihapto complexes of conjugated carbon systems with copper(I). However, the synthesis of these complexes proved to be challenging due to C_{60}'s insolubility and decomposition of the products. Nonetheless, the NMR experiments suggested the formation of three different products from the reaction of C_{60} with $[Cu(CH_3CN)_4]BF_4$ and mesitylene-2,2'-dipyridylamine (mes-dpa). Two of the products were assigned as $[(CH_3CN)_2Cu(mes\text{-}dpa)]BF_4$ and $[Cu(mes\text{-}dpa)_2]BF_4$. Analyzing the possible outcomes from this reaction then lead to the assignment of the desired $[(C_{60})Cu(mes\text{-}dpa)]BF_4$ for the final set of ^1H NMR signals by process of elimination. To eliminate the formation of the first two species, C_{60} was reacted with $[(C_2H_4)Cu(mes\text{-}dpa)]ClO_4$. Analysis of the single set of ^1H NMR signals suggested the formation of $[(C_{60})Cu(mes\text{-}dpa)]ClO_4$. Unfortunately, this complex decomposed before ^{13}C NMR could be acquired to confirm the assignment. But, assuming that the ^1H NMR assignment is correct, the formation of a C_{60}-Cu(I) complex also suggests that similar complexes may be formed with CNTs. However, based on our work with Group 6 metal functionalization, it is obvious that the CNTs would need to be highly pure and oxygen free.

Copper(0) was deposited on pyridine functionalized SWNTs. After optimizing the concentrations of the starting materials and the reaction times, we were able to add well

dispersed zero-valent copper seeds to US-SWNTs. The size of the particles could be increased by increasing the reaction time and/or increasing the concentration of the copper starting material and the reducing agent. However, increasing concentrations and reaction times led to a wider size distribution of the resulting copper particles. Use of the same optimized method to deposit copper on full length pyridine functionalized SWNTs resulted in the coating of the tubes with an even copper layer seen as a dark coating in TEM rather than as copper seeds. These results suggested that the length of the SWNTs and/or degree of pyridine functionality has an effect on the copper deposition rate. The attachment of the seeds to the pyridine group was verified using a ^{1}H NMR experiment, which showed characteristic broadening and shifting of pyridine's signals due to metal binding. The adsorption of the Cu(II) precursor by pyridine functionalized SWNTs was observed in a UV-visible spectroscopy experiment, confirming pyridine's ability to act as a seeding location for copper particles. Further, comparing seed growth on pyridine functionalized SWNTs to that on oxidized SWNTs showed that the pyridine groups were necessary for the formation of evenly dispersed copper seeds with a narrow size distribution. These seed functionalized SWNTs have the potential to generate more consistent Cu-CNT composites with high ampacity and conductivity.

Future work on these projects should begin with SWNT purification, since the direct functionalization of SWNTs with Group 6 metals and copper(I) atoms is hindered by residual catalyst material and bound/adsorbed oxygen species. We also recognize that work on the SWNT-Cu composite project could be improved by completing the copper coating and testing the conductivity and ampacity of the resulting Cu-CNT composites.

Appendix: List of Publications and Presentations

1. Kourtney D. Wright and Andrew R. Barron, “Catalyst Residue and Oxygen Species Inhibition of the Formation of Hexahapto-Metal Complexes of Group 6 Metals on Single-Walled Carbon Nanotubes: An XPS Study,” submitted for publication.
2. Kourtney D. Wright, Cathren E. Gowenlock and Andrew R. Barron, “Seeded Growth of Copper on Carbon Nanotubes,” manuscript in preparation.
3. Virginia Gomez, Kourtney D. Wright, Gibran L. Esquenazi and Andrew R. Barron, “Microwave treatment of a hot mill sludge from the steel industry: *en route* to recycling an industrial waste,” submitted for publication.
4. Covadonga Correas, Kourtney D. Wright, Enrico Andreoli and Andrew R. Barron, “Hydration induced morphological change on proppant surfaces employing a calcium-silicate cement system,” manuscript in preparation.
5. “Group 6 Transition Metal Functionalization of Single Wall Carbon Nanotubes” American Chemical Society Southwest/Southeast Regional Meeting presentation, Memphis, TN 2015.